Title	Effects of Ferric Ions on Carrier-microencapsulation for Suppressing Pyrite Oxidation
Author(s)	Li, Xinlong
Citation	北海道大学. 博士(工学) 甲第13803号
Issue Date	2019-09-25
DOI	10.14943/doctoral.k13803
Doc URL	http://hdl.handle.net/2115/79292
Type	theses (doctoral)
File Information	Li_Xinlong.pdf

Effects of Ferric Ions on Carrier-microencapsulation for Suppressing Pyrite Oxidation

A dissertation submitted in partial fulfillment of the requirements
for the degree of Doctorate in Engineering

By

XINLONG LI

Division of Sustainable Resources Engineering,
Graduate School of Engineering,
Hokkaido University, Japan
2019

Abstract

Pyrite is a common sulfide mineral in nature, and it is separated from valuable minerals and disposed to tailing dams in coal and metal mines. When pyrite is exposed to air and water, it is oxidized to form sulfuric acid, which causes acid mine drainage (AMD), a serious environmental problem in mining industry. Neutralization techniques have been commonly used to treat AMD, but they are unsustainable because AMD formation could be continued even after closure of mine. It is important to develop a sustainable method to suppress pyrite oxidation in tailing dam and prevent AMD formation. Carrier-microencapsulation (CME) has been proposed as a promising method to prevent the formation of AMD by forming a protective coating on pyrite surface. Using model experiments, the previous studies demonstrated that CME using titanium-, silicon- or aluminum-catecholate complexes effectively suppressed pyrite oxidation by forming metal-oxyhydroxide coating on pyrite surface. Considering the actual operation of CME, it is needed to understand the effects of co-existing metal ions. A common co-existing metal ion associated with pyrite is ferric ion, because it is a product of pyrite oxidation process. In this study, the effects of coexisting ferric ions on CME for suppressing pyrite oxidation were investigated.

Chapter 1 included the statement of the problem, objectives of this study and a literature review of pyrite, pyrite oxidation and prevention techniques of AMD formation.

In chapter 2, the thermodynamic and redox properties of ferric-catecholate complex were compared to aluminum- and titanium-catecholate complexes. Mono-, bis- and tris-catecholate complexes were formed in the solution containing ferric ions and catechol as same as aluminum-catechol system, while only tris-catecholate complexes was formed in solution containing titanium ions and catechol. The results of linear sweep voltammetry (LSV) indicated that ferric-catecholate complexes was decomposed sequentially: tris-catecholate complex were decomposed to bis-catecholate complex, and bis-catecholate complex was decomposed to mono-catecholate complex, then finally mono-catecholate complex was decomposed to release ferric ions. The sequential decomposition also occurred for aluminum-catecholate complexes while decomposition of titanium-catecholate complex was a one-step reaction: tris-catecholate complex was directly decomposed to release titanium ions. Among three complexes, ferric-catecholate was decomposed at the lowest redox potential and the decomposition rate was fastest. The coating formed with ferric-catecholate by polarization strongly suppressed the reduction of dissolved oxygen on platinum electrode.

In chapter 3, the effects of ferric-catecholate complexes on pyrite oxidation were investigated. Microscopic observation confirmed that coating was formed on pyrite treated with mono- and bis-catecholate complexes. Results of SEM-EDX and ATR-FTIR indicated that the coating was mainly composed of iron-oxyhydroxide phases. The results of leaching experiments showed that pyrite oxidation was suppressed by ferric-catecholate complexes via two mechanisms: (1) electron donating effects of the complexes, and (2) formation of a protective coating on pyrite.

In chapter 4, the details of coating formation with ferric-catecholate complexes and the effects of the coating on pyrite oxidation were investigated by conducting a series of electrochemical studies. The results of theoretical calculation showed that the sequential decomposition of ferric-catecholate complexes on pyrite occurred at different electrode potentials corresponded to the different HOMO energy levels of the tris-, bis-, and mono-catecholate complexes of ferric ions. Chronoamperometry and EIS using a rotating disk platinum (Pt) electrode indicated that a passive coating was formed when oxidative decomposition of Fe^{3+}-catecholate complexes occurred. When longer decomposition time and higher anodic potentials were applied, defects in the coat decreased, resulting in the formation of a more resistant coating. A comparison of the chronoamperometry results of coated and uncoated pyrite electrodes suggests that the coating formed with ferric-catecholate complex suppressed both anodic and cathodic half-cell reactions of pyrite oxidation by limiting the diffusion of reactants and products between pyrite and bulk solution phase.

In chapter 5, electrochemical properties of ferric-complexes with catechol derivatives, which are catechol substituted with electron donating groups (EDGs) and electron withdrawing group (EWGs) as potential carrier for CME was evaluated. Results of LSV indicated that the oxidation potential of ferric-complexes decreased with EDGs but increased with EWGs. Chronoamperometry and EIS showed the coating formation was enhanced with presence of EDGs while suppressed with

EWGs. Results of leaching experiments suggested that ferric-complexes with EDGs suppressed pyrite oxidation by forming protective coating on pyrite surface while no suppressive effect was achieved by the complexes with EWGs.

Chapter 6 evaluated the effects of ferric-catecholate complexes on Ti-based CME. UV-Vis spectra indicated that both ferric- and titanium-catecholate complexes were formed in solution. The results of LSV and chronoamperometry suggested that ferric- and titanium-catecholate may be oxidatively decomposed at similar potential to form a Fe-Ti-oxyhydroxide due to the co-precipitation of titanium and ferric ion. Shaking flask experiments showed that with presence of ferric-catecholate complexes, decomposition of titanium-catecholate complex to release titanium ions was enhanced. The results of XPS and thermodynamic calculation suggested that $FeTiO_3$ may be formed on pyrite surface.

Chapter 7 summarized the most essential findings of this dissertation.

TABLE OF CONTENTS

Chapter 1 General introduction

1.1 Statement of the problem and objectives of this study

Pyrite (FeS_2) is the most abundant metal sulfide mineral in nature (Bonnissel-Gissinger et al., 1998; Chandra and Gerson, 2010), and is often associated with mineralized zones containing valuable metals such as gold, silver, copper, lead, and zinc as well as with coal deposits (Chandra and Gerson, 2010; Monterroso and Macıas, 1998; Tabelin and Igarashi, 2009; Tabelin et al., 2012a). Pyrite is commonly separated from valuable minerals by mineral processing techniques and subsequently disposed of in tailings dams as wastes. Upon exposure to oxygen and water, pyrite is rapidly oxidized to form sulfuric acid. Sulfuric acid generated by pyrite oxidation could further enhance the dissolution of other minerals containing hazardous elements such as cadmium (Cd), arsenic (As) and lead (Pb) in the wastes (Jha et al., 2008; Tabelin et al., 2012b, 2017a, 2017b, 2017c, 2017d) and finally form a heavy metal-laden polluted acidic leachate called acid mine drainage (AMD). Table 1-1 and 1-2 summarized the major and minor components in AMD generated in coal or polymetallic mine worldwide as examples.

AMD is a serious environmental problem not only in the mining industry (Yuniati et al., 2015a, 2015b) but also in underground space development projects (e.g. roads and railway tunnels) (Tabelin et al., 2010, 2014a, 2014b; Tatsuhara et al., 2012). It is also a potential threat to surrounding ecosystems and the health of people living around AMD-polluted areas (Motsi et al., 2009; Simón et al., 2001; Yuniati et al., 2015a, 2015b). Once AMD is produced, water treatment like chemical neutralization is essential, which has to be continued for long periods of time (even after the closure of mines) (Mackie and Walsh, 2012). If pyrite oxidation could be suppressed, the treatment costs could be reduced and a more sustainable method to manage AMD could be developed.

Several authors have proposed a new and promising approach to suppress the oxidation of sulfide minerals like pyrite and arsenopyrite by directly passivating their surfaces in a process called carrier-microencapsulation (CME) (Jha et al., 2008, 2011; Park et al., 2018a, 2018b; Satur et al., 2007; Yuniati et al., 2015b). In this technique, metal (or metalloid) ions with low solubility are

Table 1-1 Major elements and pH of AMD in representative mines

Representative mine	pH	Fe (mg/L)	Al (mg/L)	Mn (mg/L)	Cu (mg/L)	Zn (mg/L)	References
Karaerik Cu mine,Turkey	2.2-2.5	573.0-1130.1	119.7-158.1	-	48.8-71.4	35.1-53.1	Sağlam et al. (2016)
Dabaoshan polymetallic mine, China	2.7	520	168	116.7	60.4	80.1	Chen et al. (2015)
Fanko Pb-Zn mine China	1.9	1240	53	13.7	4.4	144.5	
Yunfu pyrite mine, China	2.5-2.7	2060-2230	117-1878	27.7-145.7	0.02-0.06	4.9-80.9	
Tongling, China	2.1-3.5	8.5-151.8	5.0-33.7	0.7-6.2	1.5-6.4	0.4-11.4	Yang et al. (2014)
Santa Lucia, Zn-Pb min, Cuba	2.5-2.7	264-4620	140-174	48.1-90.7	0.1-1.8	585-2090	Romero et al. (2010)
Iberian Pyrite Belt, Portugal	1.9-3.0	14.5-8215	22.1-1100	14-49	7-111	66-269	Ferreira da Silva et al. (2009)
Sextus Mine, Norway	3.09	18.8	6.5	0.2	4.0	5.8	Johnson et al. (2001)
Kings Mine	2.8-3.7	6.7-172	4.3-22.5	0.3-0.78	3.8-15.8	11.0-25.4	
Jaintia Coalfield, India	1.6-4.8	38.5-118.4	15.2-117.8	0.3-11.7	0.01-1.8	0.3-15.5	Sahoo et al. (2012)
Lamphun area coal mine, Thailand	2.4-5.9	1.4-331	0.7-28.4	3.0-24.2	0.02-0.2	0-1.7	Suteerapataranon et al. (2006)

Table 1-2 Minor elements of AMD in representative mines

Representative mine	Pb (μg/L)	Ni (μg/L)	Co (ug/L)	As (ug/L)	Cd (ug/L)	Cr (ug/L)	References
Karaerik Cu mine, Turkey	18-100	64-92	1022.5-1470.5	498-2153	138.2-209	--	Sağlam et al. (2016)
Dabaoshan polymetallic mine, China	190	--	--	--	400	110	Chen et al. (2015)
Fanko Pb/Zn mine China	230	--	--	--	250	390	
Yunfu pyrite, China	130-400	'--	--	--	10	210-230	
Tongling, China	40-4550	--	4-229	20-2920	7-48	-	Yang et al. (2014)
Santa Lucia, Zn-Pb min, Cuba	328-637	--	-	5-293	99.7-1230	-	Romero et al. (2014)
Iberian Pyrite Belt, Portugal	0-306	455-1349	1549-6499	0-36455	127-560	-	Ferreira da Silva et al. (2009)
Sextus Cu Mine, Norway	＜50	30	50	--	10	--	Johnson et al. (2001)
Kings Cu/pyrite Mine, Norway	＜50	10-30	20-170	--	20-60	--	
Jaintia Coalfield, India	10-1580	20-5150	20-1520	--	30	60	Sahoo et al. (2012)
Lamphun coal mine, Thailand	0.03	1.3-37	27-373	--	--	--	Suteerapataranon et al (2006)

stabilized in the aqueous phase by forming complexes with a carrier (i.e., organic ligand). On the surface of sulfide minerals, the complex is oxidatively decomposed releasing the metal (or metalloid) ions that are precipitated as oxide or hydroxide. These precipitates eventually cover the mineral surface and act as a protective coating to inhibit contact between sulfide minerals and oxidants, resulting in the suppression of their dissolution. The primary advantage of CME over other encapsulation techniques is its ability to specifically target pyrite and arsenopyrite in complex systems like mine waste and tailings. It has been reported that CME using Ti^{4+}-, Si^{4+}-, and Al^{3+}-catecholate complexes are effective to suppress pyrite and arsenopyrite oxidation (Belzile et al., 1997; Jha et al., 2008, 2011; Nyavor et al., 1996; Park et al., 2018a, 2018b; Satur et al., 2007).

When the application of CME in an actual mine is considered, it is important to know how coexisting minerals and metal ions affect pyrite oxidation and coating formation during CME. Most common and important coexisting metal ions/minerals are iron ions (Fe^{3+} and Fe^{2+}) and Fe oxyhydroxides/oxides. For example, in iron oxide copper gold ore deposits (IOCG), an important copper source, magnetite (Fe_3O_4) is the dominant Fe-containing mineral that exists together with pyrite and chalcopyrite ($CuFeS_2$). In tailings dams, a significant amount of Fe^{3+} and Fe^{2+} exsit in aqueous phase together with iron-containing secondary minerals like hematite, goethite, akageneite and schwertmannite (Durocher and Schindler, 2011). It is known that Fe^{3+} and Fe^{2+} could form water-soluble complexes with catechol (Avdeef et al., 1978; Hider et al., 1981, 1983; Schweigert et al., 2001; Sever and Wilker, 2004), and that catechol has the ability to extract Fe from its mineral (Gulley-Stahl et al., 2010). Therefore, when CME is applied in actual mining operations, Fe^{3+}-catecholate complexes would be formed and it is of great importance to understand how Fe^{3+}-catecholate complexes affecting pyrite oxidation and Ti^{4+}-based CME.

The objectives of this study are four-fold:

(1) to compare the redox and thermodynamic properties of Fe^{3+}-catecholate complexes with Al^{3+}- and Ti^{4+}-catecholate complexes

(2) to investigate the effects of Fe^{3+}-catecholate complexes on pyrite oxidation

(3) to examine the effects of Fe^{3+}-catechol derivative complexes on pyrite oxidation

(4) to understand the effects of Fe^{3+}-catecholate complexes on Ti-based CME

1.2 Literature review

1.2.1 Pyrite

Pyrite (FeS_2) is the most wide-spread sulfide mineral in the earth crust (Bonnissel-Gissinger et al., 1998). It was commonly found in sedimentary beds and igneous rocks, massive hydrothermal deposits, vein and replacements (Chandra and Gerson, 2010; Holmes and Crundwell, 2000). It is frequently associated with valuable sulfide minerals, gold, and coal (Lin and Say, 1999). Pyrite is ideally composed of a ferrous cation (Fe^{2+}) and a disulfide anion (S_2^{2-}) with a ratio of 1:1 (Dana, 1864), however, due to lattice substitutions of Fe^{2+} or S^{2-} with atoms of similar radius or charge of net polarity, the ratio of Fe^{2+} and S^{2-} in natural pyrite was reported frequently to be greater or smaller than the ideal value (Chandra and Gerson, 2010; Hurlbut et al., 1977). The analysis results showed pyrite could contain a variety of trace element like Ag, As, Au, Bi, Cd, Co, Cu, Hg, Mo, Ni, Pb, Pd, Ru, Sb, Se, Te and Zn (Rimstidt and Vaughan, 2003). The crystal structure of pyrite is commonly reported as face-centered cubic, which is similar to halite (NaCl) and rarely as dodecahedron (Bragg W.L. and Bragg W.H., 1914; Chandra and Gerson, 2010; Uhlig et al., 2001). Besides, another mineral having the same chemical composition, marcasite, which is less stable and less widespread, was reported to be orthorhombic (Hurlbut et al., 1977; Wiersma and Rimstidt, 1984).

Pyrite is semiconductor (electron mobility, 230 $cm^2V^{-1}S^{-1}$, optical absorption coefficient; $\alpha > 6.0 \times 105$ cm for $hv > 1.3$ eV) (Banerjee et al., 1990; Chandra and Gerson, 2010; Ferreira da Silva et al., 2009). Nature pyrite exists as either n-type or p-type semiconductor due to geological formation condition (Gupta et al., 1980), presence of trace elements (Rimstidt and Vaughan, 2003), stoichiometry of Fe^{2+} and S_2^{2-} (Chandra and Gerson, 2010) and etc: n-type of pyrite was normally formed at relatively high temperatures while p-type was normally formed at relatively lower temperature (Abraitis et al., 2004). Pyrite is found to be p-type when it contains high electron-donating trace element such as As and to be n-type when it contains high electron accepting element such as cobalt (Abraitis et al., 2004; Savage et al., 2008). Pyrite with S : Fe stoichiometric ratio above 2 are usually behaves as p-type while those less than 2 are usually n–type (Chandra and

Gerson, 2010). It also reported that in a single natural pyrite specimen, alternating n and p type properties exist while the overall properties depend on the net properties of n or p properties (Abraitis et al., 2004; Rimstidt and Vaughan, 2003). The conductivity of pyrite was reported be varied widely between 0.02 to 562 $(\Omega\cdot\mathrm{cm})^{-1}$ (average value of 48 $(\Omega\cdot\mathrm{cm})^{-1}$) (Doyle and Mirza, 1996; Pridmore and Shuey, 1976). Generally, n-type pyrite shows much higher conductivity than p-type pyrite.

1.2.2 Pyrite oxidation

1.2.2.1 General description

Pyrite oxidation is a ubiquitous reaction in nature and the main contributor to formation of acid mine drainage (Chandra and Gerson, 2010). Upon exposure to oxygen and water, pyrite is rapidly oxidized to form sulfuric acid according to the following reaction (Biegler and Swift, 1979; Holmes and Crundwell, 2000; Johnson and Hallberg, 2005; Todd et al., 2003):

$$2\ FeS_2 + 7\ O_{2\ (aq)} + 2\ H_2O \rightarrow 2\ Fe^{2+} + 4\ SO_4^{2-} + 4\ H^+ \quad (1\text{-}1)$$

Pyrite dissolution is further promoted in the presence of ferric ions (Fe^{3+}), a strong oxidant of pyrite (Eq. 1-2), which is produced from the oxidation of ferrous ions (Fe^{2+}) by O_2 and/or the mediation of ironoxidizing bacteria (Eq. 1-3) (Garrels and Thompson, 1960; Plaza et al., 2017; Singer and Stumm, 1970).

$$FeS_2 + 14\ Fe^{3+} + 8\ H_2O \rightarrow 15\ Fe^{2+} + 2\ SO_4^{2-} + 16\ H^+ \quad (1\text{-}2)$$

$$4\ Fe^{2+} + O_{2(aq)} + 4\ H^+ \rightarrow 4\ Fe^{3+} + 2\ H_2O \quad (1\text{-}3)$$

1.2.2.2 Electrochemical mechanism

Pyrite oxidation in aqueous condition could be mainly considered as an electrochemical process consisting of three more or less simultaneous but distinct processes, that is, (1) cathode reaction, (2) electron transport and (3) anode reaction (Rimstidt and Vaughan, 2003).

On cathode of pyrite, oxygen or Fe^{3+} could obtain electron(s) from pyrite and be reduced to H_2O or Fe^{2+} as shown in Eqs. 1-4 and 1-5

$$O_2 + 4\ H^+ + 4\ e^- \rightarrow 2\ H_2O \quad (1\text{-}4)$$

$$Fe^{3+} + e^- \rightarrow Fe^{2+} \quad (1\text{-}5)$$

As shown in Eq. 1-4, during the reduction of O_2 on pyrite cathode, four electrons were transferred from pyrite to O_2. The electron transfer process was proposed as a Fenton type reaction by Lowson (1982). Firstly, adsorption of O_2 at Fe^{2+} site on pyrite surface occurs and one electron is transferred from pyrite to O_2.

$$\text{py-Fe}^{2+}\cdots O_2 \rightarrow \text{py-Fe}^{3+}\cdots O_2^- \tag{1-6}$$

Then, a H^+ ion reacts with O_2^- to form HO_2 (Eq. 1-7), and concurrently, an electron transfers from anodic site of pyrite to reduce the Fe^{3+} on pyrite surface back to Fe^{2+} (Eq. 1-8). Until this step, the transfer of first electron from pyrite to O_2 finishes.

$$\text{py-Fe}^{3+}\cdots O_2 + H^+ \rightarrow \text{py-Fe}^{3+}\cdots O_2H \tag{1-7}$$

$$e^- + \text{py-Fe}^{3+}\cdots O_2H \rightarrow \text{py-Fe}^{2+}\cdots O_2H \tag{1-8}$$

One more electron transfer from Fe^{2+} on pyrite surface (Eq. 1-9) to HO_2 group to form HO_2^- group (Eq. 1-9) and a H^+ ion in the solution could combine with HO_2^- to form H_2O_2 (Eq. 1-10).

$$\text{py-Fe}^{2+}\cdots O_2H \rightarrow \text{py-Fe}^{3+}\cdots O_2H^- \tag{1-9}$$

$$\text{py-Fe}^{3+}\cdots O_2H^- + H^+ \rightarrow \text{py-Fe}^{3+}\cdots O_2H_2 \tag{1-10}$$

Concurrently, one more electron transfer from anodic site of pyrite and reduce Fe^{3+} on pyrite surface to Fe^{2+} (Eq. 1-11). Second electron is transferred in this step.

$$e^- + \text{py-Fe}^{3+}\cdots O_2H_2 \rightarrow \text{py-Fe}^{2+}\cdots O_2H_2 \tag{1-11}$$

With one more electron transfers from Fe^{2+} to H_2O_2, H_2O_2 decomposes to form one $\cdot OH$ radical and one hydroxide ion (OH^-) (Eq. 1-12). OH^- releases to solution while $\cdot OH$ radical continues to participate in electron transfer on pyrite surface. Simultaneously, one electron transfers from anodic site of pyrite to reduce Fe^{3+} on pyrite surface to Fe^{2+}. By this step, the third electron are transferred.

$$\text{py-Fe}^{2+}\cdots O_2H_2 \rightarrow \text{py-Fe}^{3+}\cdots \cdot OH + OH^- \tag{1-12}$$

$$e^- + \text{py-Fe}^{3+}\cdots \cdot OH \rightarrow \text{py-Fe}^{2+}\cdots \cdot OH \tag{1-13}$$

Finally, one electron transfers from Fe^{2+} to $\cdot OH$, making $\cdot OH$ become OH^- (Eq. 1-14). At the same time, Fe^{3+} on pyrite surface is reduced to Fe^{2+} by obtaining one electron from anodic site of pyrite (Eq. 1-15).

$$\text{py-Fe}^{2+}\cdots \cdot OH \rightarrow \text{py-Fe}^{3+}\cdots + OH^- \tag{1-14}$$

$e^- + \text{py-Fe}^{3+} \rightarrow \text{py-Fe}^{2+}$ (1-15)

For the oxidation of pyrite by Fe^{3+} in aqueous condition, the presence of Fe^{3+} is considered as hydrated complex species, $Fe^{3+}(H_2O)_6$. When $Fe^{3+}(H_2O)_6$ absorbed on Fe site of pyrite, electron transfer from Fe^{2+} on pyrite surface to $Fe^{3+}(H_2O)_6$ occurs and results in the reduction of $Fe^{3+}(H_2O)_6$ to $Fe^{2+}(H_2O)_6$ (Eq. 1-16). After that, $Fe^{2+}(H_2O)_6$ is released into the solution and concurrently, one electron transfers from anode site of pyrite to reduce the Fe^{3+} on pyrite surface to Fe^{2+} (Eq. 1-17).

$\text{py-Fe}^{2+\cdots}Fe^{3+}(H_2O)_6 \rightarrow \text{py-Fe}^{3+} + Fe^{2+}(H_2O)_6$ (1-16)

$e^- + \text{py-Fe}^{3+} \rightarrow \text{py-Fe}^{2+}$ (1-17)

The transfer of electron from anodic site to cathodic site can be considered as the second distinct process during pyrite oxidation. This process could be affected by the conductivity of pyrite which was already discussed in the previous subsection.

For anodic reaction of pyrite oxidation, S_2^{2-} in pyrite lose 14 electrons and pyrite dissolves as Fe^{2+}, SO_4^{2-} and H^+ as oxidized product (Eq. 1-18).

$FeS_2 + 8\ H_2O \rightarrow Fe^{2+} + 2SO_4^{2-} + 16\ H^+ + 14\ e^-$ (1-18)

In Eq. 1-18, one sulfur atom loses 7 electrons and this process is also proposed as multi-step described as follows.

$\text{py-S-S} \rightarrow \text{py-S-S}^+ + e^-$ (1-19)

$\text{py-S-S}^+ + H_2O \rightarrow \text{py-S-S-OH} + H^+$ (1-20)

$\text{py-S-S-OH} \rightarrow \text{py-S-SO} + e^- + H^+$ (1-21)

$\text{py-S-SO} \rightarrow \text{py-S-SO}_2 + 2\ e^- + 2\ H^+$ (1-22)

$\text{py-S-SO}_2 \rightarrow \text{py-S-SO}_3 + 2\ e^- + 2\ H^+$ (1-23)

$\text{py-S-SO}_3 \rightarrow \text{py-S} + HSO_4^- + e^-$ (1-24)

1.2.3 Prevention techniques of AMD

As illustrated in the previous section, oxidant (O_2 and Fe^{3+}), water, iron-oxidizing bacteria were involved in pyrite oxidation as important roles (Park et al., 2019). If one or more than one component mentioned above could be excluded from reaction with pyrite, pyrite oxidation could be suppressed, resulting in the limitation of AMD formation. Based on this strategy, many techniques were proposed as alternative methods to prevent/suppress AMD by suppressing pyrite oxidation. These methods could be classified into three major groups: (1) physical barrier, (2) bactericidal control and (3) surface passivation.

1.2.3.1 Physical barrier

The most common technique to passivate the contact between H_2O or/and O_2 and sulfide tailings is the application of physical barrier that includes dry and wet covers (Evangelou, 2018; Kleinmann, 1990). As for dry cover, materials like fine-grained soil or soil substitute, none-reactive fine mine residues, organic materials, alkaline wastes and AMD remediation sludges, were reported to be effective in suppressing AMD formation. Yanful and Payant (1992) reported that comparing to uncovered tailings, acid generation was decreased by three-orders when soil cover was applied. While some authors also mentioned that high maintenance cost was needed for this method (Sahoo et al., 2013). Bussière et al. (2004) studied the feasibility of application of low-sulfide tailings as a dry cover with capillary barrier effect material by column leaching experiments for around 400 days. The results showed this method could not only suppress the acid generation but also passivate the dissolution of metals like Fe and Zn.

Caruccio (1983) applied a plastic cover in a field study in West Virginia to reduce AMD formation. Although the result was reported to be promising, the cost of this technique was highly dependent on the covering area and maintenance, which may preclude the application in the tailing site with wide area (Sahoo et al., 2013; Skousen and Foreman, 2000). Industrial wastes, such as fly ash (Mollamahmutoğlu and Yilmaz, 2001), red mud bauxite and/ or cement kiln dust (Duchesne and Doye, 2005), desulphurized tailings (Demers et al., 2008) and AMD neutralization sludge (Demers et al., 2017) were also investigated as materials for dry cover to suppress the AMD generation.

In addition, dry covers made of organic wastes, such as paper-mill waste (Bellaloui et al., 1999), pulp/paper residue (Cabral et al., 2000), wood waste/chips, vegetation and peat (Peppas et al., 2000) were also proposed as alternative materials as dry cover. Except for the function as physical oxygen barrier, organic wastes could suppress AMD formation due to additional three mechanisms: (1) pH buffering effects. Organic wastes could neutralize acid, which could suppress the activity of iron-oxidizing bacteria (Sahoo et al., 2013). (2) Consumption of O_2 due to decomposition of carbon-rich compounds by microorganisms (Park et al., 2019). (3) Suppressing the oxidizing ability of Fe^{3+} due to complexation between Fe^{3+} and organic compounds (Pandey et al., 2011). However, however, due to the presence of organic acid and other complexing agents in organic waste, toxic metals may be extracted from co-existing minerals (Pond et al., 2005); it was also reported that organic cover may cause the reductive dissolution of secondary iron-oxyhydroxide, and result in the release of toxic elements (i.e., As, Cu, Pb, Cd and Se) which previously adsorbed onto or coprecipitated on secondary iron-oxyhydroxide into aqueous environment (Ribeta et al., 1995).

Disposal of sulfide-rich tailings under water (wet cover) is widely used as a technique to suppress the generation of AMD. This is primarily because the diffusion rate of O_2 is 4 orders of magnitude slower than that in air (Awoh et al., 2013; Moncur et al., 2015). Moncur et al. (2015) conducted a long-term test with 100 cm water cover on sulfide tailing surface and the results were compared to that obtained in the absence of cover. The results showed that the tailings without the cover were highly oxidized while the one with the cover were mildly oxidized. Moreover, the analysis of pore water collected from sub-aerial and sub-aqueous tailings with the water cover showed higher pH, lower concentration of Fe and S than without the cover, indicating the formation of AMD was suppressed by water cover effectively. However, some authors also reported that water cover may not gave a long-term effect. Vigneault et al. (2001) found a clear evidence of sulfide oxidation and mobilization of Zn and Cd when experiments exceeded 2 years. This technique may be problematic in the area where annual evaporation exceed precipitation because the decrease of water may allow tailings to be exposed to atmosphere and generate AMD (Lottermoser, 2007).

1.2.3.2 Bactericidal control

Pyrite oxidation could be accelerated with presence of acidophilic iron- (e.g., *Acidithiobacillus ferroxidans*) and sulfur-oxidizing bacteria (e.g., *Acidithiobacillus thiooxidans*), so the limitation of AMD generation could be achieved by inhibiting the activity of those bacteria (Evangelou, 2018). Sodium lauryl or sodium dodecyl sulfate, which was widely used in cleaning detergents as anodic surfactants, was reported to be effective in red acid generation by 60-95% (Kleinmann and Erickson, 1984). In addition, food preservatives and organic acids have also been proposed as bactericide to reduce the generation of AMD (Sahoo et al., 2013). Utilization of bactericide cannot completely kill microorganisms but reduce their population and activity. The effect of bactericide cannot be permanent because bactericides are generally water-soluble and leach out from tailings, so repetitive addition of bactericide are needed for maintaining the low level of bacterial activities (Park et al., 2019). Although suppressing pyrite oxidation by addition of bactericides is a more cost-effective technique than dry/wet cover, application of bactericides to natural AMD raises a serious concern due to their aquatic toxicity (Hodges et al., 2006; Liwarska-Bizukojc et al., 2005; Sahoo et al., 2013).

1.2.3.3 Surface passivation

Surface passivation could suppress pyrite oxidation by forming a protective coating on pyrite surface, which could block the approach of oxidants to pyrite. Depending on the mechanism of coating formation, the techniques of surface passivation could be divided into surface absorption, microencapsulation and carrier-microencapsulation.

- Surface absorption

Many organic compounds could absorb on pyrite surface by physical and/or chemical absorption to form organic coating. For instance, the disodium salt of 1,3-benzendiamidoethanthiol (Na_2BDET), a strong coordination ligand to divalent metal, was found to form Fe-BDET linkages along pyrite lattice, resulting in the suppression of pyrite dissolution (Matlock et al., 2001; Osterloh et al., 1998). Matlock et al. (2003) reported that by applying this technique, 97.5% and 99.3% reduction of Fe dissolution in coal cleaning were achieved at pH 3 and 6.5, respectively. Zaman et al.

(2007) also confirmed that the suppressive effect was achieved even under strong acidic condition (pH 1) over 1 month.

Lan et al. (2002) has proposed a method using 8-hydroxyquinoline (C_9H_7NO) because it could form a very indissoluble precipitate with Fe^{3+} ($Fe(C_9H_6NO)_3$, $k_{sp} = 3\times10^{-44}$) on pyrite surface, suppressing both chemical dissolution and biological reaction on pyrite surface. However, iron 8-hydroxyquinoline could be dissolved in strong acid condition, suggesting that this method should be applied on fresh sulfide tailings before AMD generation. Since 8-hydroxyquinoline was reported to be toxic for aquatic organisms, the environmental effects of this technique are required to be fully assessed (Sahoo et al., 2013).

Phospholipids, which are consisted of one hydrophilic head and two hydrophobic tails, were used to control pyrite oxidation (Elsetinow et al., 2003; Evangelou and Zhang, 1995). The hydrophilic head of phospholipids are more easily to absorb on pyrite surface, which makes the hydrophobic tails toward solution phase (Park et al., 2019; Zhang et al., 2003a). Zhang et al. (2003a) examined the effect of L-α-phosphatidylcholine and 1,2-bis(10,12-tricosadiynoyl)-sn-glycero-3-phosphocholine on pyrite oxidation by conducting a laboratory experiment and the results indicated the suppressive effect could be achieved even under strong acidic condition (pH < 2). However, such suppressive effect was not experimentally observed by 1,2-dipropionoyl-*sn*-glycero-3-phosphocholine, a two tailed lipid with short chain, indicating the suppressive effect of phospholipid was highly dependent on the length of hydrophobic tails. In addition, the pretreatment of UV radiation induced the formation of crosslinks of hydrophobic tails, which could strongly suppress pyrite oxidation under the presence of *A. ferrooxidans* up to 30 days (Zhang et al., 2003b). Comparing to many organic regents, the phospholipids are inexpensive and environment-friendly (Elsetinow et al., 2003). Kargbo et al. (2004) reported that the suppressive effect of phospholipids became weaker in presence of silicate, a common anion in the AMD. The stability of phospholipid coatings for long-term was not well evaluated yet (Sahoo et al., 2013).

Fatty acids, which are widely used as collector for flotation of oxide mineral, was also reported to be effective in suppressing pyrite oxidation. This is because fatty acids could not only increase hydrophobicity of pyrite that reduces the interaction between mineral and water, but also form a protective coating that physically limited the reactive area on pyrite surface (Jiang et al., 2000; Nyavor et al., 1996). In addition, other organic reagents, such as humic acid, ligin, oxalic acid, polyethylene polyamine (diethylenetriamine (DETA), triethylentermine (TETA), sodium triethylenetetramine-bisdithiocarbamate (DTC-TETA)) were also reported to be effective in suppressing pyrite oxidation (Ačai et al., 2009; Belzile et al., 1997; Chen et al., 2006; Lalvani et al., 1996; Liu et al., 2013; Shu et al., 2017).

- Microencapsulation

Microencapsulation was firstly proposed by (Huang and Evangelou, 1992) as a new technique to suppress pyrite oxidation by forming iron-phosphate coating on pyrite surface. In this technique, hydrogen peroxide (H_2O_2), phosphate and sodium acetate (CH_3COONa) were applied for pretreatment. H_2O_2 firstly oxidized pyrite to release Fe^{3+} and the released Fe^{3+} was precipitated with phosphate to form iron-phosphate as insoluble coating on pyrite surface (Evangelou, 1995, 2001; Evangelou and Zhang, 1995). The suppressive effect of this method was also confirmed by the other researchers (Cárdenes Van den Eynde et al., 2009; Elsetinow et al., 2001; Georgopoulou et al., 1996; Harris and Lottermoser, 2006; Nyavor and Egiebor, 1995; Vandiviere and Evangelou, 1998). Due to the use of phosphate and H_2O_2, the demerits of this technique are apparent (Park et al., 2019). Addition of phosphate raised a risk for eutrophication in natural ecosystems (Khummalai and Boonamnuayvitaya, 2005) and handling the dosage of H_2O_2 would become difficult in large scale application (Ouyang et al., 2015). Iron-phosphate was also reported to be ineffective in suppressing pyrite oxidation with presence of sulfide oxidizing bacteria or in acidic condition ($pH < 4$) (Evangelou, 1995; Lan et al., 2002). Another microencapsulation technique was proposed by Evangelou (1996) using silicate instead of phosphate. Silicate could absorb on oxidized surface of pyrite and form an iron hydroxide-silica coating. Zhang and Evangelou (1998) reported that with application of silicate-based microencapsulation for 1000 min, only 10% of sample was oxidized, which is much lower than the result (65%) obtained in the control experiment. In addition, comparative studies indicated that ferric-hydroxide-silica coating gave a better performance than ferric-phosphate coating.

Although the development of silicate-based microencapsulation could overcome the drawback of phosphate, the addition of H_2O_2 was still necessary in this technique. A H_2O_2-free method using organosilane, such as methyltrimethoxysilane (MTMOS), tetramethoxysilane (TMOS), tetraethoxysilane (TEOS), N-(2-aminoethyl)-3-aminopropyl trimethoxysilane (AAPS), n-polyltrimethoxysilane (NPS), γ-aminopropyltrimethoxysilane (APS) and vinyltrimethoxysilane (VTMS) was proposed (Diao et al., 2013; Khummalai and Boonamnuayvitaya, 2005; Ouyang et al., 2015; You et al., 2013). The hydrolyzed product of organosilane in water absorbed on pyrite surface and formed silica-like coating. Due to the incomplete decomposition, some organic functional groups were also present in the coating, which could increase the hydrophobicity and crack-resistibility of the coating. Khummalai and Boonamnuayvitaya (2005) studied the effect of TMOS, TEOS, AAPS on prevention of arsenopyrite (FeAsS) and the results suggested that the coating formed by MTMOS was most effective in suppressing the chemical and biological reaction of pyrite oxidation. Ouyang et al. (2015) examined the suppressive effect of γ-mercatopropyltrimethoxysilane (Prop-SH), APS and VTMS on pyrite oxidation via an electrochemical method, although the result of Prop-SH was not promising, APS and VTMS could suppress the electrochemical reactions of pyrite oxidation. The application of organosilane on treatment of actual sulfide-rich tailings may be limited due to the high cost of the regents (Sahoo et al., 2013).

- Carrier-microencapsulation

The microencapsulation techniques described in last subsection could suppress pyrite oxidation by forming a passivated coating. These techniques can not specifically target on the pyrite, which is the main contributor to AMD formation in real tailing systems (Park et al., 2019). Comparing with the conventional microencapsulation techniques, carrier-microencapsulation (CME) is more promising because of its ability to specifically target pyrite and arsenopyrite even in complex systems containing quartz and aluminosilicates (Park et al., 2018b). In this technique, redox-sensitive organic complexes synthesized from metal(loid) ions (e.g., Ti^{4+}, Si^{4+}, and Al^{3+}) and catechol (1,2-dihydroxybenzene) are used as coating agents (Jha et al., 2008, 2011, 2012; Li et al., 2019a, 2019b; Park et al., 2018a, 2018b; Satur et al., 2007; Yuniati et al., 2015a, 2015b). Because pyrite dissolves electrochemically, the metal(loid)-catecholate complexes are selectively oxidized on anodic sites of pyrite (Eq. 1-25) as O_2 is reduced on cathodic sites of the mineral (Eq. 1-4).

$[M^{n+}(cat)_3]^{n-6} \rightarrow M^{n+} + 3\ Q + 6\ e^-$ (M^{n+}: Ti^{4+}, Si^{4+} or Al^{3+}; Q: $C_6H_6O_2$, 1,2-benzoquinone) (1-25)

Decomposition of the redox sensitive complexes releases their metal(loid) ions, which precipitates on the surface of pyrite to form a protective coating against further exposure to oxidants. Previous studies have shown that CME using Ti^{4+}- and Al^{3+}-catecholate complexes could suppress not only the oxidation of sulfide minerals like pyrite but also the release of toxic arsenic from arsenopyrite (Park et al., 2018a, 2018b; Satur et al., 2007). Moreover, pyrite with CME using Si^{4+}-catecholate complexes were stable even in the presence of iron-oxidizing bacteria (Yuniati et al., 2015b). Another advantage of CME is its ability to form hydrophilic coatings on pyrite, which could improve the separation efficiency of this mineral from hydrophobic coal by flotation (Jha et al., 2011, 2008).

1.3 Outline of the dissertation

The dissertation is comprised of seven chapters and the contents of each chapters are outlined as follows:

Chapter 1 states the problem and objectives of this study and reviews the previous studies on pyrite, pyrite oxidation and prevention techniques for AMD formation.

Chapter 2 compares the redox and thermodynamic properties of Fe^{3+}-, Al^{3+}- and Ti^{4+}-catecholate complexes.

Chapter 3 examines the effect of ferric-catecholate complexes on pyrite oxidation

Chapter 4 explains the mechanism of suppressive effect of ferric-catecholate complexes on pyrite oxidation by electrochemical study.

Chapter 5 evaluates the effects of ferric-catechol derivative complexes on pyrite oxidation.

Chapter 6 investigates the effects of ferric-catecholate complexes on Ti-based CME.

Chapter 7 presents the summary and conclusions of this dissertation.

References

Abraitis, P.K., Pattrick, R.A.D., Vaughan, D.J., 2004. Variations in the compositional, textural and electrical properties of natural pyrite: a review. Int. J. Miner. Process. 74, 41–59.

Ačai, P., Sorrenti, E., Gorner, T., Polakovič, M., Kongolo, M., de Donato, P., 2009. Pyrite passivation by humic acid investigated by inverse liquid chromatography. Colloids Surf. Physicochem. Eng. Asp. 337, 39–46.

Avdeef, A., Sofen, S.R., Bregante, T.L., Raymond, K.N., 1978. Coordination chemistry of microbial iron transport compounds. 9. Stability constants for catechol models of enterobactin. J. Am. Chem. Soc. 100, 5362–5370.

Awoh, A.S., Mbonimpa, M., Bussière, B., 2013. Determination of the reaction rate coefficient of sulphide mine tailings deposited under water. J. Environ. Manage. 128, 1023–1032.

Banerjee, H.D., Godhaunkar, N., Pal, U., 1990. Upgradation and studies on semiconducting properties of pyrite (FeS2) for device applications. Mater. Lett. 10, 99–104.

Bellaloui, A., Chtaini, A., Ballivy, G., Narasiah, S., 1999. Laboratory Investigation of the Control of Acid Mine Drainage Using Alkaline Paper Mill Waste. Water. Air. Soil Pollut. 111, 57–73.

Belzile, N., Maki, S., Chen, Y.-W., Goldsack, D., 1997. Inhibition of pyrite oxidation by surface treatment. Sci. Total Environ. 196, 177–186.

Biegler, T., Swift, D.A., 1979. Anodic behaviour of pyrite in acid solutions. Electrochimica Acta 24, 415–420.

Bonnissel-Gissinger, P., Alnot, M., Ehrhardt, J.-J., Behra, P., 1998. Surface Oxidation of Pyrite as a Function of pH. Environ. Sci. Technol. 32, 2839–2845.

Bragg W.L., Bragg W.H., 1914. The analysis of crystals by the X-ray spectrometer. Proc. R. Soc. Lond. Ser. Contain. Pap. Math. Phys. Character 89, 468–489.

Bussière, B., Benzaazoua, M., Aubertin, M., Mbonimpa, M., 2004. A laboratory study of covers made of low-sulphide tailings to prevent acid mine drainage. Environ. Geol. 45, 609–622.

Cabral, A., Racine, I., Burnotte, F., Lefebvre, G., 2000. Diffusion of oxygen through a pulp and paper residue barrier. Can. Geotech. J. 37, 201–217.

Cárdenes Van den Eynde, V., Paradelo, R., Monterroso, C., 2009. Passivation techniques to prevent corrosion of iron sulphides in roofing slates. Corros. Sci. 51, 2387–2392.

Caruccio, F.T., 1983. The Effect of Plastic Liner on Acid Loads/DLM Site, W.V. Presented at the Proceedings, Proceedings, fourth annual West Virginia surface mine drainage task force symposium, p. 7.

Chandra, A.P., Gerson, A.R., 2010. The mechanisms of pyrite oxidation and leaching: A fundamental perspective. Surf. Sci. Rep. 65, 293–315.

Chen, L., Hu, M., Huang, L., Hua, Z., Kuang, J., Li, S., Shu, W., 2015. Comparative metagenomic and metatranscriptomic analyses of microbial communities in acid mine drainage. ISME J. 9, 1579–1592.

Chen, Y., Li, Y., Cai, M., Belzile, N., Dang, Z., 2006. Preventing oxidation of iron sulfide minerals by polyethylene polyamines. Miner. Eng. 19, 19–27.

Dana, J.D., 1864. Manual of Mineralogy.

Demers, I., Bussière, B., Benzaazoua, M., Mbonimpa, M., Blier, A., 2008. Column test investigation on the performance of monolayer covers made of desulphurized tailings to prevent acid mine drainage. Miner. Eng., Selected Papers from Processing and Disposal of Minerals Industry Wastes ’07, Falmouth, UK, June 2007 21, 317–329.

Demers, I., Mbonimpa, M., Benzaazoua, M., Bouda, M., Awoh, S., Lortie, S., Gagnon, M., 2017. Use of acid mine drainage treatment sludge by combination with a natural soil as an oxygen barrier cover for mine waste reclamation: Laboratory column tests and intermediate scale field tests. Miner. Eng., Sustainable Minerals 107, 43–52.

Diao, Z., Shi, T., Wang, S., Huang, X., Zhang, T., Tang, Y., Zhang, X., Qiu, R., 2013. Silane-based coatings on the pyrite for remediation of acid mine drainage. Water Res. 47, 4391–4402.

Doyle, F.M., Mirza, A.H., 1996. Electrochemical oxidation of pyrite samples with known composition and electrical properties, in: Proceedings of the Fourth International Symposium on Electrochemistry in Mineral and Metal Processing. pp. 203–214.

Duchesne J., Doye I., 2005. Effectiveness of Covers and Liners Made of Red Mud Bauxite and/or Cement Kiln Dust for Limiting Acid Mine Drainage. J. Environ. Eng. 131, 1230–1235.

Durocher, J.L., Schindler, M., 2011. Iron-hydroxide, iron-sulfate and hydrous-silica coatings in acid-mine tailings facilities: A comparative study of their trace-element composition. Appl. Geochem. 26, 1337–1352.

Elsetinow, A.R., Borda, M.J., Schoonen, M.A.A., Strongin, D.R., 2003. Suppression of pyrite oxidation in acidic aqueous environments using lipids having two hydrophobic tails. Adv. Environ. Res. 7, 969–974.

Elsetinow, A.R., Schoonen, M.A.A., Strongin, D.R., 2001. Aqueous Geochemical and Surface Science Investigation of the Effect of Phosphate on Pyrite Oxidation. Environ. Sci. Technol. 35, 2252–2257.

Evangelou, V.P., 2018. Pyrite Oxidation and Its Control. CRC Press.

Evangelou, V.P., 2001. Pyrite microencapsulation technologies: Principles and potential field application. Ecol. Eng. 17, 165–178.

Evangelou, V.P., 1996. Oxidation Proof Silicate Surface Coating on Iron Sulfides. U.S. Patent, Patent Number 5,494,703.

Evangelou, V.P., 1995. Potential Microencapsulation of Pyrite by Artificial Inducement of Ferric Phosphate Coatings. J. Environ. Qual. 24, 535–542.

Evangelou, V., L. Zhang, Y., 1995. A Review: Pyrite Oxidation Mechanisms and Acid Mine Drainage Prevention. Crit. Rev. Environ. Sci. Technol. 25, 141–199.

Ferreira da Silva, E., Bobos, I., Xavier Matos, J., Patinha, C., Reis, A.P., Cardoso Fonseca, E., 2009. Mineralogy and geochemistry of trace metals and REE in volcanic massive sulfide host rocks, stream sediments, stream waters and acid mine drainage from the Lousal mine area (Iberian Pyrite Belt, Portugal). Appl. Geochem. 24, 383–401.

Georgopoulou, Z.J., Fytas, K., Soto, H., Evangelou, B., 1996. Feasibility and cost of creating an iron-phosphate coating on pyrrhotite to prevent oxidation. Environ. Geol. 28, 61–69.

Gulley-Stahl, H., Hogan, P.A., Schmidt, W.L., Wall, S.J., Buhrlage, A., Bullen, H.A., 2010. Surface complexation of catechol to metal oxides: an ATR-FTIR, adsorption, and dissolution study. Environ. Sci. Technol. 44, 4116–4121.

Gupta, V.P., Ravindra, N.M., Srivastava, V.K., 1980. Semiconducting properties of pyrite. J. Phys. Chem. Solids 41, 145–148.

Harris, David L., Lottermoser, B.G., 2006. Evaluation of phosphate fertilizers for ameliorating acid mine waste. Appl. Geochem. 21, 1216–1225.

Harris, D. L., Lottermoser, B.G., 2006. Phosphate stabilization of polymínerallic mine wastes. Mineral. Mag. 70, 1–13.

Hider, R.C., Howlin, B., Miller, J.R., Mohd-Nor, A.R., Silver, J., 1983. Model compounds for microbial iron-transport compounds. Part IV. Further solution chemistry and Mössbauer studies on iron (II) and iron (III) catechol complexes. Inorganica Chim. Acta 80, 51–56.

Hider, R.C., Mohd-Nor, A.R., Silver, J., G. Morrison, I.E., C. Rees, L.V., 1981. Model compounds for microbial iron-transport compounds. Part 1. Solution chemistry and Mössbauer study of iron (II) and iron (III) complexes from phenolic and catecholic systems. J. Chem. Soc. Dalton Trans., 609–622.

Hodges, G., Roberts, D.W., Marshall, S.J., Dearden, J.C., 2006. The aquatic toxicity of anionic surfactants to Daphnia magna—A comparative QSAR study of linear alkylbenzene sulphonates and ester sulphonates. Chemosphere 63, 1443–1450.

Holmes, P.R., Crundwell, F.K., 2000. The kinetics of the oxidation of pyrite by ferric ions and dissolved oxygen: an electrochemical study. Geochim. Cosmochim. Acta 64, 263–274.

Huang, X., Evangelou, V.P., 1992. Abatement of acid mine drainage by encapsulation of acid-producing geological material. Final research report, 1 August 1990-31 October 1992 (No. PB--93-202687/XAB). Kentucky Univ.

Hurlbut, C.S., 1906-, Klein, C., 1937-, 1977. Manual of mineralogy (after James D. Dana). Wiley.

Jha, R.K.T., Satur, J., Hiroyoshi, N., Ito, M., Tsunekawa, M., 2012. Suppression of Pyrite Oxidation by Carrier Microencapsulation Using Silicon and Catechol. Miner. Process. Extr. Metall. Rev. 33, 89–98.

Jha, R.K.T., Satur, J., Hiroyoshi, N., Ito, M., Tsunekawa, M., 2011. Suppression of floatability of pyrite in coal processing by carrier microencapsulation. Fuel Process. Technol. 92, 1032–1036.

Jha, R.K.T., Satur, J., Hiroyoshi, N., Ito, M., Tsunekawa, M., 2008. Carrier-microencapsulation using Si–catechol complex for suppressing pyrite floatability. Miner. Eng., 21, 889–893.

Jiang, C.L., Wang, X.H., Parekh, B.K., 2000. Effect of sodium oleate on inhibiting pyrite oxidation. Int. J. Miner. Process. 58, 305–318.

Johnson, D.B., Hallberg, K.B., 2005. Acid mine drainage remediation options: a review. Sci. Total Environ., Bioremediation of Acid Mine Drainage: The Wheal Jane Mine Wetlands Project 338, 3–14.

Johnson, D.B., Rolfe, S., Hallberg, K.B., Iversen, E., 2001. Isolation and phylogenetic characterization of acidophilic microorganisms indigenous to acidic drainage waters at an abandoned Norwegian copper mine. Environ. Microbiol. 3, 630–637.

Sever, M.J., Wilker, J.J, 2004. Visible absorption spectra of metal–catecholate and metal–tironate complexes. Dalton Trans. 0, 1061–1072.

Kargbo, D.M., Atallah, G., Chatterjee, S., 2004. Inhibition of Pyrite Oxidation by a Phospholipid in the Presence of Silicate. Environ. Sci. Technol. 38, 3432–3441.

Khummalai, N., Boonamnuayvitaya, V., 2005. Suppression of arsenopyrite surface oxidation by sol-gel coatings. J. Biosci. Bioeng. 99, 277–284.

Kleinmann, R.L., Erickson, P.M., 1984. Control of acid drainage from coal refuse using anionic surfactants.

Kleinmann, R.L.P., 1990. At-source control of acid mine drainage. Int. J. Mine Water 9, 85–96.

Lalvani, S.B., Zhang, G., Lalvani, L.S., 1996. Coal Pyrite Passivation Due to Humic Acids and Lignin Treatment. Fuel Sci. Technol. Int. 14, 1291–1313.

Lan, Y., Huang, X., Deng, B., 2002. Suppression of Pyrite Oxidation by Iron 8-Hydroxyquinoline. Arch. Environ. Contam. Toxicol. 43, 168–74.

Li, X., Gao, M., Hiroyoshi, N., Tabelin, C.B., Taketsugu, T., Ito, M., 2019a. Suppression of pyrite oxidation by ferric-catecholate complexes: An electrochemical study. Miner. Eng. 138, 226–237.

Li, X., Hiroyoshi, N., Tabelin, C.B., Naruwa, K., Harada, C., Ito, M., 2019b. Suppressive effects of ferric-catecholate complexes on pyrite oxidation. Chemosphere 214, 70–78.

Lin, H.K., Say, W.C., 1999. Study of pyrite oxidation by cyclic voltammetric, impedance spectroscopic and potential step techniques. J. Appl. Electrochem. 29, 987–994.

Liu, Y., Dang, Z., Xu, Y., Xu, T., 2013. Pyrite Passivation by Triethylenetetramine: An Electrochemical Study. J. Anal. Methods Chem.

Liwarska-Bizukojc, E., Miksch, K., Malachowska-Jutsz, A., Kalka, J., 2005. Acute toxicity and genotoxicity of five selected anionic and nonionic surfactants. Chemosphere 58, 1249–1253.

Lottermoser, B.G., 2007. Mine Wastes: Characterization, Treatment, Environmental Impacts. Berlin.

Lowson, R.T., 1982. Aqueous oxidation of pyrite by molecular oxygen. Chem. Rev. 82, 461–497.

Mackie, A.L., Walsh, M.E., 2012. Bench-scale study of active mine water treatment using cement kiln dust (CKD) as a neutralization agent. Water Res. 46, 327–334.

Matlock, M.M., Howerton, B.S., Atwood, D.A., 2001. Irreversible precipitation of mercury and lead. J. Hazard. Mater. 84, 73–82.

Matlock, M.M., Howerton, B.S., Atwood, D.A., 2003. Covalent coating of coal refuse to inhibit leaching. Adv. Environ. Res. 7, 495–501.

Mollamahmutoğlu, M., Yilmaz, Y., 2001. Potential use of fly ash and bentonite mixture as liner or cover at waste disposal areas. Environ. Geol. 40, 1316–1324.

Moncur, M.C., Ptacek, C.J., Lindsay, M.B.J., Blowes, D.W., Jambor, J.L., 2015. Long-term mineralogical and geochemical evolution of sulfide mine tailings under a shallow water cover. Appl. Geochem., Environmental Geochemistry of Modern Mining 57, 178–193.

Monterroso, C., Macías, F., 1998. Drainage waters affected by pyrite oxidation in a coal mine in Galicia (NW Spain): Composition and mineral stability. Sci. Total Environ. 216, 121–132.

Motsi, T., Rowson, N.A., Simmons, M.J.H., 2009. Adsorption of heavy metals from acid mine drainage by natural zeolite. Int. J. Miner. Process. 92, 42–48.

Nyavor, K., Egiebor, N.O., 1995. Control of pyrite oxidation by phosphate coating. Sci. Total Environ. 162, 225–237.

Nyavor, K., Egiebor, N.O., Fedorak, P.M., 1996. Suppression of microbial pyrite oxidation by fatty acid amine treatment. Sci. Total Environ. 182, 75–83.

Osterloh, F., Saak, W., Pohl, S., Kroeckel, M., Meier, C., Trautwein, A.X., 1998. Synthesis and Characterization of Neutral Hexanuclear Iron Sulfur Clusters Containing Stair-like [Fe6(μ3-S)4(μ2-SR)4] and Nest-like [Fe6(μ3-S)2(μ2-S)2(μ4-S)(μ2-SR)4] Core Structures. Inorg. Chem. 37, 3581–3587.

Ouyang, Y., Liu, Y., Zhu, R., Ge, F., Xu, T., Luo, Z., Liang, L., 2015. Pyrite oxidation inhibition by organosilane coatings for acid mine drainage control. Miner. Eng. 72, 57–64.

Pandey, S., Yacob, T.W., Silverstein, J., Rajaram, H., Minchow, K., Basta, J., 2011. Prevention of Acid Mine Drainage Through Complexation of Ferric Iron by Soluble Microbial Growth Products. AGU Fall Meet. Abstr. 43, H43J-1370.

Park, I., Tabelin, C.B., Jeon, S., Li, X., Seno, K., Ito, M., Hiroyoshi, N., 2019. A review of recent strategies for acid mine drainage prevention and mine tailings recycling. Chemosphere 219, 588–606.

Park, I., Tabelin, C.B., Magaribuchi, K., Seno, K., Ito, M., Hiroyoshi, N., 2018a. Suppression of the release of arsenic from arsenopyrite by carrier-microencapsulation using Ti-catechol complex. J. Hazard. Mater. 344, 322–332.

Park, I., Tabelin, C.B., Seno, K., Jeon, S., Ito, M., Hiroyoshi, N., 2018b. Simultaneous suppression of acid mine drainage formation and arsenic release by Carrier-microencapsulation using aluminum-catecholate complexes. Chemosphere 205, 414–425.

Peppas, A., Komnitsas, K., Halikia, I., 2000. Use of organic covers for acid mine drainage control. Miner. Eng. 13, 563–574.

Pond, A.P., White, S.A., Milczarek, M., Thompson, T.L., 2005. Accelerated weathering of biosolid-amended copper mine tailings. J. Environ. Qual. 34, 1293–1301.

Pridmore, D.F., Shuey, R.T., 1976. The electrical resistivity of galena, pyrite, and chalcopyrite. Am. Mineral. 61, 248–259.

Ribeta, I., Ptacek, C.J., Blowes, D.W., Jambor, J.L., 1995. The potential for metal release by reductive dissolution of weathered mine tailings. J. Contam. Hydrol. 17, 239–273.

Rimstidt, J.D., Vaughan, D.J., 2003. Pyrite oxidation: a state-of-the-art assessment of the reaction mechanism. Geochim. Cosmochim. Acta, Advances in Oxide and Sulfide Mineral Surface Chemistry 67, 873–880.

Romero, F.M., Prol-Ledesma, R.M., Canet, C., Alvares, L.N., Pérez-Vázquez, R., 2010. Acid drainage at the inactive Santa Lucia mine, western Cuba: Natural attenuation of arsenic, barium and lead, and geochemical behavior of rare earth elements. Appl. Geochem. 25, 716–727.

Sahoo, P.K., Tripathy, S., Equeenuddin, Sk.Md., Panigrahi, M.K., 2012. Geochemical characteristics of coal mine discharge vis-à-vis behavior of rare earth elements at Jaintia Hills coalfield, northeastern India. J. Geochem. Explor. 112, 235–243.

Sahoo, P.K., Kim, K., Equeenuddin, S.M., Powell, M.A., 2013. Current approaches for mitigating acid mine drainage. Rev. Environ. Contam. Toxicol. 226, 1–32.

Satur, J., Hiroyoshi, N., Tsunekawa, M., Ito, M., Okamoto, H., 2007. Carrier-microencapsulation for preventing pyrite oxidation. Int. J. Miner. Process. 83, 116–124.

Savage, K.S., Stefan, D., Lehner, S.W., 2008. Impurities and heterogeneity in pyrite: Influences on electrical properties and oxidation products. Appl. Geochem., Sulfide Oxidation - Sulfide Oxidation: Insights from Experimental, Theoretical, Stable Isotope, and Predictive Studies in the Field and Laboratory 23, 103–120.

Schweigert, N., Zehnder, A.J.B., Eggen, R.I.L., 2001. Chemical properties of catechols and their molecular modes of toxic action in cells, from microorganisms to mammals. Environ. Microbiol. 3, 81–91.

Shu, X., Zhang, Q., Zhang, X., Mo, D., Li, L., Liang, Y., 2017. Inhibitory effect of pyrite oxidation by a new passivator and straw. Chin. J. Environ. Eng. 11, 933–937.

Simón, M., Martín, F., Ortiz, I., García, I., Fernández, J., Fernández, E., Dorronsoro, C., Aguilar, J., 2001. Soil pollution by oxidation of tailings from toxic spill of a pyrite mine. Sci. Total Environ. 279, 63–74.

Skousen, J., Foreman, J., 2000. Water management techniques for acid mine drainage control. Green Lands 30, 44–53.

Suteerapataranon, S., Bouby, M., Geckeis, H., Fanghänel, T., Grudpan, K., 2006. Interaction of trace elements in acid mine drainage solution with humic acid. Water Res. 40, 2044–2054.

Tabelin, C.B., Basri, A.H.M., Igarashi, T., Yoneda, T., 2012a. Removal of arsenic, boron, and selenium from excavated rocks by consecutive washing. Water, Air, Soil Pollut. 223(7), 4153-4167.

Tabelin, C.B., Hashimoto, A., Igarashi, T., Yoneda, T., 2014a. Leaching of boron, arsenic and selenium from sedimentary rocks: I. Effects of contact time, mixing speed and liquid-to-solid ratio. Sci. Total Environ. 472, 620–629.

Tabelin, C.B., Hashimoto, A., Igarashi, T., Yoneda, T., 2014b. Leaching of boron, arsenic and selenium from sedimentary rocks: II. pH dependence, speciation and mechanisms of release. Sci. Total Environ. 473–474, 244–253.

Tabelin, C.B., Igarashi, T., 2009. Mechanisms of arsenic and lead release from hydrothermally altered rock. J. Hazard. Mater. 169, 980–990.

Tabelin, C.B., Igarashi, T., Tamoto, S., 2010. Factors affecting arsenic mobility from hydrothermally altered rock in impoundment-type in situ experiments. Miner. Eng., Special issue: Sustainability, Resource Conservation & Recycling 23, 238–248.

Tabelin, C.B., Igarashi, T., Takahashi, R., 2012b. Mobilization and speciation of arsenic from hydrothermally altered rock in laboratory column experiments under ambient conditions. Appl. Geochem. 27, 326–342.

Tabelin, C.B., Sasaki, R., Igarashi, T., Park, I., Tamoto, S., Arima, T., Ito, M., Hiroyoshi, N., 2017a. Simultaneous leaching of arsenite, arsenate, selenite and selenate, and their migration in tunnel-excavated sedimentary rocks: I. Column experiments under intermittent and unsaturated flow. Chemosphere 186, 558–569.

Tabelin, C.B., Sasaki, R., Igarashi, T., Park, I., Tamoto, S., Arima, T., Ito, M., Hiroyoshi, N., 2017b. Simultaneous leaching of arsenite, arsenate, selenite and selenate, and their migration in tunnel-excavated sedimentary rocks: II. Kinetic and reactive transport modeling. Chemosphere 188, 444–454.

Tabelin, C.B., Veerawattananun, S., Ito, M., Hiroyoshi, N., Igarashi, T., 2017c. Pyrite oxidation in the presence of hematite and alumina: I. Batch leaching experiments and kinetic modeling calculations. Sci. Total Environ. 580, 687–698.

Tabelin, C.B., Veerawattananun, S., Ito, M., Hiroyoshi, N., Igarashi, T., 2017d. Pyrite oxidation in the presence of hematite and alumina: II. Effects on the cathodic and anodic half-cell reactions. Sci. Total Environ. 581–582, 126–135.

Tatsuhara, T., Arima, T., Igarashi, T., Tabelin, C.B., 2012. Combined neutralization–adsorption system for the disposal of hydrothermally altered excavated rock producing acidic leachate with hazardous elements. Eng. Geol. 139–140, 76–84.

Todd, E.C., Sherman, D.M., Purton, J.A., 2003. Surface oxidation of pyrite under ambient atmospheric and aqueous (pH = 2 to 10) conditions: electronic structure and mineralogy from X-ray absorption spectroscopy. Geochim. Cosmochim. Acta, Advances in Oxide and Sulfide Mineral Surface Chemistry 67, 881–893.

Uhlig, I., Szargan, R., Nesbitt, H.W., Laajalehto, K., 2001. Surface states and reactivity of pyrite and marcasite. Appl. Surf. Sci. 179, 222–229.

Vandiviere, M.M., Evangelou, V.P., 1998. Comparative testing between conventional and microencapsulation approaches in controlling pyrite oxidation. J. Geochem. Explor. 64, 161–176.

Vigneault, B., Campbell, P.G.C., Tessier, A., De Vitre, R., 2001. Geochemical changes in sulfidic mine tailings stored under a shallow water cover. Water Res. 35, 1066–1076.

Wiersma, C.L., Rimstidt, J.D., 1984. Rates of reaction of pyrite and marcasite with ferric iron at pH 2. Geochim. Cosmochim. Acta 48, 85–92.

Yang, Y., Li, Y., Sun, Q., 2014. Archaeal and bacterial communities in acid mine drainage from metal-rich abandoned tailing ponds, Tongling, China. Trans. Nonferrous Met. Soc. China 24, 3332–3342.

You, G., Yu, C., Lu, Y., Dang, Z., 2013. Evaluation of the protective effect of polysiloxane coating on pyrite with electrochemical techniques. Electrochimica Acta 93, 65–71.

Yuniati, M.D., Hirajima, T., Miki, H., Sasaki, K., 2015a. Silicate covering layer on pyrite surface in the presence of silicon–catechol complex for acid mine drainage prevention. Mater. Trans. 56, 1733–1741.

Yuniati, M.D., Kitagawa, K., Hirajima, T., Miki, H., Okibe, N., Sasaki, K., 2015b. Suppression of pyrite oxidation in acid mine drainage by carrier microencapsulation using liquid product of hydrothermal treatment of low-rank coal, and electrochemical behavior of resultant encapsulating coatings. Hydrometallurgy 158, 83–93.

Zaman, K.M., Chusuei, C., Blue, L.Y., Atwood, D.A., 2007. Prevention of sulfide mineral leaching through covalent coating. Main Group Chem. 6, 169–184.

Zhang, X., Borda, M.J., Schoonen, M.A.A., Strongin, D.R., 2003a. Adsorption of phospholipids on pyrite and their effect on surface oxidation. Langmuir 19, 8787–8792.

Zhang, X., Borda, M.J., Schoonen, M.A., Strongin, D.R., 2003b. Pyrite oxidation inhibition by a cross-linked lipid coating. Geochem Trans. 4, 8.

Zhang, Y.L., Evangelou, V.P., 1998. Formation of ferric hydroxide-silica coatings on pyrite and its oxidation behavior1. Soil Sci. 163, 53.

Chapter 2 Comparison of thermodynamic and electrochemical properties of ferric-, aluminum- and titanium-catecholate complexes

2.1 Introduction

In this chapter, the thermodynamic and electrochemical properties of Fe^{3+}-, Al^{3+}- and Ti^{4+}-catecholate complexes and the effects of the coating formed from these complexes on half-cell reactions of pyrite oxidation were compared. Speciation diagrams of metal-catecholate complexes were created using hyperquad simulation and speciation software (Hyss, 2009) based on thermodynamic considerations and the reliability of the results was verified by ultraviolet–visible (UV–Vis) light spectrophotometry. Redox properties of metal-catecholate complexes were elucidated by linear sweep voltammetry (LSV) and frontier orbital theory using energy level of highest occupied molecular orbital (E_{HOMO}). The formation of coating from different complexes was compared by conducting chronoamperometry and electrochemical impedance spectroscopy (EIS) on Pt electrode. Redox properties of coatings formed by various metal-catecholate complexes were evaluated by cyclic voltammetry. The abilities of coating formed from different complexes on Pt electrode surface against oxygen attack were evaluated by cathodic polarization.

2.2 Methodology

2.2.1 Solution preparation

Catechol (1,2-dihydroxybenzene, $C_6H_4(OH)_2$) and metal ion source ($AlCl_3 \cdot 6H_2O$, $FeCl_3 \cdot 4H_2O$, $Ti(SO_4)_2$ solution ($Ti(SO_4)_2$ in H_2SO_4)) were mixed in deionized water (DI water, 18MΩ·cm, Milli-Q® Water Purification System, Merck Millipore, USA) to prepare the solutions containing cation-catecholate complex. The pH of solutions was adjusted by adding sodium hydroxide (NaOH) solution to pH 3, 7, and 10. For all electrochemical experiments, 0.1M sodium chloride (NaCl) was added as a supporting electrolyte. All the solutions were filtered with a syringe-dived membrane filter with a pore size of 0.2 μm (Sartorius AG, Germany) before used in experiments.

2.2.2 Thermodynamic calculation and UV-Vis spectrophotometry

Speciation diagrams of metal-catecholate complexes were created using reported thermodynamic constants listed in Table 2-1 in the software named as hyperquad speciation and simulation (Hyss, 2009, Protonic software, Leeds, UK). The concentration of metal ion and catechol set for calculation is 1 mM and 3 mM, respectively. To confirm the results of thermodynamic calculations, solutions initially containing 1 mM metal ion (Fe^{3+} or Al^{3+}) and 3 mM catechol were adjusted to pH 3, 7 or 10 prepared, filtered by 0.2 μm filter membrane filter, and measured using UV–Vis light spectrophotometer (V-630, Jasco Analytical Instruments, Japan). For the case of Ti^{4+}, due to the limitation of measuring range of spectrophotometer, same experiment was conducted using the solution initially containing 0.1 mM Ti^{4+} and 0.3 mM catechol.

2.2.3 Electrochemical study

A conventional three-electrode system was used in this study. Platinum (Pt) rod with a surface area of 7.06 mm^2 embedded in non-conductive resin was used as the working electrode. Ag/AgCl/3.3 M NaCl and a Pt wire were used as reference and counter electrode, respectively. Solution (volume: 12 ml) was poured into a reactor cell with a water-jacket, which was connected to a water recirculating bath to maintain the temperature at 25°C. Solutions were purged with N_2 for 30 mins prior to each measurement, unless indicated otherwise. Electrode potential mentioned in this paper is refer to the value against Ag/AgCl reference electrode.

2.2.3.1 Linear sweep voltammetry

Linear sweep voltammetry (LSV) was conducted to study the redox properties of metal-catecholate complexes. The complex solutions used in LSV were prepared by dissolving 1 mM metal ions and 3 mM catechol in 0.1 M NaCl solution and the pH of solution was adjusted to pH 3, 7 or 10. The measurement was started from the open circuit potential (OCP), and the applied potential was increased up to + 0.8 V at a sweep rate of 5 mV/s. During the measurement, the solution was unstirred.

2.2.3.2 Chronoamperometry and electrochemical impedance spectroscopy

For investigating the process of coating formation during anodic reaction, chronoamperometry combining with electrochemical impedance spectroscopy (EIS) was conducted. The complex solutions used here were prepared by dissolving 5 mM metal ions and 15 mM catechol in 0.1 M NaCl solution and the pH of solution was adjusted to pH 10. In order to maintain the continuous supply of reactant from solution to electrode surface, during measurements, agitation using a magnetic bar at 250 rpm was conducted. During measurement, agitation using magnetic bar at 250 rpm was conducted. Electrode potential at + 0.8 V was applied on the working electrode to induce the oxidative decomposition of complexes for 10 min and EIS (DC bias, 0 Vs OCP; AC amplitude, 5 mV; AC frequency, 20000 Hz to 0.1 Hz) was applied to detect the surface change after chronoamperometry. Chronoamperometry-EIS in the same condition described above were repeated for 5 more times.

2.2.3.3 Electrochemical properties of the coating

After coating was formed on Pt electrode surface via the process mentioned in section 2.2.3.2, the redox properties of coatings and the suppressive effect of coating on reduction of O_2 were compared using cyclic voltammetry (CV) and chronoamperometry, respectively. For investigating the redox properties, Pt electrode with various coating was immersed in the 0.1 M NaCl solution which was deoxygenated with N_2 for 30 min. The measurement was start from OCP and the sweep direction was towards more negative potentials first (i.e., cathodic direction) at a scan rate of 5 mV/s for 1 cycle.

For investigating the suppressive effect of coating on preventing oxygen reduction, the Pt electrode with coatings was used as working electrode and put in the 0.1 M NaCl solution, which was open to the air and agitated by a magnetic bar at 250 rpm during the measurement. A constant potential at - 0.2 V was applied on the working electrode and the current was recorded as a function of time.

2.2.4 Density functional theory (DFT) study

DFT calculations with hybrid functionals were performed to determine geometries, energies and highest occupied molecular orbital (HOMO) energy levels (E_{HOMO}) of metal-catecholate molecules by using Gaussian 09 program (rev. D01). The functional CAM-B3LYP with 6-311+G** basis set was employed in all calculations. It was reported that the long-range corrected functional can reproduce the orbital energy well. The water solvation effect is included by a polarizable continuum model (Li et al., 2019b).

2.3 Results and discussion

2.3.1 Speciation of catechol and metal-catecholate complexes with pH

The structures, chemical formulas and abbreviations of catechol and metal-catecholate complexes are shown in Fig. 2-1 while their speciation diagrams with pH were made according to the thermodynamic constants listed in Table 2-1 and the results were shown in Fig. 2-2.

Table 2-1 List of thermodynamic constants (equilibrium constants for the formation of different chemical species, *β*) used in the calculation

Complex/compound	log β	Reference
$[Fe(cat)]^+$	20.01	Avdeef et al., 1978
$[Fe(cat)_2]^-$	34.7	
$[Fe(cat)_3]^{3-}$	43.76	
$[Al(cat)]^+$	16.3	Nurchi et al., 2009
$[Al(cat)_2]^-$	31.66	
$[Al(cat)_3]^{3-}$	41.06	
$[Ti(cat)_3]^{2-}$	60	Creutz and Chou, 2008
Hcat	13.0	Avdeef et al., 1978
H_2cat	22.22	
Fe(OH)	-2.6	Hutcheson et al., 2005
$Fe(OH)_2$	-5.34	
$Fe(OH)_3$	-11.51	
$Fe(OH)_4$	-20.88	
$Fe_2(OH)_3$	-2.84	
$Fe_4(OH)_3$	-5.38	
$Fe(OH)_{3(s)}$	37.4	
$Al_2(OH)_2$	-7.7	Crisponi et al., 2008

$Al(OH)$	-5.41
$Al(OH)_3$	-15.18
$Al(OH)_4$	-24.37

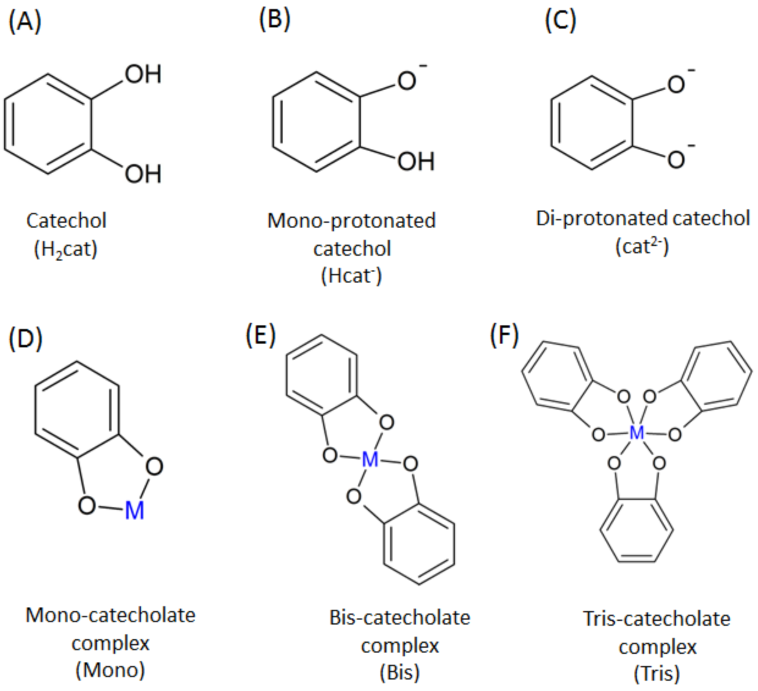

Catechol (H_2cat)

Mono-protonated catechol ($Hcat^-$)

Di-protonated catechol (cat^{2-})

Mono-catecholate complex (Mono)

Bis-catecholate complex (Bis)

Tris-catecholate complex (Tris)

Fig. 2-1 Structures, chemical formulas and abbreviations of catechol and metal-catecholate complexes

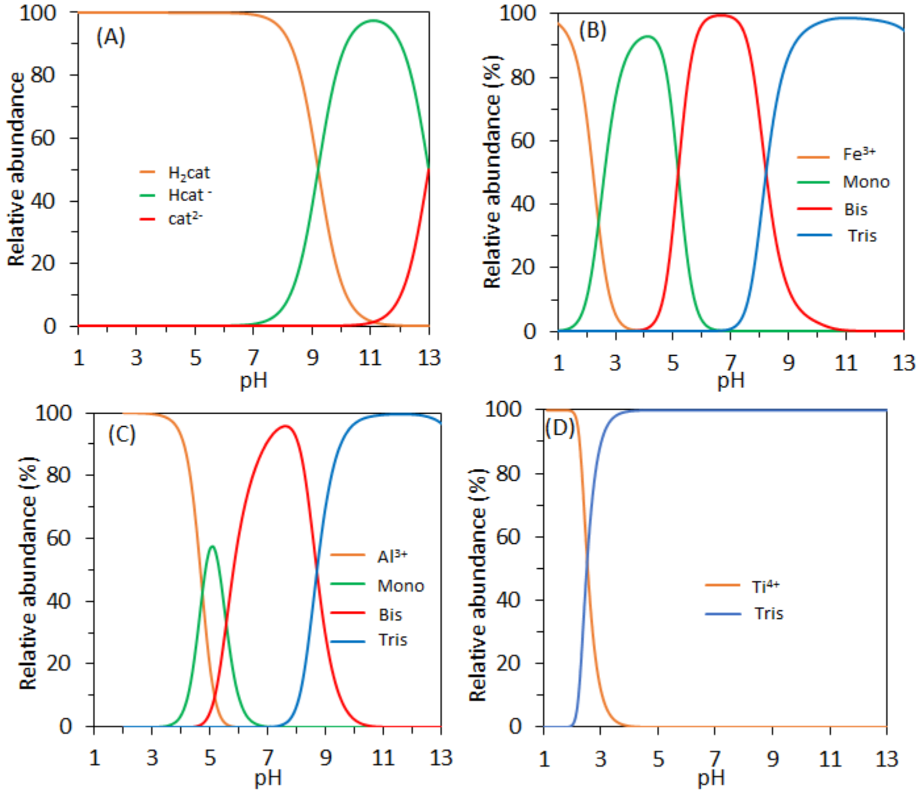

Fig. 2-2 Speciation diagrams of (A) catechol, (B) Fe^{3+}-catecholate complexes, (C) Al^{3+}-catecholate complexes and (D) Ti^{4+}-catecholate complex

Catechol is an organic molecule with the chemical formula $C_6H_6O_2$ (Fig. 2-1(A)). As shown in Fig. 2-2(A), catechol is not ionized below pH 7 but when the pH increases from 7 to 11, this compound is deprotonated forming mono-protonated catechol ($Hcat^-$, $C_6H_5O_2$, Fig. 2-1 (B)). Above pH 11, $Hcat^-$ loses one more proton to form di-protonated catechol (cat^{2-}, $C_6H_4O_2^{2-}$). Catechol is a strong complexing agent that forms water-soluble complexes with many metal ions (Sever and Wilker, 2004). It was reported that tri-valent cations (Fe^{3+} and Al^{3+}) coordinate with different number of catechol to form mono- (Fig. 2-1(C)), bis- (Fig. 2-1(D)), and tris-catecholate (Fig. 2-1(E)) complexes under different pH while for tetra-valent cations (Ti^{4+}), only tris -catecholate complexes was observed even with change of pH (Sever and Wilker, 2004). For Fe^{3+}-catecholate complexes shown in Fig. 2-2(B), mono- ($[Fe(cat)]^+$), bis- ($[Fe(cat)_2]^-$) and tris-catecholate ($[Fe(cat)_3]^{3-}$) presents in the range of pH 2-6, 4-10 and 7-13 respectively. For Al^{3+}-catecholate shown in Fig. 2-2(C), mono-

($[Al(cat)]^+$), bis- ($[Al(cat)_2]^-$) and tris-catecholate ($[Al(cat)_3]^{3-}$) presents in the range of pH 4-7, 5-10 and 8-13, respectively For Ti^{4+}-catecholate complex shown in Fig. 2-2(D), tris-catecholate complex ($[Ti(cat)_3]^{2-}$) starts to form when pH is above 2.

To verify the accuracy of the speciation diagrams created above to the conditions of this study, UV-Vis spectrophotometry was conducted on the solutions containing metal ion such as Fe^{3+}, Al^{3+} or Ti^{4+} and catechol at various pH (3, 7 and 10), and the results are shown in Fig. 2-3. For the solution containing catechol at pH 3 and 7, the absorbance spectra overlapped and gave the same peak at 274 nm, which was due to the presence of H_2cat. At pH 10, the absorbance peak shifted to around 297 nm, which could be attributed to the presence of $Hcat^-$. For the solution containing Fe^{3+} and catechol, the following additional absorbance peaks were detected: 416, 714 nm at pH 3; 379, 578 nm at pH 7; 496 nm at pH 10. The absorbance peaks observed at pH 3, 7 and 10 were close to the peaks reported for $[Fe(cat)]^+$, $[Fe(cat)_2]^-$ and $[Fe(cat)_3]^3$, respectively, indicating their presence in solution under the conditions of this study (Sever and Wilker, 2004). These results were consistent with the thermodynamic calculations shown in Fig. 2-2(B). In the case of Al^{3+} at pH 3, no absorbance peak corresponding to the presence of a complex was observed, which means that no complex was formed between Al^{3+} and catechol. At pH 7, an absorbance peak (i.e., shoulder) at around 295 nm was observed, which could be attributed to the presence of $[Al(cat)_2]^-$. At pH 10, an additional absorbance peak at 303 nm appeared and this may be due to the presence of $[Al(cat)_3]^{3-}$ (Park et al., 2018b). The results of UV-Vis spectra of solutions containing Al^{3+} and catechol were in line with the speciation diagrams. For the solution containing Ti^{4+} and catechol, absorbance peak at 374 nm corresponding to presence of $[Ti(cat)_3]^{2-}$ (Sever and Wilker, 2004)were observed at pH 7 and pH 10, but, this absorbance peak was absent at pH 3. It was different from the results of thermodynamic calculation in Fig. 2-2(D) showing $[Ti(cat)_3]^{2-}$ could be formed when pH was above 2. This difference may be due either to inaccuracies of the thermodynamic constants reported for Ti^{4+}-catecholate or that this value was determined under different conditions (temperature, ion strength, etc.) from our studies.

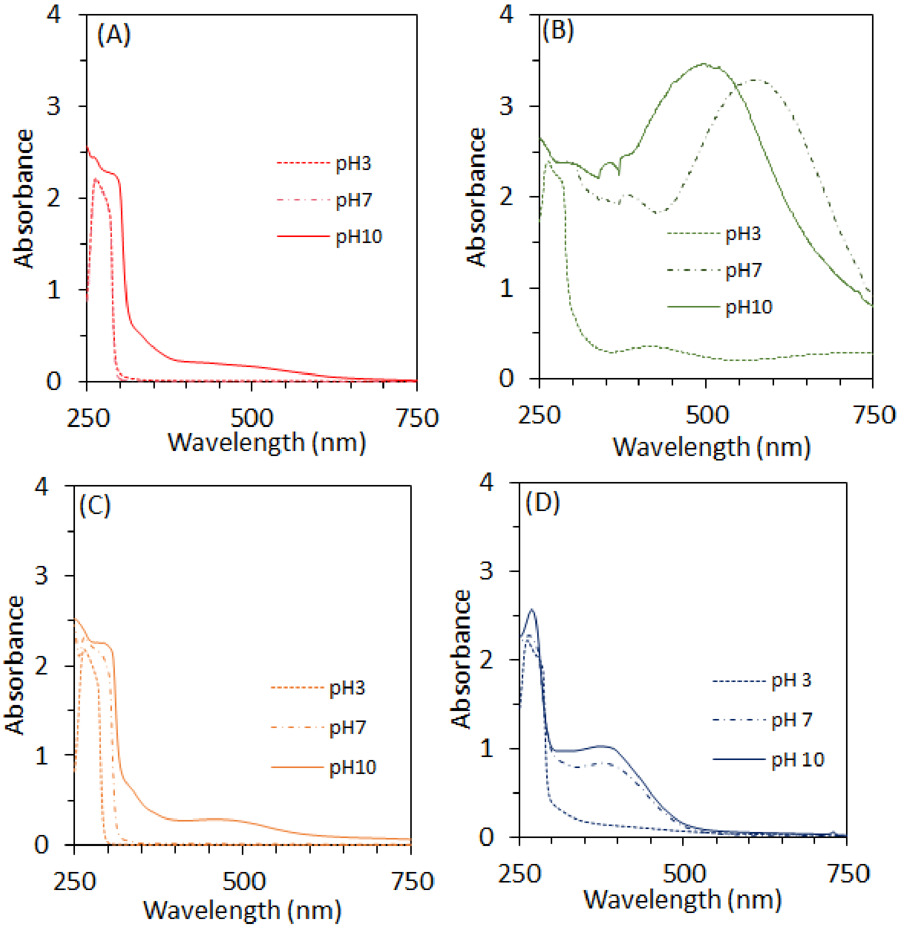

Fig 2-3 UV-Vis spectra of solutions containing (A) catechol, (B) Fe^{3+}-catecholate complexes, (C) Al^{3+}-catecholate complexes and (D) Ti^{4+}-catecholate complex

2.3.2 Redox properties of metal-catecholate complexes

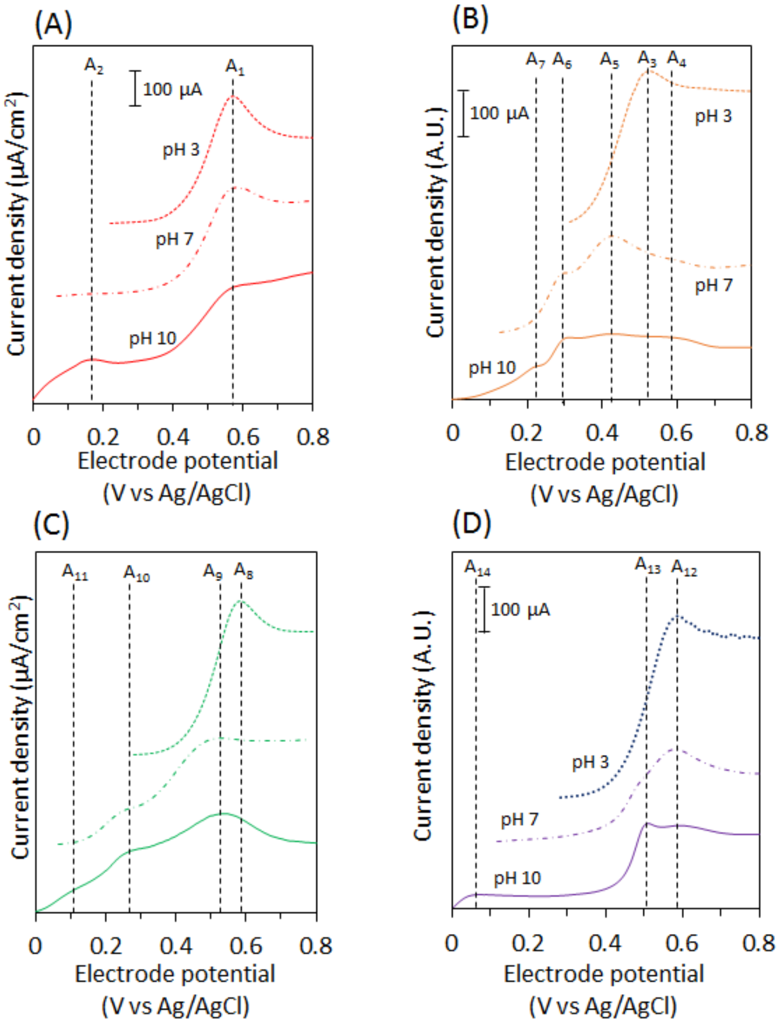

Fig. 2-4 Linear sweep voltammograms of solution containing (A) catechol, (B) Fe^{3+}-catecholate complexes, (C) Fe^{3+}-catecholate complexes and (D) Ti^{4+}-catecholate complex

During CME treatment, when metal-catecholate complexes approached at anodic sites of pyrite, they are expected to be oxidatively decomposed to release the metal ions that will form protective coatings (Eq. 2-1) (Li et al., 2019a, 2019b; Park et al., 2018a, 2018b).

$[M^{n+}(cat)_3]^{n-6} \rightarrow \quad M^{n+} + 3\ Q + 6\ e^-$ (M^{n+}: Fe^{3+}, Al^{3+} and Ti^{4+}; Q: quinone) (2-1)

This means that the electrode potential for oxidative decomposition of various metal-catecholate complexes are essential for the success of CME.

Fig. 2-4(A) shows the results of LSV for 0.1 M NaCl solutions containing 3 mM catechol at pH

3, 7 and 10. At pH 3 and 7, same current peak (A_1) was observed at + 0.57 V. In these conditions, both the results of speciation diagrams (Fig. 2-2(A)) and UV-Vis spectra (Fig. 2-3(A) showed the component in the solution is H_2cat, so A_1 could be attributed to Eq. 2-2.

$H_2cat \rightarrow Q + 2\ e^-$ (2-2)

In addition to the same peak A_1 at pH 10, another peak (A_2) at + 0.17 V was observed. This new peak may be caused by the oxidation of semi-quinone as shown in Eq. 2-3.

$SQ \rightarrow Q + e^-$ (2-3)

Fig. 2-4(B) shows the results of LSV for the solution containing Fe^{3+} and catechol. According to the results of thermodynamic calculation and UV-Vis spectrum, mono-catecholate complex was the dominant complex species formed in the solution at pH 3. Because the concentration ratio of Fe^{3+} and catechol is 1:3, even if the mono-catecholate complex was formed, the high concentration of free catechol should still present and give a current peak in the LSV. However, as shown in Fig. 2-4(A), the peak at + 0.57 V corresponding to the oxidation of free catechol was absent while a single peak appeared at + 0.53 V (A_4) was observed. So, this peak may be caused by the combinative current from oxidation of mono-catecholate complex (Eq. 2-4) and free catechol (Eq. 2-2).

$[Fe(cat)]^+ \rightarrow Fe^{3+} + Q + 2\ e^-$ (2-4)

At pH 7, the predominant species was confirmed to be bis-catecholate complex. A small peak around + 0.57 V (A_5) corresponding to the oxidation of free catechol, and two peaks around + 0.31 V (A_5) and + 0.42 V (A_6), which may be attributed to oxidation of bis- (Eq. 2-5) and mono-catecholate complexes (Eq. 2-4), respectively.

$[Fe(cat)_2]^- \rightarrow [Fe(cat)]^+ + Q + 2\ e^-$ (2-5)

If this is the case, there is no conflict about the inference on the current peak (A_4) observed at pH 3; that is, the current peak at + 0.53 V may be a combination of current peaks of oxidation of mono-catecholate at + 0.42 V and free catechol at + 0.57 V. At pH 10, the main complex species was confirmed to be tris-catecholate complex. In addition to the two current peaks at B_3 and B_4, a new peak around +0.22 V (A_7) appeared, which could be attributed to the oxidation of tris-catecholate complex to bis-catecholate complex (Eq. 2-6).

$[Fe(cat)_3]^{3-} \rightarrow [Fe(cat)_2]^{-} + Q + 2\ e^{-}$ (2-6)

Based on these results, the oxidative decomposition pathway of Fe^{3+}-catecholate complexes was also a sequential process:

$$[Fe(cat)_3]^{3-} \rightarrow [Fe(cat)_2]^{-} \rightarrow [Fe(cat)]^{+} \rightarrow Fe^{3+}$$

Fig. 2-4(C) illustrates the results of LSV for the solution containing Al^{3+} and catechol. At pH 3, a current peak was observed at + 0.57 V (A_8), which corresponds to oxidation of H_2cat (Eq. 2-2). At pH 7, a small current peak (A_8) corresponding to the oxidation of free catechol is observed around + 0.57 V. In addition to this peak, two more current peaks around + 0.28 V (A_3) and + 0.52 V (A_2) appeared. Based on the thermodynamic calculations shown in Fig. 2-2 (C), the present complex species should be bis-catecholate at pH 7. Considering this, the two current peaks was most likely due to the sequential oxidation of bis-catecholate complex, that is, peak A_9 and A_{10} were likely corresponding to the oxidation of bis-catecholate to mono-catecholate complex (Eq. 2-7) and oxidation of mono-catecholate complex to release Al^{3+} (Eq. 2-8), respectively.

$[Al(cat)_2]^{-} \rightarrow [Al(cat)]^{+} + Q + 2\ e^{-}$ (2-7)

$[Al(cat)]^{+} \rightarrow Al^{3+} + Q + 2\ e^{-}$ (2-8)

At pH 10, the predominant species is tris-catecholate complex. In addition to two current peaks at A_9 and A_{10}, a new current peak at A_{11} appeared. Since A_2 and A_3 were considered as the oxidation of bis-catecholate complex, the new peak was most likely due to the oxidation of tris-catecholate complex to bis-catecholate complex (Eq. 2-9).

$[Al(cat)_3]^{3-} \rightarrow [Al(cat)_2]^{-} + Q + 2\ e^{-}$ (2-9)

Based on these results, the oxidative decomposition of Al^{3+}-catecholate complex could be expressed as

$$[Al(cat)_3]^{3-} \rightarrow [Al(cat)_2]^{-} \rightarrow [Al(cat)]^{+} \rightarrow Al^{3+}$$

The results of LSV of solutions containing Ti^{4+} and catechol was shown in Fig. 2.4(D). At pH 3, a peak around + 0.57 V (A_{12}) corresponding to oxidation of free catechol (Eq. 2-2) was observed. This was consistent with the UV-Vis spectra shown in Fig. 2-3(D) indicating only free catechol was present in this condition at pH 3. At pH 7 and pH 10, in addition to A_{12}, a new current peak (shoulder) at + 0.51 V (A_{13}) appeared. Since the results of UV-Vis confirmed the presence of tris-catecholate complexes at pH 7 and 10, so this A_{13} should be related to oxidation of tris-catecholate complex. Different from three current peaks obtained in the case of $[Fe(cat)_3]^{3-}$ and $[Al(cat)_3]^{3-}$, this single peak may indicate that the oxidation of $[Ti(cat)_3]^{2-}$ may be not a sequential process: three coordinated catecholate in the complex were oxidized simultaneously at same potential as shown in Eq. 2-10.

$$[Ti(cat)_3]^{2-} \rightarrow Ti^{4+} + 3\,Q + 6\,e^- \qquad (2\text{-}10)$$

In addition, the current peak A_{14} observed at pH 10 may be assigned as the oxidation for semi-quinone (Eq. 2-3)

For CME, release of metal ions from complexes is a necessary process for coating formation. When metal-catecholate complex is completely oxidized, metal ions are released on pyrite surface and finally precipitated as a metal-oxyhydroxide phase on pyrite (Eq. 2-11).

$$M^{n+} + n\,OH^- \rightarrow M(OH)_n \qquad (2\text{-}11)$$

where M^{n+} represents for Fe^{3+}, Al^{3+} or Ti^{4+}.

The peak potential corresponding to the release of metal ions from Fe^{3+}-, Al^{3+}-, and Ti^{4+}-catecholate complexes appeared at around + 0.42 V, + 0.55 V, and + 0.51 V, respectively. These results indicate that Fe^{3+}-catecholate complexes are more readily oxidized while Al^{3+} and Ti^{4+}-catecholate complexes needed higher electrode potentials for complete decomposition.

2.3.3 Theoretical consideration for redox properties of metal-catecholate complexes

To better understand why these metal-complexes exhibit different oxidation potentials, E_{HOMO} of tris-catecholate complex of Fe^{3+}-, Al^{3+} and Ti^{4+} molecules was calculated by a DFT study. The results showed that E_{HOMO} of $[Ti(cat)_3]^{2-}$ is - 7.76 eV, which is much lower than $[Fe(cat)_3]^{3-}$ (- 7.25 eV) and $[Al(cat)_3]^{3-}$ (- 7.28 eV). It suggests that oxidation of $[Ti(cat)_3]^{2-}$ occurs at higher electrode potential than the other two complexes, which is consistent with the results obtained in LSV.

In contrast to the sequential decomposition behavior of Fe^{3+}- and Al^{3+}-catecholate complexes, the Ti^{4+}-catecholate complex is decomposed in a single step, which is difficult to interpret based on the experimental data. For better understanding the oxidative decomposition behavior of

Ti^{4+}-catecholate complex, E_{HOMO} of Ti^{4+}-catecholate complex and hypothetical intermediate produced by incomplete oxidative decomposition was calculated using a DFT study.

If decomposition of Ti^{4+}-catecholate complexes is also assumed as a sequential process as similar as Fe^{3+}- and Al^{3+}-catecholate complexes, the intermediates could be bis- or mono-catecholate complex. Without considering the coordination effect of H_2O or OH^-, bis- and mono-catecholate complex of Ti^{4+} could be represented as $[Ti(cat)_2]^0$ and $[Ti(cat)]^{2+}$. If the coordination effect of H_2O or OH^- was also included into consideration, the possible composition of bis- and mono-catecholate complexes could be represents as follows:

Bis-catecholate complex: $[Ti(cat)_2(H_2O)_2]^0$, $[Ti(cat)_2(H_2O)(OH)]^-$, $[Ti(cat)_2(OH)_2]^{2-}$

Mono-catecholate complex: $[Ti(cat)(H_2O)_4]^{2+}$, $[Ti(cat)(H_2O)_3(OH)]^-$, $[Ti(cat)(H_2O)_2(OH)_2]^0$

$[Ti(cat)(H_2O)(OH)_3]^-$, $[Ti(cat)(OH)_4]^{2-}$

In order to understand whether H_2O or OH^- coordinated into the bis- or mono-catecholate complex, the formation energy of bis- (or mono-) catecholate complex with coordinated H_2O and/or OH^- was calculated according to the following equation and the results were listed in the Table 2-2.

$$E_{form} = E\{Ti(cat)_m(H_2O)_q(OH)_n\} - E\{Ti(cat)_m\} - q*E\{H_2O\} - n*E\{OH^-\} \tag{2-12}$$

Table 2-2 Formation energy (E_{form}) and HOMO energy (E_{HOMO}) of hypothetical bis- and mono-catecholate complexes of Ti^{4+}

m, q, n	m=3 q=0 n=0	m=2 q=0 n=0	m=2 q=2 n=0	m=2 q=1 n=1	m=2 q=0 n=2	m=1 q=0 n=0	m=1 q=4 n=0	m=1 q=3 n=1	m=1 q=2 n=2	m=1 q=1 n=3	m=1 q=0 n=4
E_{form} （ev）	-	0.00	-1.35	-3.17	-4.29	0.00	-3.48	-4.28	-8.35	-9.76	-10.69
E_{HOMO} (ev)	-7.76	-8.36	-8.21	-7.87	-7.55	-9.69	-8.46	-8.53	-8.24	-7.78	-7.52

As shown in the Table 2-2, for bis- and mono-catecholate complexes, with the coordination of

OH- in the structure of molecular, the E_{form} is lowest, suggesting $[Ti(cat)_2(OH)_2]^{2-}$ and $[Ti(cat)(OH)_4]^{2-}$ are the most stable species for bis- and mono-catecholate complexes in theory, respectively. Their E_{HOMO} were calculated to be around -7.5 eV, which is higher than $[Ti(cat)_3]^{2-}$. These results imply that once $[Ti(cat)_3]^{2-}$ is partially oxidatively decomposed to form intermediates like $[Ti(cat)_2(OH)_2]^{2-}$ and $[Ti(cat)(OH)_4]^{2-}$, these intermediates may be immediately oxidized because they needed lower oxidation potentials for decomposition than that of $[Ti(cat)_3]^{2-}$. If this is the case, a reasonable explanation for the presence of only one peak in LSV could be proposed; that is, one oxidation peak corresponds to the simultaneous oxidative decompositions of the three coordinated catechol in complex under similar electrode potential.

2.3.4 Coating formation

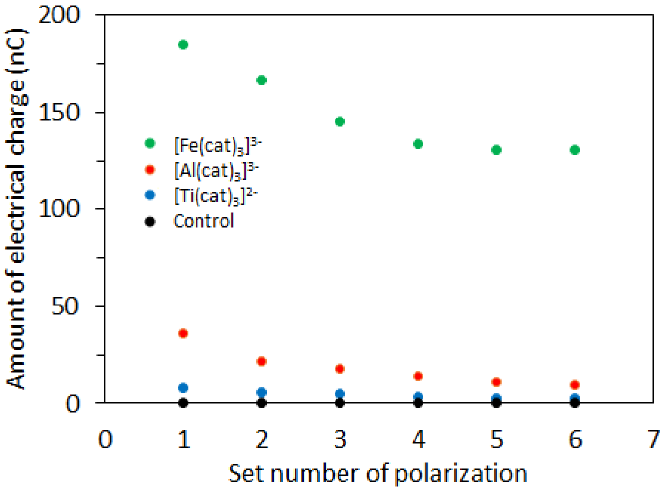

Fig. 2-5 Electrical charge generated in each set of 10-min polarization at + 0.8 V with or without metal-catecholate complexes

In this section, coating formation by various metal-catecholate complexes under same electrode potential were compared. Fig. 2-5 showed the relationship between amount of electrical charge (Q) generated from anodic polarization and set number of anodic polarizations at constant electrode potential (+ 0.8 V). For the case of solution without complexes, Q was almost 0. In the solutions of metal-catecholate complexes, Q were higher than 0 indicating the oxidative decomposition of metal-catecholate complexes occurred on Pt electrode surface. Among three complexes, Q generated from Fe^{3+}-catecholate complexes was apparently more than those generated from Al^{3+}-catecholate and Ti^{4+}-catecholate complexes. It meant that the decomposition rate of Fe^{3+}-catecholate complexes was faster than the other two complexes. For all the case with metal-catecholate complexes, with increase of set of anodic polarization, Q generated in each set reduced in the solution of metal-catecholate complexes, implying the decomposition rate of metal-catecholate complexes gradually decreased. The consumption of complex in each solution was calculated using the data of Q and the results showed that the change of concentration of complex due to the consumption during was negligible to the initial concentration. In addition, during experiment, the solution was continuously stirred with a magnetic bar, the supply of reductants to electrode surface could be achieved. If so, the decrease of reaction rate should not be attributed to the depletion of reactants near Pt electrode surface. Considering above, the decrease of Q with set of polarization may be attributed to the formation of passivated coating on Pt electrode.

$$[M^{n+}(cat)_3]^{n-6} + n\ OH^- \rightarrow M(OH)_n + 3\ Q + 6\ e^- \qquad (2\text{-}13)$$

Fig. 2-6 showed the EIS results of Pt electrode measured after each set of anodic polarization. For the case without complexes, EIS spectra generated in different set did not show any significant change, indicating the surface of Pt was not changed with anodic polarization. For the case of Fe^{3+}-catecholate complexes, a clear semi-circle combined with an inclined line could be observed. With increase of polarization time, the diameter of semi-circle also apparently increased. The semi-circle may be attributed to a resistor-capacitor parallel circuit in the coating and the inclined line was due to Warburg element. For the case of Al^{3+}- and Ti^{4+}-catecholate complexes, part of semi-circle like curve could be observed while the inclined lines were absent. Based on the discussion above, an equivalent circuit (A) could be applied to model the case for Fe^{3+}-catecholate complex and an equilibrant circuit (B) was applied for Al^{3+}/Ti^{4+}-catecholate complex. In these equilibrant circuit, R_s represents for solution resistance; R_d and Q_f represent for the resistance in the defect area of coating and the constant phase element corresponding to the capacitance of the coating, respectively; Ws represents for Warburg short corresponding to the diffusion with transmissive boundary.

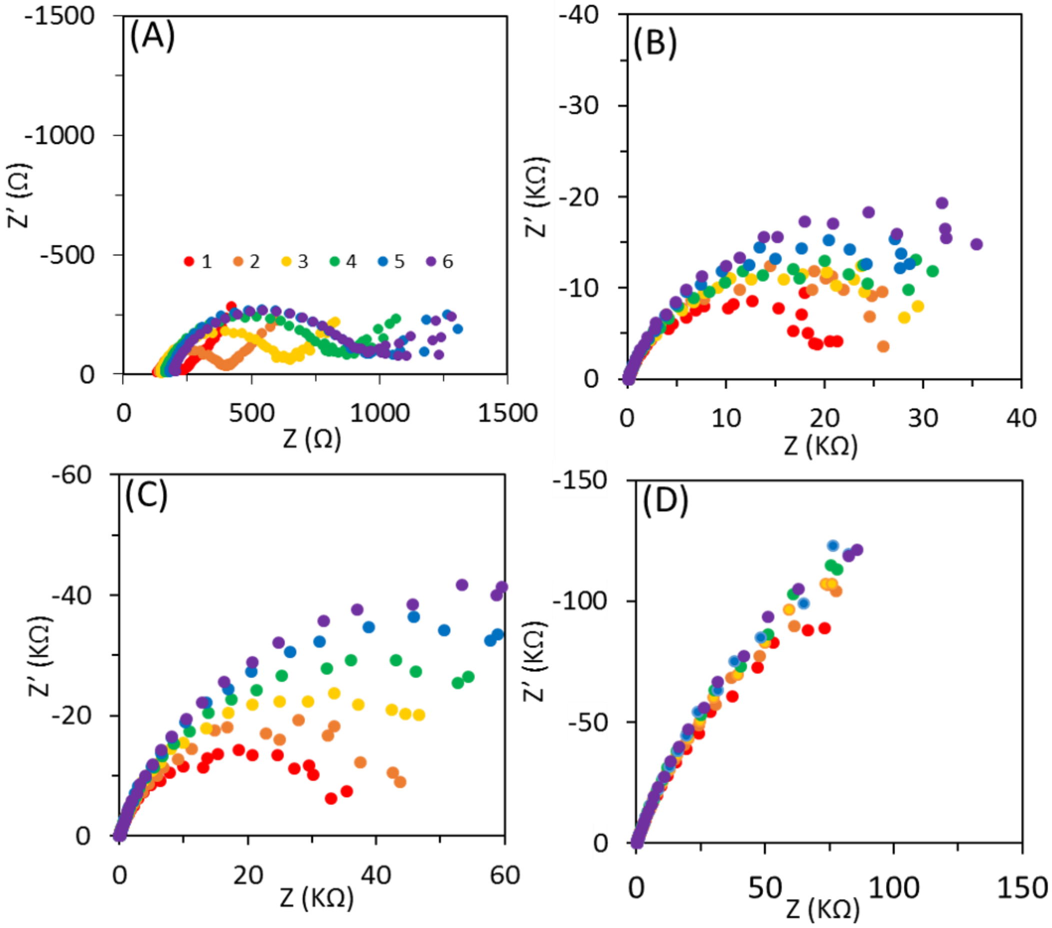

Fig. 2-6 Results of EIS after each set of 10-min polarization with (A) Fe^{3+}-catecholate complex, (B) Al^{3+}-catecholate complex, (C) Ti^{4+}-catecholate complex and (D) without metal-catecholate complex solutions

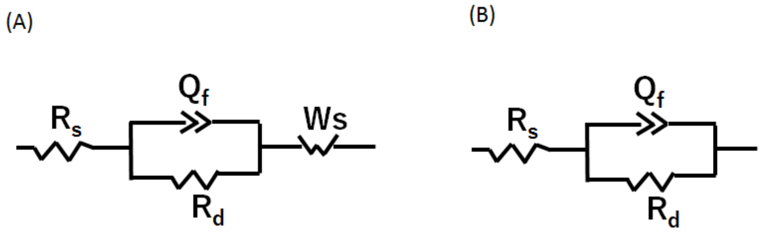

Fig. 2-7 Two equivalent circuit (A) and (B)

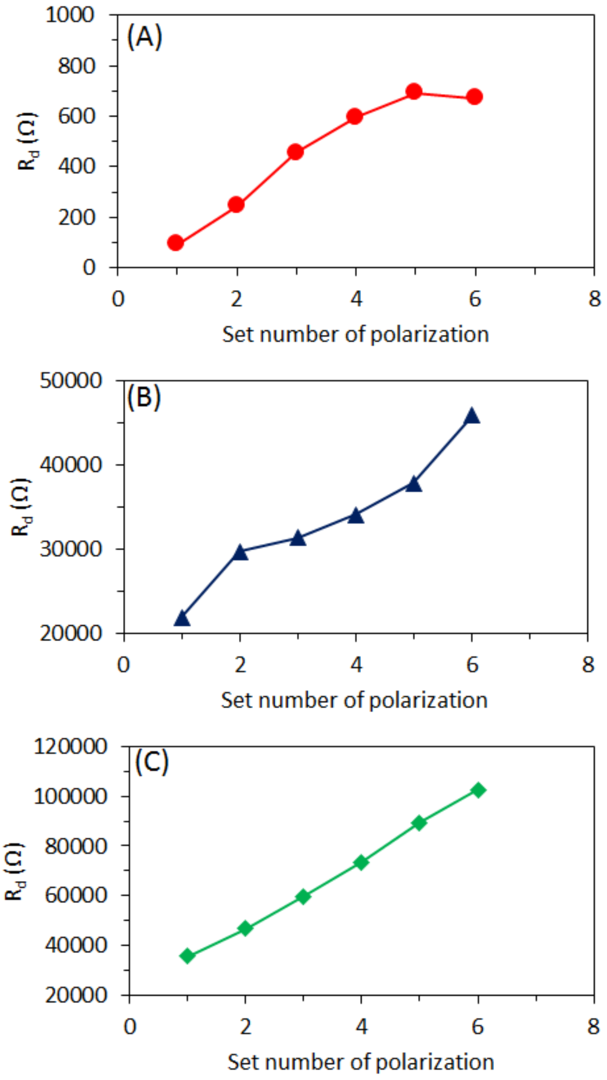

Fig. 2-8 Fitting results of R_d in the coating formed after each set of 10min-polarization in (A) Fe^{3+}-catecholate complex, (B) Al^{3+}-catecholate complex and (C) Ti^{4+}-catecholate complex solutions

As shown in Fig. 2-8, for all metal-catecholate complexes, with increase of anodic polarization time, the R_d of the coating increased indicating that the coating became more resistant. Compared to R_d of the coating formed by Ti^{4+}- and Al^{3+}-catecholate complexes, R_d in the one formed by Fe^{3+}-catecholate complex was apparently smaller. Electric charge, Q shown in Fig. 2-5 indicated that more coating may be produced in Fe^{3+}-catecholate complex solution. The reason that Fe-oxyhydroxide coating was less resistant than Al^{3+}- and Ti^{4+}-oxyhydroxide could be attributed to the electron exchange between Fe-oxyhydroxide coating and Pt electrode as shown in Eq. 2-14.

$Fe(OH)_3 + e^- \rightarrow \quad Fe(OH)_2$ (2-14)

For verifying this assumption, redox property of Fe-oxyhydroxide coating formed by Fe^{3+}-catecholate complex was investigated by cyclic voltammetry (CV). As results shown in Fig. 2-9, comparing with Al- and Ti-oxyhydroxide coating, a very big cathodic current peak around - 0.1 V was observed when Fe-oxyhydroxide was present on Pt electrode surface, indicating the reductive reaction of coating corresponding to Eq. 2-14 may occur. In addition, an anodic current peak around + 0.5 V was also observed, which may be due to the oxidation of $Fe(OH)_2$ to $Fe(OH)_3$ according to

$Fe(OH)_2 \rightarrow Fe(OH)_3 + e^-$ (2-15)

The discussion above illustrated that due to the electron exchange between $Fe(OH)_3$ coating and Pt electrode, the R_d in the coating $Fe(OH)_3$ was apparently smaller than the other two coatings. So, it may be difficult to compare the suppressive effect of various coatings based on EIS results. Considering this, suppressive effects of coating formed by various metal-catecholate complexes were compared by conducting chronoamperometry at cathodic electrode potential on the Pt electrode with coating.

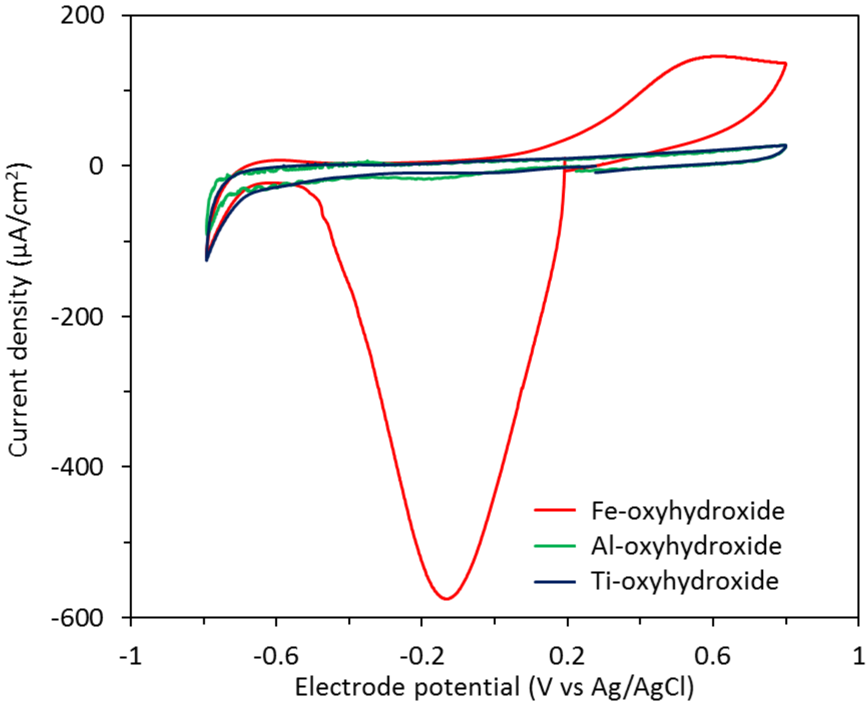

Fig. 2-9 Cyclic voltammograms of metal-oxyhydroxide coating on Pt electrode in 0.1 M NaCl solution

2.3.5 Effects of metal-oxyhydroxide coating on oxygen reduction on Pt electrode

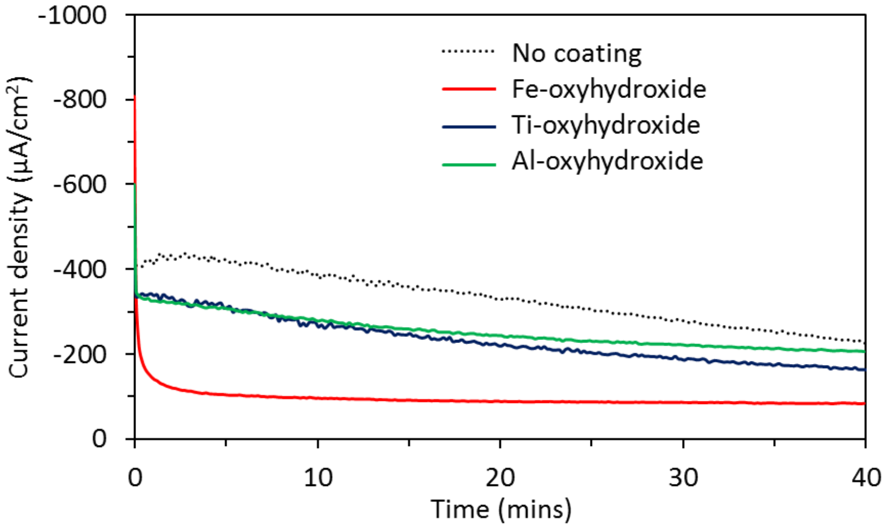

Fig. 2-10 Chronoamperometry at - 0.2 V of Pt electrode with or without metal-oxyhydroxide coating in 0.1 M NaCl at aerobic condition

Reduction of O_2 on cathodic site of pyrite is the first step of pyrite dissolution (Eq. 2-16), so the suppressive effect of coating formed in CME on oxygen reduction was very essential for us to compare the performance of the three kind of metal-catecholate complexes in CME (Li et al., 2019b).

$$O_2 + 4 e^- + 2 H_2O \rightarrow 4 OH^- + 6 e^- \tag{2-16}$$

Fig. 2-10 showed the current density generated on Pt electrode at - 0.2 V. The results showed that larger current generated on Pt electrode without pretreatment with metal-catecholate complex solution (no coating on Pt electrode), indicating that oxygen reacted rapidly on the electrode surface. After pretreatment with metal-catecholate complexes, the currents significantly became smaller. It means that coating formed from complexes suppressed O_2 reduction on Pt electrode. The smallest current was achieved with pretreatment with Fe^{3+}-catecholate complex, which suggested that Fe-oxyhydroxide coating gave the best suppressive effect on O_2 reduction. This may be because Fe^{3+}-catecholate complex could easily decomposed and more coating could be formed within a certain time than the other two complexes.

2.4 Conclusions

In this chapter, the thermodynamic and redox properties of ferric-catecholate complex was compared to aluminum- and titanium-catecholate complexes. Mono-, bis- and tris-catecholate complexes were formed in the solution containing ferric ions and catechol as same as aluminum-catechol system, while only tris-catecholate complexes was formed in solution containing titanium ions and catechol. The results of LSV indicated that ferric-catecholate complexes was decomposed sequentially: tris-catecholate complex was decomposed to bis-catecholate complex, and bis-catecholate complex was decomposed to mono-catecholate complex, then finally mono-catecholate complex decomposed to release ferric ions. The sequential decomposition also occurred for aluminum-catecholate complexes while decomposition of titanium-catecholate complex was one-step reaction: tris-catecholate complex was directly decomposed to release titanium ions. Among three complexes, ferric -catecholate was decomposed at lowest redox potential and decomposition rate was fastest. The coating formed with ferric-catecholate by polarization strongly suppressed the dissolved oxygen reduction on platinum electrode.

References

Avdeef, A., Sofen, S.R., Bregante, T.L., Raymond, K.N., 1978. Coordination chemistry of microbial iron transport compounds. 9. Stability constants for catechol models of enterobactin. J. Am. Chem. Soc. 100, 5362–5370.

Creutz, C., Chou, M.H., 2008. Binding of Catechols to Mononuclear Titanium (IV) and to 1- and 5-nm TiO_2 Nanoparticles. Inorg. Chem. 47, 3509–3514.

Crisponi, G., Nurchi, V.M., Pivetta, T., Gałezowska, J., Gumienna-Kontecka, E., Bailly, T., Burgada, R., Kozłowski, H., 2008. Towards a new attenuating compound: a potentiometric, spectrophotometric and NMR equilibrium study on Fe(III), Al(III) and a new tetradentate mixed bisphosphonate-hydroxypyridinonate ligand. J. Inorg. Biochem. 102, 1486–1494.

Hutcheson, R.M., Engelmann, M.D., Cheng, I.F., 2005. Voltammetric studies of Zn and Fe complexes of EDTA: Evidence for the push mechanism. Biometals 18, 43–51.

Sever, M., Wilker, J., 2004. Visible absorption spectra of metal–catecholate and metal–tironate complexes. Dalton Trans. 0, 1061–1072.

Li, X., Hiroyoshi, N., Tabelin, C.B., Naruwa, K., Harada, C., Ito, M., 2019a. Suppressive effects of ferric-catecholate complexes on pyrite oxidation. Chemosphere 214, 70–78.

Li, X., Gao, M., Hiroyoshi, N., Tabelin, C.B., Taketsugu, T., Ito, M., 2019b. Suppression of pyrite oxidation by ferric-catecholate complexes: An electrochemical study. Miner. Eng. 138, 226–237.

Nurchi, V.M., Pivetta, T., Lachowicz, J.I., Crisponi, G., 2009. Effect of substituents on complex stability aimed at designing new iron (III) and aluminum (III) chelators. J. Inorg. Biochem. 103, 227

Park, I., Tabelin, C.B., Magaribuchi, K., Seno, K., Ito, M., Hiroyoshi, N., 2018a. Suppression of the release of arsenic from arsenopyrite by carrier-microencapsulation using Ti-catechol complex. J. Hazard. Mater. 344, 322–332.

Park, I., Tabelin, C.B., Seno, K., Jeon, S., Ito, M., Hiroyoshi, N., 2018b. Simultaneous suppression of acid mine drainage formation and arsenic release by Carrier-microencapsulation using aluminum-catecholate complexes. Chemosphere 205, 414–425.

Tabelin, C.B., Veerawattananun, S., Ito, M., Hiroyoshi, N., Igarashi, T., 2017. Pyrite oxidation in the presence of hematite and alumina: II. Effects on the cathodic and anodic half-cell reactions. Sci. Total Environ. 581–582, 126–135.

Chapter 3 Suppression of pyrite oxidation by ferric-catecholate complexes: a leaching study

3.1 Introduction

This chapter aims to investigate the effects of Fe^{3+}-catecholate complexes on pyrite oxidation. A speciation diagram of Fe^{3+}-catecholate complexes was created using hyperquad simulation and speciation software (Hyss, 2009) based on thermodynamic considerations and the reliability of the results was verified by ultraviolet-visible (UV-Vis) light spectrophotometry. Linear sweep voltammetry (LSV) was conducted to elucidate the redox properties of Fe^{3+}-catecholate complexes. The composition and morphology of the pyrite surface treated with Fe^{3+}-catecholate complexes were characterized by high-resolution optical microscopy, scanning electron microscopy with energy dispersive X-ray spectroscopy (SEM-EDX) and attenuated total reflectance Fourier transform infrared spectroscopy (ATR-FTIR). Finally, the effects of Fe^{3+}-catecholate complexes on pyrite oxidation were investigated by batch-type leaching experiments.

3.2 Methodology

3.2.1 Pyrite sample preparation and characterization

A pyrite specimen obtained from Cerro de Pasco Mine, Peru was used in this study. For surface analysis of oxidation products, a single crystal cuboid sample (about 1 cm^3) cut from the specimen with a diamond cutter was used. This crystal sample was fixed inside a plastic holder using a non-conductive resin (Technovit 3040, Heraeus Kulzer GmbH, Germany) and polished with successively finer grades of silicon carbide papers (200 to 3000 grits) to remove the resin and expose a fresh pyrite surface.

For the leaching experiments, the pyrite sample was prepared as follows: (1) the pyrite specimen was lightly crushed by a hammer to ca. 2 cm in diameter to remove visible impurities manually. (2) the sample was crushed by a jaw crusher (BB51, Retsch Inc., Germany) to less than 2 mm, (3) the crushed pyrite sample was further ground by a disk mill (RS 100, Retsch Inc., Germany), and (4) the ground sample was sieved to obtain a 106 - 150 μm size fraction. To remove attached fine particles and any oxidized layer formed during preparation and storage, the sample was sonicated in ethanol for 30 s, washed with 1 M HNO_3 for 1min, rinsed with deionized water (DI water, 18 MΩ·cm, Milli-Q® Water Purification System, Merck Millipore, USA) for and dewatered with acetone (McKibben and Barnes, 1986).

The X-ray powder diffraction (XRD) pattern of the sample shows strong peaks of pyrite, and chemical composition of the sample determined by a wet method (i.e., microwave digestion and inductively coupled plasma atomic emission spectrometry, ICP-AES, ICPE 9820, Shimadzu Corporation, Japan) indicates that the sample was relatively pure with only about 3% of impurities like Si, Ca, Cu, and Zn.

3.2.2 Solutions

Solutions containing Fe^{3+} and catechol were prepared by dissolving reagent grade ferric nitrate nonahydrate ($Fe(NO_3)_3 \cdot 9H_2O$, Wako Pure Chemical Industries. Ltd., Japan) and catechol (1,2-dihydroxybenzene, $C_6H_6O_2$, Wako Pure Chemical Industries Ltd., Japan) in DI water, and their pH were adjusted using sodium hydroxide solution (NaOH, Wako Pure Chemical Industries Ltd., Japan). For the electrochemical experiments, sodium nitrate ($NaNO_3$, Wako Pure Chemical Industries. Ltd., Japan) was added as supporting electrolyte. In the leaching experiments, instead of NaOH, pH buffers (sodium acetate-acetic acid (NaAc-HAc), Wako Pure Chemical Industries Ltd., Japan), tris(hydroxymethyl) aminomethane (Tris, $C_4H_{11}NO_3$, SERVA, Germany) - nitric acid (HNO_3, Wako Pure Chemical Industries. Ltd., Japan) were used instead of NaOH solution to maintain a constant pH. Before the experiments, all solutions were filtrered through 0.2 μm syringe-driven membrane filters (Sartorius AG, Germany) to remove precipitates formed during solution preparation.

3.2.3 Speciation diagram of Fe^{3+}-catecholate complexes

A speciation diagram of Fe^{3+}-catecholate complexes from pH 1 to 13 was created using Hyss with the total concentrations of Fe^{3+} and catechol set at 0.1 mM and 0.3 mM, respectively. UV-Vis light spectrophotometry (V-630, Jasco Analytical Instruments, Japan) was used to identify Fe^{3+}-catechol complexes in solutions containing 0.1 mM Fe^{3+} and 0.3 mM catechol under various pH conditions. Before each measurement, the solution was poured into a single-crystal quartz cell and equilibrated to 25 °C for 30 mins. The UV-Vis absorption spectrum was measured between 800 and

350 nm.

3.2.4. Electrochemical experiments

Redox properties of Fe^{3+}-catecholate complexes were investigated by anodic and cathodic LSV using a computer-controlled electrochemical measurement unit (SI 1280B, Solartron Instruments, UK). A conventional three-electrode system was used consisting of a platinum (Pt) rod working electrode (surface area: 7.06 mm^2), a Pt wire counter electrode, Ag/AgCl/3.3M NaCl reference electrode and a glass cell with a water-jacket connected to a recirculating thermostat water bath (BB400, Yamato Scientific Co. Ltd., Japan).

12 ml of 0.1 M $NaNO_3$ solutions containing (i) 1 mM Fe^{3+} and 1mM catechol (pH 5), (ii) 1 mM Fe^{3+} and 2 mM catechol (pH 8), or (iii) 1 mM Fe^{3+} and 3 mM catechol (pH 10) was poured in the cell maintained at 25°C, and purged with N_2 (99.99 % purity) for 30 mins through a Teflon® tube to remove dissolved oxygen (DO). Before each measurement, the tube tip was repositioned slightly above the surface of the solution, and N_2 was continuously introduced to avoid redissolution of oxygen during the measurement. The LSV measurement was started after equilibration at open circuit potential (OCP) either towards positive (+ 0.8 V) or negative (- 0.2 V) potentials at a sweep rate of 5 mV/s.

3.2.5 Leaching experiments

Solutions used for the leaching experiments were prepared by dissolving pre-determined amounts of $Fe(NO_3)_3$ and catechol in pH-buffered solutions (0.1M NaAc-HAc (pH 5), 0.5 M Tris-HNO_3 (pH 8 and 10)). Leaching experiments were carried out by mixing 1 g of washed ground pyrite (106 – 150 μm) and 10 ml solution in 50-ml Erlenmeyer flask shaken at 80 strokes/min in a constant temperature water bath maintained at 25 °C. Several selected experiments were triplicated to ascertain that the differences observed were statistically significant. At predetermined time intervals, suspensions were collected and their pH and Eh were measured. The suspension was then filtered using a 0.2 μm membrane filter and the filtrate was analyzed for dissolved Fe and S concentrations using ICP-AES (margin of error = ± 2%) while the residue was thoroughly washed with DI water, dried in a vacuum drying oven at 40 °C for 24 h and observed by optical microscopy.

3.2.6 Characterization of oxidation products

A single crystal pyrite embedded in resin was immersed in the same solutions as those mentioned in section 3.2.5 under ambient conditions. After the pre-determined treatment time, the sample was taken out, washed thoroughly with DI water and dried in a vacuum drying oven at 40 °C for 24 h. The dried sample was then analyzed by high-resolution digital optical microscopy (VHX-100, Keyence Corporation, Japan) and analyzed by SEM-EDX (SSX-550, Shimadzu Corporation, Japan) and ATR-FTIR (FT/IR-6200HFV with an ATR Pro One attachment equipped with a diamond prism, Jasco Analytical Instruments, Japan).

3.3 **Results and discussion**

3.3.1 Speciation of Fe^{3+}-catecholate complexes

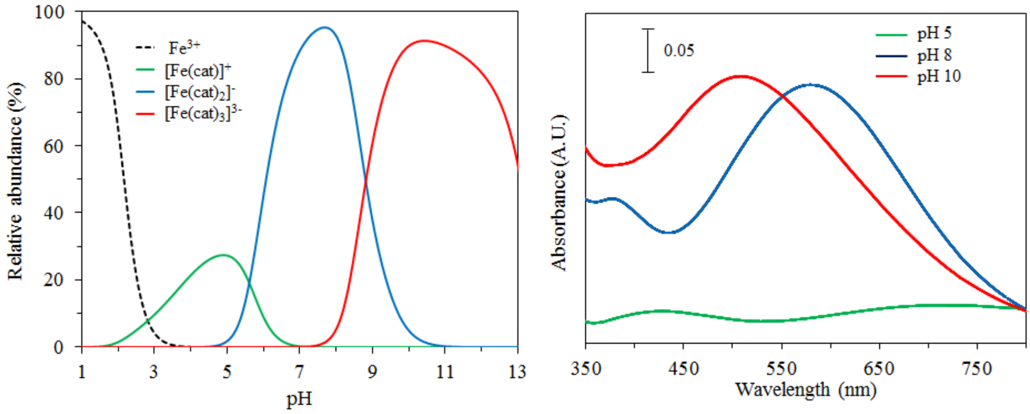

Fig. 3-1 (A) The speciation diagram with pH of Fe^{3+} and its catecholate species ($[Fe^{3+}]$ = 1 mM and [cat] = 0.3 mM) and (B) UV-Vis spectra of solutions containing 0.1 mM Fe^{3+} and 0.3 mM catechol under various pH conditions

Several authors have been reported that catechol coordinates with Fe^{3+} to form mono-, bis- or tris-catecholate complexes that speciate with pH and their reported structures (Avdeef et al., 1978; Hider et al., 1981, 1983; Schweigert et al., 2001; Sever and Wilker, 2004) are summarized as follows:

Mono-catecholate complex: $[Fe(cat)(H_2O)_4]^+$, $[Fe(Hcat)(H_2O)_4]^{2+}$, $Fe(cat)(OH)(H_2O)_3$

Bis-catecholate complex: $[Fe(cat)(Hcat)(OH)]^-$, $[Fe(cat)_2(OH)(H_2O)_2]^{2-}$, $[Fe_2(cat)_4(OH)(H_2O)]^{3-}$

Tris-catecholate complex: $[Fe(cat)_3]^{3-}$

Where “cat” and “Hcat” represent the di-deprotonated and mono-deprotonated catechol molecules, respectively. Sever and Wilker (2004) proposed that it is the di-deprotonated catechol and not the mono-deprotonated molecule that is coordinated with Fe^{3+}, and because direct observations of the Hcat ligand in mono- and bis-catecholate complexes in the aqueous phase have not yet been reported, catechol chelated with Fe^{3+} is assumed in this study to be di-deprotonated.

Because Fe^{3+} forms a six-coordinated complex while catechol is a bidentate-type ligand, either OH^- or H_2O may occupy the rest of the coordination sphere when this ion forms mono- or bis-catecholate complex. Unfortunately, the structures of mono- and bis-catecholate complexes are still under debate, so in this study, simplified notations were used; that is $[Fe(cat)]^+$ and $[Fe(cat)_2]^-$ represent mono- and bis-catecholate complexes, respectively while $[Fe(cat)_3]^{3-}$ is denoted as tris-catecholate complex.

A speciation distribution diagram of Fe^{3+}-catecholate complexes based on the thermodynamic constants (Avdeef et al., 1978; Hutcheson et al., 2005) is shown in Fig. 3-1(A). Both Fe^{3+}-catecholate complexes and ferric hydroxide were included in the calculations. The speciation diagram shows that Fe^{3+}-catecholate complex are not formed under strongly acidic conditions ($pH < 2$). The dominant Fe^{3+}-catecholate complexes changes with pH; that is, $[Fe(cat)]^+$, $[Fe(cat)_2]^-$, and $[Fe(cat)_3]^{3-}$ predominated at pH 5, pH 8 and pH 10, respectively.

Fig. 3-1(B) shows the UV-Vis spectra of solutions containing 0.1 mM Fe^{3+} and 0.3 mM catechol at various pH. At pH 5, two absorbance peaks appeared at 429 and 708 nm, which were very close to the reported peaks of $[Fe(cat)]^+$ (Sever and Wilker, 2004). At pH 8, two absorbance peaks at 376 nm and 579 nm were observed, which were similar to the peaks of $[Fe(cat)_2]^-$ (i.e. 374 nm and 576 nm) (Sever and Wilker, 2004). At pH 10, only one absorbance peak at 508 nm was visible, and this is near the peak of $[Fe(cat)_3]^{3-}$ (473 - 490 nm) (Sever and Wilker, 2004). These results were consistent with those predicted by the speciation diagram based on thermodynamic considerations.

3.3.2 Electrochemical properties of Fe^{3+}-catecholate complexes

In CME using Ti^{4+}- and Si^{4+}-catecholate complexes, the complexes are electrochemically decomposed on anodic sites of pyrite as follows (Jha et al., 2008, 2011; Park et al., 2018a, b; Satur et al., 2007; Yuniati et al., 2015), according to

$$[M(cat)_3]^{2-} \rightarrow M^{4+} + 3\ Q + 6\ e^- \quad (3\text{-}1)$$

where M and Q represent cations such as Ti^{4+} and Si^{4+}, and quinone ($C_6H_4O_2$), respectively.

The electrons released in Eq. 3-1 is transferred to cathodic sites of pyrite and consumed by the reduction of DO to water (H_2O) (Eq. 3-2).

$$3/2\ O_{2\,(aq)} + 6\ e^- + 6\ H^+ \rightarrow 3\ H_2O \quad (3\text{-}2)$$

The cations released in Eq. 3-1 are rapidly hydrolyzed and precipitated on the pyrite surface forming a protective barrier against further oxidation of pyrite (Eqs. 3-3 and 3-4)

$$M^{4+} + 2\ H_2O \rightarrow MO_2 + 4\ H^+ \quad (3\text{-}3)$$

$$M^{4+} + 4\ H_2O \rightarrow M(OH)_4 + 4\ H^+ \quad (3\text{-}4)$$

Similar to Ti^{4+} and Si^{4+}-catecholate complexes, Fe^{3+}-catecholate complexes may be oxidatively decomposed on the pyrite surface and suppress pyrite oxidation. Another possible effect is that, Fe^{3+}-catecholate complexes may act as oxidants and enhance pyrite oxidation due to the presence of Fe^{3+} as the central ion of the complexes. To evaluate the redox properties of Fe^{3+}-catecholate complexes, anodic and cathodic LSV were conducted in 0.1 M $NaNO_3$ solutions containing (i) 1 mM Fe^{3+} and 1 mM catechol (pH 5), (ii) 1 mM Fe^{3+} and 2 mM catechol (pH 8), or (iii) 1 mM Fe^{3+} and 3 mM catechol (pH 10). From the thermodynamic calculation and UV-Vis spectrophotometric measurements, it could be deduced that the dominant Fe^{3+}-catecholate complex was $[Fe(cat)]^+$ at pH 5, $[Fe(cat)_2]^-$ at pH 8 and $[Fe(cat)_3]^{3-}$ at pH 10. For comparison, the results for the solutions containing only catechol are also shown in the figures.

Figs. 3-2(A), (B) and (C) shows the results of anodic LSV. For $[Fe(cat)]^+$ solution at pH 5, the results showed that an apparent oxidative current peak is observed at + 0.43 V (Fig. 3-2(A)), which was lower than that of free catechol (Eq. 3-5).

$$H_2cat \rightarrow Q + 2\,e^- + 2\,H^+ \qquad E_{pa1} = +\,0.55\ V \tag{3-5}$$

The current peak at + 0.43V was most probably generated by the decomposition of $[Fe(cat)]^+$ to release Fe^{3+} and quinone (Eq. 3-6)

$$[Fe(cat)]^+ \rightarrow Fe^{3+} + Q + 2\,e^- \qquad E_{pa2} = +\,0.43\ V \tag{3-6}$$

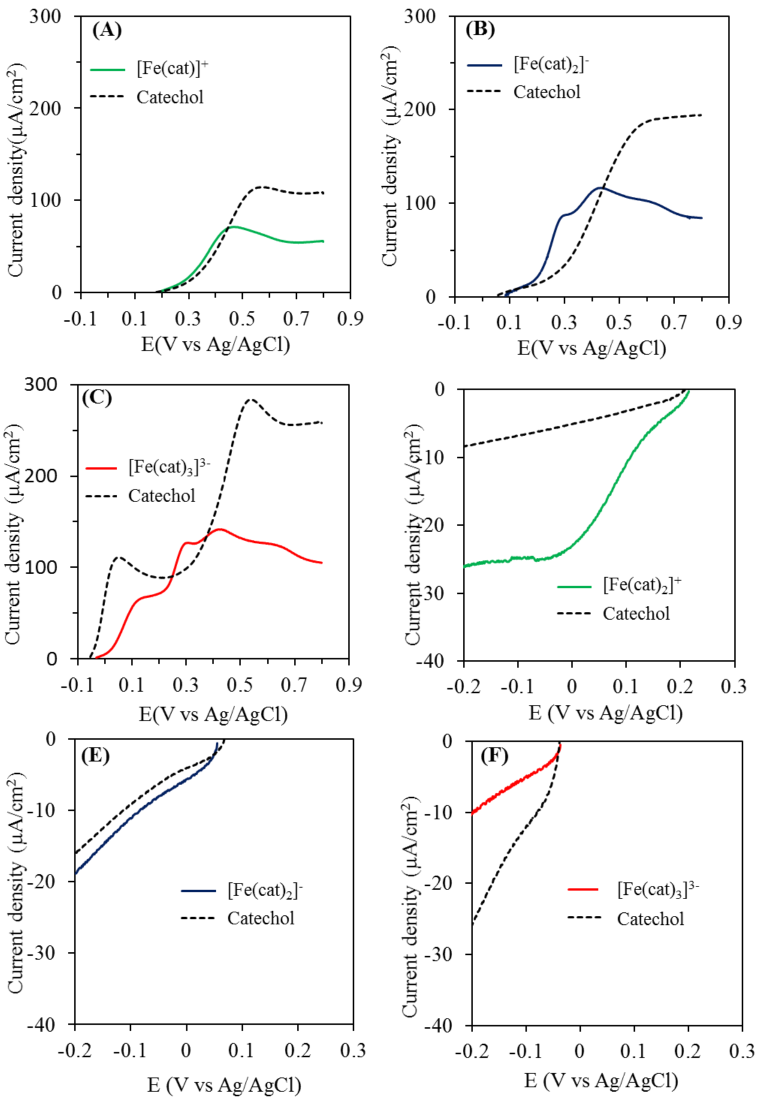

Fig. 3-2 Anodic linear sweep voltammograms of (A) mono-catecholate complexes, (B) bis-catecholate complexes and (C) tris-catecholate complexes and cathodic linear sweep voltammograms of (D) mono-catecholate complexes, (E) bis-catecholate complexes and (F) tris-catecholate complexes. The solution containing catechol only was measured under the same conditions.

For the solution of $[Fe(cat)_2]^-$ at pH 8 (Fig. 3-2(B)), two oxidation peaks were observed at + 0.29 and + 0.43V, and a weak-wide peak was detected between + 0.6 and + 0.7 V. By comparing with the result of LSV of free catechol, the wide peak between + 0.6 and + 0.7 V could be attributed to the oxidation of free catechol (Eq. 3-5). The peak at + 0.43 V also appeared in the case of $[Fe(cat)]^+$ solution at pH 5, which suggests that the same reaction as shown in Eq. 3-6 occurred. This means that $[Fe(cat)]^+$ was formed before this reaction, so the current peak that appeared at + 0.29 V is most likely because of the partial decomposition of $[Fe(cat)_2]^-$ to $[Fe(cat)]^+$ (Eq. 3-7).

$$[Fe(cat)_2]^- \rightarrow [Fe(cat)]^+ + Q + 2\ e^- \qquad E_{pa3} = +\ 0.29\ V \tag{3-7}$$

For $[Fe(cat)_3]^{3-}$ solution at pH 10 (Fig. 3-2(C)), anodic current peaks were observed around + 0.12, + 0.29, + 0.43 and + 0.6-0.7 V. The wide peak around + 0.6-0.7V could be attributed to the oxidation of free catechol (Eq. 3-5). By comparing the results shown in Fig. 3-2(C) with the results of Figs. 3-2(A) and (B), the peak at + 0.29 V and + 0.43 V could be attributed to be due to the oxidative decomposition of $[Fe(cat)_2]^-$ (Eq. 3-7) and $[Fe(cat)]^+$ (Eq. 3-6), respectively. This means that the peak at 0.12 V was because of the oxidative decomposition of $[Fe(cat)_3]^{3-}$ to $[Fe(cat)_2]^-$ (Eq. 3-8).

$$[Fe(cat)_3]^{3-} \rightarrow [Fe(cat)_2]^- + Q + 2\ e^- \qquad E_{pa4} = +\ 0.12\ V \tag{3-8}$$

In addition to the peak at around + 0.6-0.7 V, which was similar to the one observed in Figs. 3-2(A) and (B), Fig. 3-2(C) shows another peak at around + 0.06 V. This peak could be attributed to the oxidation of semi-quinone radicals, which are more stable under alkaline conditions due to the slow dismutation rate of radical anions (Schweigert, et al., 2004). Based on these results, Fe^{3+}-catecholate complexes follow a sequential oxidative pathway, which is summarized as follows:

$$[Fe(cat)_3]^{3-} \rightarrow [Fe(cat)_2]^- \rightarrow [Fe(cat)]^+ \rightarrow Fe^{3+}$$

Fig. 3-2(D), (E) and (F) showed the cathodic linear voltammograms of $[Fe(cat)]^+$, $[Fe(cat)_2]^-$ and $[Fe(cat)_3]^{3-}$, respectively. As shown in Fig. 3-2(A), a larger cathodic current was observed with $[Fe(cat)]^+$ than with catechol. This larger current could be attributed to the reduction of $[Fe^{III}(cat)]^+$ to $[Fe^{II}(cat)]$, which was also reported by the other researchers (Hider et al., 1981) according to

$[Fe^{III}(cat)]^+ + e^- \rightarrow [Fe^{II}(cat)]$ (3-9)

In Fig. 3-2(E), there was no significant difference between the current density obtained in $[Fe(cat)_2]^-$ and catechol only solutions, indicating that $[Fe(cat)_2]^-$ do not act as an oxidant to obtain electrons. As shown in Fig. 3-2(F), current density obtained for $[Fe(cat)_3]^{3-}$ was smaller than that of catechol. The larger current with catechol may be due to the reduction of semi-quinone formed under alkaline conditions. These results imply that among the three Fe^{3+}-catecholate complexes, only $[Fe(cat)]^+$ could act as an oxidant (electron-acceptor). This difference could be explained by the stronger steric effect of coordinated ligands in $[Fe(cat)_2]^-$ and $[Fe(cat)_3]^{3-}$ that made electron transfer from electrode to Fe^{3+} (electron acceptor) more difficult.

3.3.3 Surface observation of pyrite treated with Fe^{3+}-catecholate complexes

The results of electrochemical experiments showed under the right potential that Fe^{3+}-catecholate complexes could be oxidatively decomposed. If the oxidative decomposition of Fe^{3+}-catecholate complexes occurred on the anodic sites of pyrite, Fe^{3+} could be released and precipitated on the pyrite surface to form an iron oxyhydroxide coating. To verify the presence of this kind of coating, a single crystal pyrite sample was treated in solutions containing Fe^{3+}-catecholate complexes, and characterized using digital optical microscopy, SEM-EDX and ATR-FTIR. The solutions used for the treatment were (A) $[Fe(cat)]^+$ solution: 0.1 M NaA-HAc (pH 5) with 5 mM $Fe(NO_3)_3$ and 5 mM catechol, (B) $[Fe(cat)_2]^-$ solution: 0.5 M Tris-HNO_3 (pH 8) with 5 mM $Fe(NO_3)_3$ and 10 mM catechol, and (C) $[Fe(cat)_3]^{3-}$ solution: 0.5 M Tris-HNO_3 (pH 10) with 5 mM $Fe(NO_3)_3$ and 15 mM catechol.

Microscopic observations confirmed that pyrite was covered with a new solid phase after treatment in $[Fe(cat)]^+$ and in $[Fe(cat)_2]^-$ solutions for 1 day and 4 days, respectively. For pyrite sample treated in $[Fe(cat)_3]^{3-}$ solution up to 14 days, this new phase was not apparent. As shown in Fig. 3-3(B), SEM-EDX observations for pyrite treated with $[Fe(cat)_2]^-$ for 4 days showed that the coating formed on pyrite is composed of C, O and Fe.

Fig. 3-4 illustrates the results of ATR-FTIR spectroscopy. Absorption peaks corresponding to Fe-O band were detected at 490 cm^{-1} and 460 cm^{-1} (Basti et al., 2010; Tabelin et al., 2017) for pyrite treated in $[Fe(cat)]^+$ solution for 1 day. For pyrite treated in $[Fe(cat)_2]^-$ solution for 4 days, Fe-O peaks at 558, 499 and 449 cm^{-1}, a sharp peak at 1380 cm^{-1}, and O-H vibrations at 3057, 3260 and 3358 cm^{-1}, which correspond to the formation of iron-oxyhydroxide phaseswere detected (Tabelin et al., 2017). For pyrite treated with $[Fe(cat)_2]^-$, peaks and shoulders corresponding to C-C ring stretching (1515 cm^{-1}), C=C stretching (1450 cm^{-1}), C-O stretching (1271 cm^{-1}) and C-H bending (1210 cm^{-1}) vibrations were also observed (Basti et al., 2010). This indicates that organic substances such as catechol or its reaction products were present on the pyrite surface. The presence of organic substances in the coating could be attributed to either incomplete decomposition of Fe^{3+}-catecholate complexes or the adsorption of catechol/quinone on Fe-oxyhydroxides/oxides (Basti et al., 2010). Based on these results, an Fe-oxyhydroxides/oxide coating was formed after treatment with $[Fe(cat)]^+$ and $[Fe(cat)_2]^-$, but this coating was absent in $[Fe(cat)_3]^{3-}$.

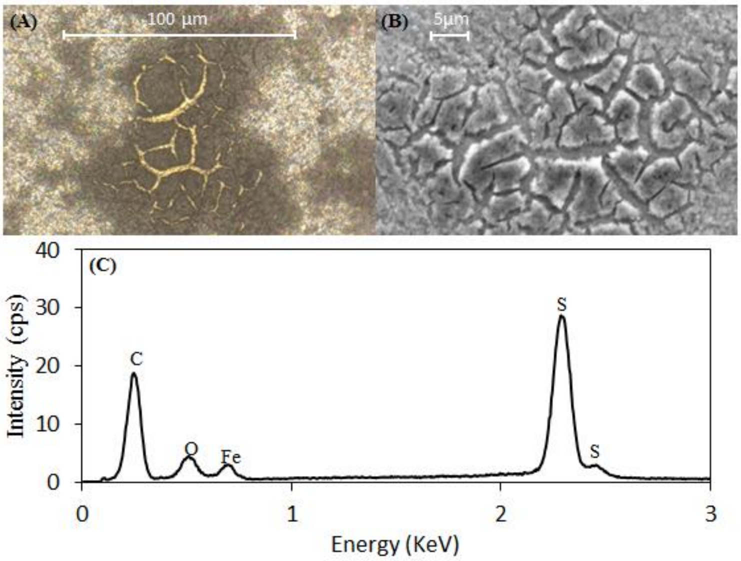

Fig. 3-3 Surface analysis of pyrite after treatment in $[Fe(cat)_2]^-$ for 4 days: (A) optical microscope photomicrograph, (B) SEM photomicrograph, and (C) EDX spectrum of observed area in (B)

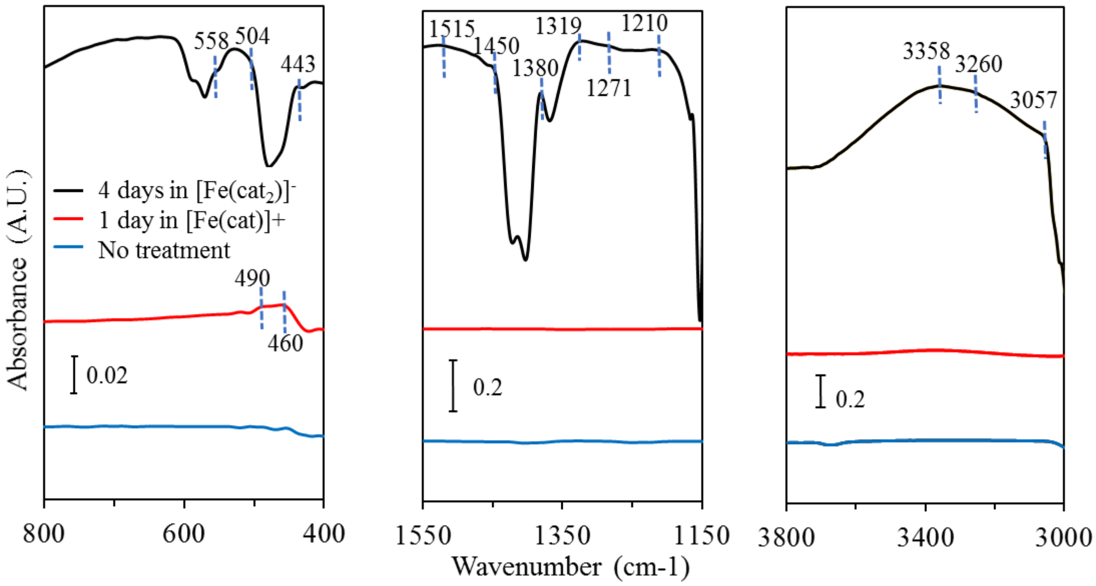

Fig. 3-4 ATR-FTIR spectra of pyrite before and after treatment with $[Fe(cat)]^+$ for 1 day and $[Fe(cat)_2]^-$ for 4 days. Note variations in the vertical scale

3.3.4 Leaching experiments

There are two possible effects of Fe^{3+}-catecholate complexes on the oxidation of pyrite: (1) suppression due to coating formation, and (2) enhancement via the oxidizing effect of Fe^{3+} in $[Fe(cat)]^+$. To evaluate the overall effects of three Fe^{3+}-catecholate complexes ($[Fe(cat)]^+$, $[Fe(cat)_2]^-$ and $[Fe(cat)_3]^{3-}$) on the pyrite oxidation, batch-type leaching experiment under different pH values with or without Fe^{3+}-catecholate complexes were conducted.

Fig. 3-5 shows the dissolved Fe concentration as a function of time. Without Fe^{3+}-catecholate complexes, Fe concentrations were relatively low because Fe^{2+} generated by pyrite oxidation was rapidly converted to Fe^{3+} and precipitated as $Fe(OH)_3$ (Eq. 3-10).

$$Fe^{3+} + 3H_2O \rightarrow Fe(OH)_3 + 3\,H^+ \qquad (3\text{-}10)$$

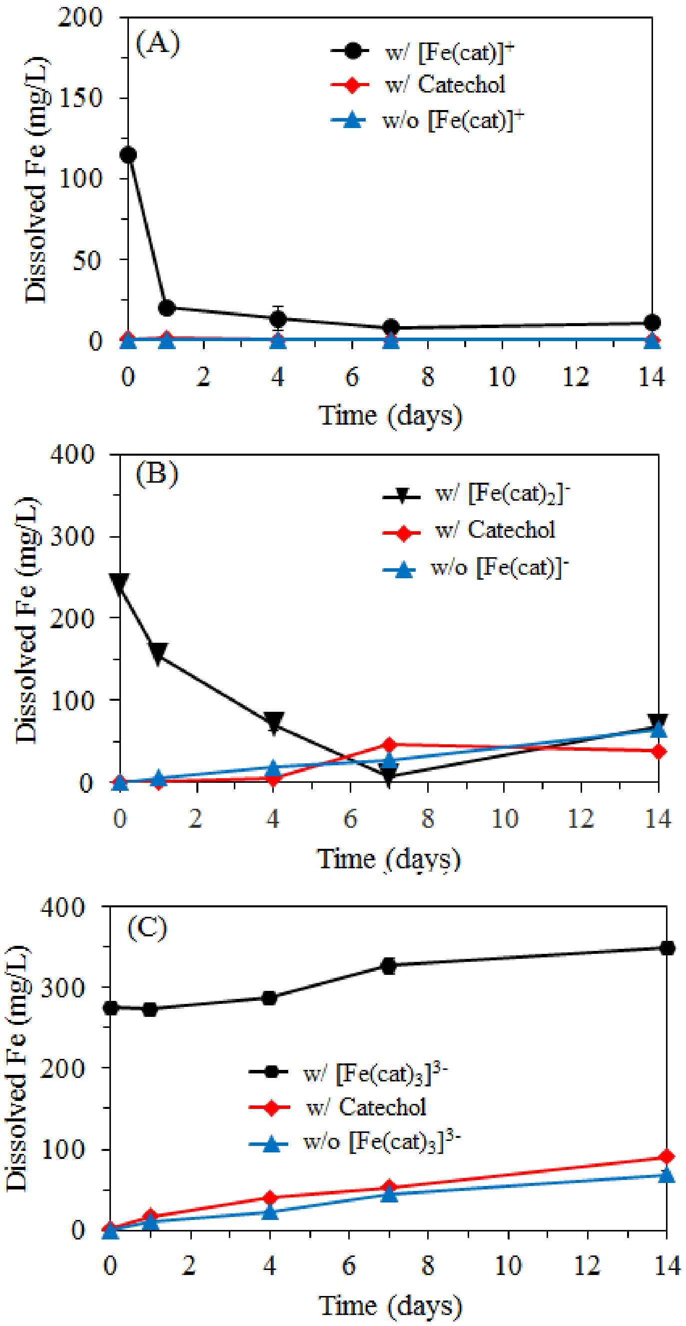

Fig. 3-5 Dissolved Fe concentration as a function of time: (A) mono-catecholate complexes at pH 5, (B) bis-catecholate complexes at pH 8, and (C) tris-catecholate complexes at pH 10. Control experiments with catechol only and without complexes were conducted for comparison

When Fe^{3+}-catecholate complexes were added, the initial Fe concentrations were higher than those without complexes. With $[Fe(cat)]^+$ and $[Fe(cat)_2]^-$, dissolved Fe concentrations decreased with time; that is, Fe concentration become less than 25 mg/L after 1 day for $[Fe(cat)]^+$ and 7 days for $[Fe(cat)_2]^-$. This could be attributed to the decomposition of $[Fe(cat)]^+$ and $[Fe(cat)_2]^-$ followed by precipitation of $Fe(OH)_3$ (Eqs. 3-10, 3-11 and 3-12).

$$[Fe(cat)_2]^- + 1/2\ O_2 + 2\ H^+ \rightarrow [Fe(cat)]^+ + Q + H_2O \tag{3-11}$$

$$[Fe(cat)]^+ + 1/2\ O_2 + 2\ H^+ \rightarrow Fe^{3+} + Q + H_2O \tag{3-12}$$

In comparison to $[Fe(cat)]^+$, precipitation of dissolved Fe was less extensive in $[Fe(cat)_2]^-$, which could be explained by its two-step decomposition reaction (Eqs. 3-11 and 3-12) of $[Fe(cat)_2]^-$. To form Fe-oxyhydroxides/oxides from $[Fe(cat)_3]^{3-}$, a three-step decomposition is required, which make the formation of these oxyhydroxides/oxides more difficult. Experimental results showed that with $[Fe(cat)_3]^{3-}$, dissolved Fe concentration did not decrease, indicating that $[Fe(cat)_3]^{3-}$ could not be decomposed completely within the duration of the leaching experiments (14 days).

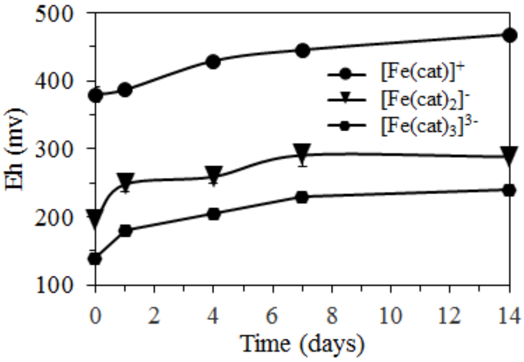

Fig. 3-6 Eh as a function of time in pyrite leaching experiments with mono-, bis-, and tris-catecholate complexes of Fe^{3+}

Fig. 3-6 illustrates the comparison of Eh of solutions during the leaching experiments. The values of Eh ranged from + 0.38 to + 0.47 V for $[Fe(cat)]^+$, + 0.2 to + 0.28 V for $[Fe(cat)_2]^-$, and + 0.13 to + 0.24 V for $[Fe(cat)_3]^{3-}$. These values indicate that redox conditions of the leaching system were more oxidizing with $[Fe(cat)]^+$ and $[Fe(cat)_2]^-$ than with $[Fe(cat)_3]^{3-}$. This may be another reason why the decompositions of $[Fe(cat)]^+$ and $[Fe(cat)_2]^-$ were easier than that of $[Fe\ (cat)_3]^{3-}$.

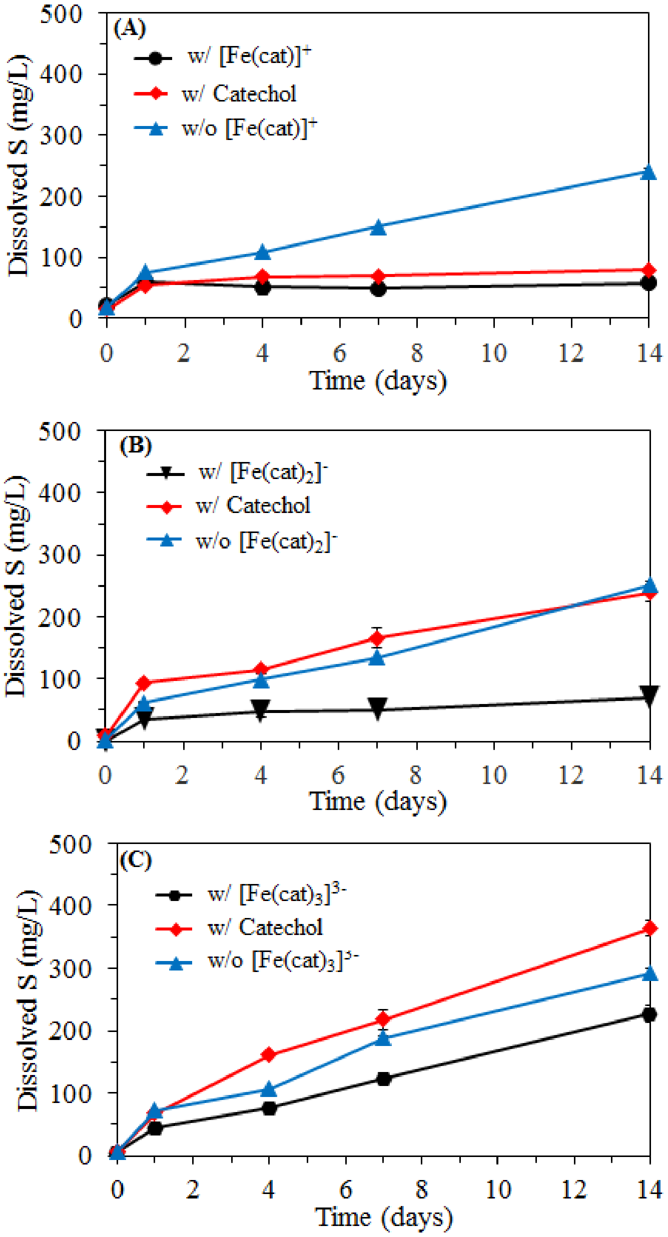

Fig. 3-7 Dissolved S concentration as a function of time: (A) mono-catecholate complex at pH 5, (B) bis-catecholate complex at pH 8, and (C) tris-catecholate complex at pH 10. Control experiments with only catechol only and without complexes were conducted for comparison

Fig. 3-7 shows the concentration of dissolved S as a function of time. Dissolved S concentration with Fe^{3+}-catecholate complexes was lower than that without complexes, indicating that Fe^{3+}-catecholate complexes suppressed pyrite oxidation. The extent of suppression varied with pH or Fe^{3+}-catecholate species; that is, dissolved S was almost constant after one day in $[Fe(cat)_2]^-$ (pH 8) and $[Fe(cat)]^+$ (pH 5), but continued to increase when $[Fe(cat)_3]^{3-}$ (pH 10). When $[Fe(cat)]^+$ and $[Fe(cat)_2]^-$ were used, Fe-oxyhydroxides/oxide coating was formed on pyrite which could explain why better suppression of pyrite oxidation in these two complexes was observed. In contrast, a coating was not formed in the case of $[Fe(cat)_3]^{3-}$, resulting in less effective suppression of pyrite oxidation. The weaker suppressive effects of $[Fe(cat)_3]^{3-}$ could be attributed mainly to its electron donating properties, whereby electrons are released during its partial decomposition to $[Fe(cat)_2]^-$ (Eq. 3-13) and the subsequent reactions (Eq. 3-11)

$$[Fe(cat)_3]^{3-} + 1/2\ O_2 + 2\ H^+ \rightarrow [Fe(cat)_2]^- + Q + H_2O \qquad (3\text{-}13)$$

In run-of-mine ore or tailings dam, Fe ions like Fe^{3+} and Fe-containing minerals coexist with pyrite, so the formation of Fe^{3+}-catecholate complexes when CME treatment is applied to these wastes is unavoidable. The results of leaching experiments showed Fe^{3+}-catecholate complexes suppress pyrite oxidation among a wide pH (5 - 10) where current CME treatments using Ti^{4+}, Si^{4+} and Al^{3+}-catecholate complexes have optimum suppressive effects. Our results indicate that Fe^{3+}-catecholate complexes formed during CME treatment have negligible effects on the efficiency of the technique. In fact, Fe^{3+}-catecholate complexes could improve the passivation of pyrite by forming a protective coating similar to those of Ti^{4+}-, Si^{4+}- and Al^{3+}-catecholate complexes. Unfortunately, CME using Fe^{3+}-catecholate complexes alone would be ineffective to suppress pyrite oxidation because after disposal of treated waste in tailings dam, Fe-oxyhydroxide/oxide could easily be re-dissolved when the conditions become acidic. None the less, hydrophilicity of iron oxyhydroxide may be useful in flotation, which is commonly conducted under alkaline conditions, so CME using Fe^{3+}-catecholate complexes may be applied to the feed before flotation as a kind of depressant to reduce pyrite floatability.

3.4 Conclusions

In this chapter, the effects of Fe^{3+}-catecholate complexes on pyrite oxidation were investigated. Mono-, bis- and tris-catecholate complexes were present under different pH conditions. All three complexes could act as an electron-donor while mono-catecholate also exhibited the ability to act as an electron acceptor. Mono- and bis-catecholate complexes of Fe^{3+} were oxidatively decomposed on the pyrite surface to form Fe-oxyhydroxide/oxide coating, resulting in the overall suppression of pyrite oxidation. Tris-catecholate complexes did not form a protective coating but could still limit the extent of pyrite oxidation due to its electron donating property.

This chapter is modified from “Li et al., 2019. Suppressive effects of ferric-catecholate complexes on pyrite oxidation. Chemosphere 214, 70-78”.

References

Avdeef, A., Sofen, S.R., Bregante, T.L., Raymond, K.N., 1978. Coordination chemistry of microbial iron transport compounds. 9. Stability constants for catechol models of enterobactin. J. Am. Chem. Soc. 100(17), 5362-5370.

Basti, H., Tahar, L.B., Smiri, L.S., Herbst, F., Vaulay, M. J., Chau, F., Ammar. S., Benderbous, S., 2010. Catechol derivatives-coated Fe_3O_4 and γ-Fe_2O_3 nanoparticles as potential MRI contrast agents. J. Colloid Interface Sci. 341(2), 248-254.

Hider, R.C., Mohd-Nor, A.R., Silver, J., Morrison, I.E., Rees, L.V., 1981. Model compounds for microbial iron-transport compounds. Part 1. Solution chemistry and Mössbauer study of iron (II) and iron (III) complexes from phenolic and catecholic systems. J. Chem. Soc. Dalton Trans. (2), 609-622.

Hider, R.C., Howlin, B., Miller, J.R., Mohd-Nor, A.R., Silver, J., 1983. Model compounds for microbial iron-transport compounds. Part IV. Further solution chemistry and Mössbauer studies on iron (II) and iron (III) catechol complexes. Inorg. Chim. Acta. 80, 51-56.

McKibben, M.A., Barnes, H.L., 1986. Oxidation of pyrite in low temperature acidic solutions: Rate laws and surface textures. Geochim. Cosmochim. Acta 50(7), 1509-1520.

Schweigert, N., Zehnder, A.J., Eggen, R.I., 2001. Chemical properties of catechols and their molecular modes of toxic action in cells, from microorganisms to mammals. Appl. Environ. Microbiol. 3(2), 81-91.

Sever, M.J., Wilker, J.J., 2004. Visible absorption spectra of metal–catecholate and metal–tironate complexes. Dalton Trans. (7), 1061-1072.

Tabelin, C.B., Veerawattananun, S., Ito, M., Hiroyoshi, N., Igarashi, T, 2017. Pyrite oxidation in the presence of hematite and alumina: I. Batch leaching experiments and kinetic modeling calculations. Sci. Total Environ. 580, 687-698.

Chapter 4 Suppression of pyrite oxidation by ferric-catecholate complexes: an electrochemical study

4.1 Introduction

In the previous chapter, Fe^{3+}-catecholate complexes was found to suppress the overall dynamics of pyrite oxidation via their electron donating effects and the formation of an Fe-oxyhydroxide-like coating on pyrite. However, the sequential decomposition of Fe^{3+}-catecholate complexes and the effects of Fe-oxyhydroxide-like coatings on the anodic and cathodic half-cell reactions of pyrite oxidation remain unclear. A more detailed understanding of these processes could not only improve the overall efficiency of CME but also provide important insights into the roles played by catechol-functional groups, ubiquitous in nature especially in natural organic matter, during the redox cycling of iron especially in systems rich in sulfide minerals like pyrite.

In this study, the mechanisms involved in the sequential decomposition of Fe^{3+}-catecholate complexes were investigated by linear sweep voltammetry (LSV) and frontier orbital theory using energy level of highest occupied molecular orbital (E_{HOMO}). Electrochemical processes crucial for the formation of coating and its intrinsic properties were also elucidated using chronoamperometry and electrochemical impedance spectroscopy (EIS). Finally, the effects of the coating on the half-cell reactions during pyrite oxidation were examined using chronoamperometry of CME-treated pyrite electrodes.

4.2 Methodology

4.2.1 Preparation of Fe^{3+}-catecholate complex solutions

All chemicals used in this paper were reagent grade (Wako Pure Chemical Industries. Ltd., Japan) and utilized without further purification. Ferric nitrate nonahydrate ($Fe(NO_3)_3{\cdot}9H_2O$), catechol (1,2-dihydroxybenzene, $C_6H_6O_2$), and deionized (DI) water (18 MΩ·cm, Milli-Q® Integral Water Purification System, Merck Millipore, USA) were used to prepare solutions containing Fe^{3+}-catecholate complexes while pH adjustments were done using sodium hydroxide (NaOH) solutions. All of the electrochemical experiments used sodium nitrate ($NaNO_3$) as supporting electrolyte. For the pretreatment of the pyrite electrode by Fe^{3+}-catecholate complex, a pH buffer (sodium acetate - acetic acid (NaAc-HAc)) was used to maintain the pH at 5.0 for 24 h. To remove precipitates formed during solution preparation, all solutions were filtered through 0.2 μm membrane filters using a vacuum filtration system (Sartorius AG, Germany).

4.2.2 Pyrite electrode preparation

A mineral specimen from Cerro de Pasco Mine, Peru was used to prepare the pyrite electrode. The pyrite specimen is mainly composed of Fe (45.8%) and S (51.2%) and only pyrite peaks were observed in its XRD pattern (Li et al., 2019). The single-crystal pyrite specimen was cut into a cuboid by a diamond cutter, connected to copper wires with silver conducting paste, and then embedded inside a plastic holder with Technovit® non-conductive resin (Heraeus Kulzer GmbH, Germany). Pyrite in the working electrode (i.e., pyrite electrode) was exposed by polishing with silicon carbide papers of increasing grit numbers (#200, #600, #1000, and #1500). Before each electrochemical experiment, the pyrite electrode was polished with silicon carbide paper (#1200, #1500, #2000, and #3000) and ultrasonically cleaned to expose a new and unreacted surface.

4.2.3 Electrochemical experiments

4.2.3.1 Static- and rotating disk-type electrode setups

The static-type electrode experiments were done with a conventional three electrode cell setup connected to a computer-controlled electrochemical measurement unit (SI 1280B, Solartron Analytical, UK) (Fig. 4-1(A)). Two kinds of working electrode were used in this type of electrochemical measurements: (1) a Pt working electrode with surface area of 0.196 cm^2 (HS-105, TOA DKK Co. Ltd., Japan), and (2) a pyrite working electrode as described in the last section. For the reference and counter electrodes, an Ag/AgCl/KCl-saturated electrode and a Pt plate were used, respectively. A jacketed glass reactor vessel was used for the measurement, which is connected to a recirculating thermostat water bath (BB400, Yamato Scientific Co. Ltd., Japan) maintaining the temperature at 298 K. For the rotating disk-type electrode experiment, a rotating Pt disk electrode with surface area of 0.196 cm^2 (HR-D1-Pt5, Hokuto Denko Co. Ltd. Japan) was used as the working electrode that is connected to a specially designed disk electrode driving unit (Fig. 4-1(B)). The reaction vessel for the rotating disk-type electrode experiments was placed in a thermo-stat water bath and maintained at 298 K. It should also be noted that only a Pt electrode was used for the rotating disk-type electrode measurements. The applied electrode potential in this paper is expressed as values against the Ag/AgCl/saturated KCl reference electrode.

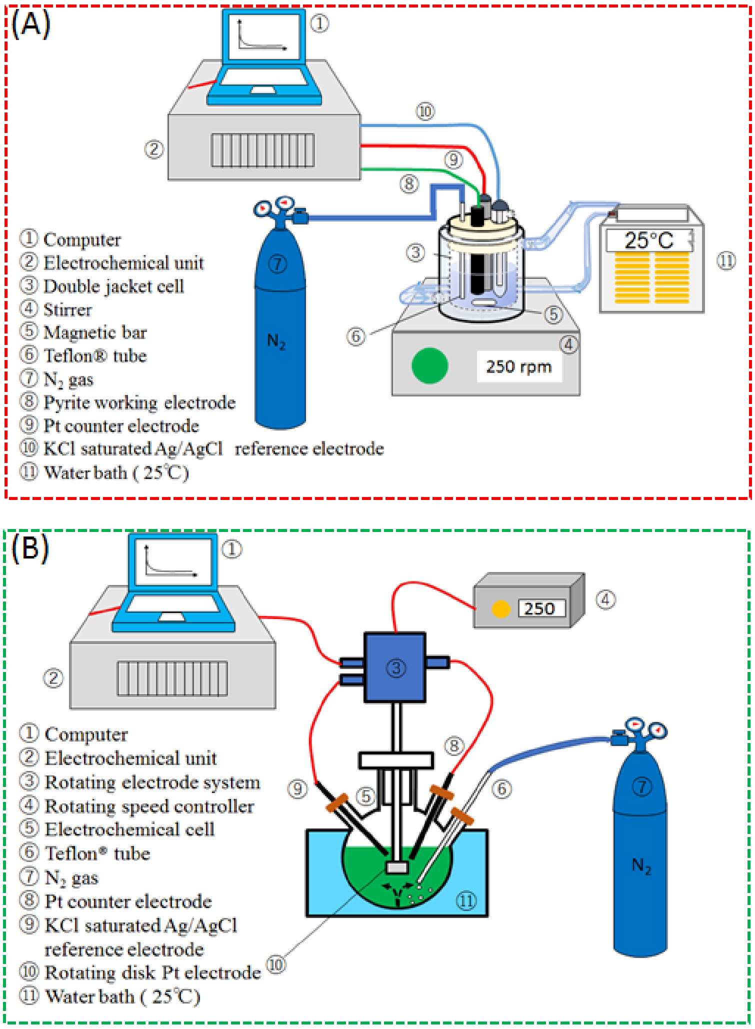

Fig. 4-1 Schematic diagrams of the electrochemical setup using (A) static-type electrode and (B) rotating disk-type electrode.

4.2.3.2 Linear sweep voltammetry

The LSV measurements were conducted using the static-type electrode setup, a Pt working electrode, and 120 ml of 0.1 M $NaNO_3$ solutions containing (i) 1 mM Fe^{3+} and 1mM catechol (pH 5),

(ii) 1 mM Fe^{3+} and 2 mM catechol (pH 8), or (iii) 1 mM Fe^{3+} and 3 mM catechol (pH 10). Before the experiments, DO was removed by with N_2 (99.999% purity) purging through a Teflon® tube inserted in the solution. After 30 mins, the tube tip was moved above the solution surface, and N_2 was continuously introduced to limit O_2 re-dissolution into solution during the measurement. For the LSV measurements, the working electrode was first equilibrated at the open circuit potential (OCP) and then an applied potential was introduced and increased incrementally at a sweep rate of 5 mV/s until + 0.8 V. The LSV measurements using a pyrite electrode were done in a similar manner as described above.

4.2.3.3 Chronoamperometry-EIS measurements using the rotating disk-type Pt electrode

To investigate the formation and growth of the protective coating via the anodic decomposition of Fe^{3+}-catecholate complexes, a series of chronoamperometry-EIS experiments were carried out using a rotating disk-type electrode setup and a Pt working electrode. The reactor vessel was filled with 300 ml of 0.1 M $NaNO_3$ solution containing 5 mM Fe^{3+} and 5 mM catechol (pH 5) and deoxygenated by N_2 gas purging for 40 mins prior to each measurement.

The first series of chronoamperometry-EIS experiments was designed to investigate the formation and growth of the protective coating with time. To decompose the Fe^{3+}-catecholate complex and form the protective coating, chronoamperometry was carried out at an applied potential of + 0.8 V for 1 min, which was then followed by EIS measurement (DC bias, + 0.8 V; AC amplitude, 5 mV; AC frequency, 20,000 Hz to 0.1 Hz) to elucidate the electrochemical properties (i.e., impedance) of the coating formed on the working electrode. At an applied potential of + 0.8V, chronoamperometry-EIS experiments were alternately repeated 10 times to investigate the growth of the protective coating. After the experiments, the Pt electrode was taken out of the reactor vessel, washed thoroughly with DI water, dried in a vacuum drying oven at 40 °C for 24 h, and then analyzed by scanning electron microscopy with energy dispersive X-ray spectroscopy (SEM-EDX). The results of EIS were fitted by equivalent circuit model using the ZView® software (Solartron Analytical, UK).

Another set of chronoamperometry-EIS experiments were carried out to investigate the effects of electrode potential on coating formation. Firstly, EIS was carried out at the OCP, and then a 10 mV DC bias against the OCP was applied to the working electrode while the anodic current was measured as a function of time until fluctuations in the current stabilized (i.e., the current was less than 5% of the total current for 1 min). After finishing the steady state current measurement mentioned above, another EIS measurement was conducted (DC bias, 0 mV Vs previous potential; AC amplitude, 5 mV; AC frequency, 20000 Hz to 0.1Hz). After this, chronoamperometry-EIS experiments were repeated alternately with a 10-mV step increase of the DC bias until the applied potential reached + 0.8 V.

4.2.3.4 Chronoamperometry of CME-treated pyrite electrodes

To form the coating, the pyrite electrode was pretreated for 24 h in a magnetically stirred (200 rpm) acetate buffer solution (40 ml; pH 5) containing 5 mM Fe^{3+} and 5 mM catechol at room temperature. After pretreatment, the electrode was taken out of the solution and washed thoroughly with DI water to remove any excess solution. Using the pretreated pyrite electrode as a working electrode, anodic and cathodic polarization experiments were conducted in a 120 ml 0.1 M $NaNO_3$ solution stirred with a magnetic bar at 250 rpm for 2h. Anodic polarization experiments were conducted at + 0.6 V under anoxic conditions while the cathodic polarization experiments were carried out at - 0.2 V under oxic conditions. As controls, anodic and cathodic polarization experiments of the pyrite electrode treated for 24 h in 40 ml acetate buffer solution (pH 5) without Fe^{3+}-catecholate complex were also carried out.

4.2.4 Density Functional Theory (DFT) calculations

Density Functional Theory (DFT) calculations with hybrid functionals were performed to determine geometries, energies, and highest occupied molecular orbital (HOMO) energy levels (E_{HOMO}) of mono-, bis-, and tris-catecholate complex molecules by using Gaussian 09 program (rev. D01) (Frisch, et al, 2009). The functional CAM-B3LYP (Yanai et al., 2004) with 6-311+G** basis set was employed in all calculations. It has been reported that the long-range corrected functional could reproduce the orbital energy accurately and with high degrees of certainty (Tsuneda and Hirao, 2014). The water solvation effect was included in the calculations using a polarizable continuum model (Cancès et al., 1997; Cossi et al., 1998; Mennucci and Tomasi, 1997).

4.3 Results and discussion

4.3.1 Oxidative decomposition of Fe^{3+}-catecholate complexes

The first step of coating formation in CME is the oxidative decomposition of metal-catecholate complexes on pyrite. Redox properties of Fe^{3+}-catecholate complexes were elucidated by LSV using solutions of (i) 1 mM Fe^{3+} and 1mM catechol (pH 5), (ii) 1 mM Fe^{3+} and 2 mM catechol (pH 8), or (iii) 1 mM Fe^{3+} and 3 mM catechol (pH 10). Fig. 4-2(A) shows the results of LSV using a Pt working electrode. Thermodynamic calculations and UV-Vis spectrophotometry results confirmed that the dominant Fe^{3+}-catecholate species in solutions (i), (ii), and (iii) were mono-, bis- and tris-catecholate complexes, respectively. Oxidative current peaks or shoulders were detected in the electrode potential regions of A_1, A_2, A_3, and A_4. LSV results for catechol solutions without Fe^{3+} only exhibited one peak at A_1 (data not shown), which suggest that the peak at A_1 corresponded to the oxidation of uncoordinated catechol according to

$$H_2cat \rightarrow Q + 2\ e^- + 2\ H^+ \qquad (4\text{-}1)$$

Meanwhile, peaks at A_2, A_3, and A_4 could be attributed to the oxidative decomposition of Fe^{3+}-catecholate complexes, which is consistent with our previous study proposing that Fe^{3+}-catecholate complexes decomposed via a sequential process (Li et al., 2019). At A_4, tris-catecholate complexes are oxidized to bis-catecholate complexes (Eq. 4-2) followed by the decomposition of bis-catecholate complexes to mono-catecholate at A_3 (Eq. 4-3) and finally, the oxidation of mono-catecholate complexes to release Fe^{3+} at A_2 (Eq. 4-4).

$$[Fe(cat)_3]^{3-} \rightarrow [Fe(cat)_2]^- + Q + 2\ e^- \qquad (4\text{-}2)$$

$$[Fe(cat)_2]^- \rightarrow [Fe(cat)]^+ + Q + 2\ e^- \qquad (4\text{-}3)$$

$$[Fe(cat)]^+ \rightarrow Fe^{3+} + Q + 2\ e^- \qquad (4\text{-}4)$$

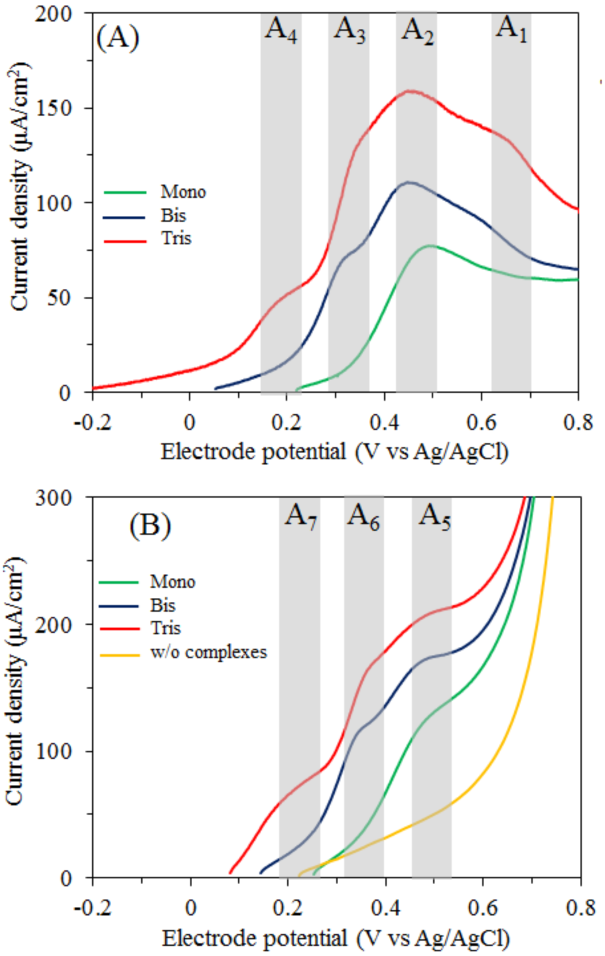

Fig. 4-2 Linear sweep voltammograms of Fe^{3+}-catecholate complexes on (A) Pt and (B) pyrite electrodes

However, Pt is an ideal surface, so whether these reactions would still occur on the pyrite surface under similar applied potentials remains unclear. To verify the oxidative decomposition of Fe^{3+}-catecholate complexes on pyrite, LSV using a pyrite working electrode and solutions (i), (ii), or (iii) were conducted (Fig. 4-2(B)). For comparison, LSV result in solutions without Fe^{3+}-catecholate complexes using the pyrite working electrode is also shown in Fig. 4-2(B). The oxidative decompositions of Fe^{3+}-catecholate complexes on pyrite were identical to those on Pt; that is, three oxidative current peaks, A_5, A_6 and A_7, were detected when Fe^{3+}-catecholate complexes were present in solution. Moreover, the applied potentials where the oxidative decomposition reactions occurred on pyrite were very similar to those observed (A_2, A_3 and A_4) for the Pt electrode (Fig. 4-2(A)), indicating that the decomposition pathway of Fe^{3+}-catecholate complexes on pyrite surfaces could be described in Eqs. 4-2, 4-3 and 4-4.

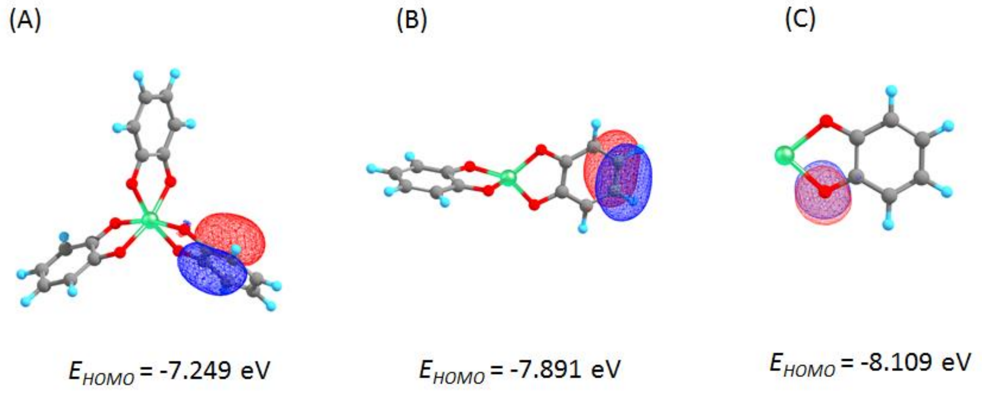

Fig. 4-3 HOMO and E_{HOMO} of (A) tris-catecholate, (B) bis-catecholate, and (C) mono-catecholate complexes. Atoms of Fe, H, C, and O are shown as green, light blue, gray, and red spheres, respectively. The orbital lobes shown in blue and red represent the opposite phases

To better understand why Fe^{3+}-catecholate complexes oxidatively decomposed sequentially, DFT calculations were performed. The spin multiplicities of Fe^{3+}-catecholate molecules, doublet, quartet, and sextet states were calculated, and the results verified that the sextet was the most stable spin multiplicity for Fe^{3+}-catecholate molecule. The HOMO energy, E_{HOMO}, has been reported to strongly influence the oxidation potential (Dance, 2006). Nematollahi et al. (2010), for example, reported that the oxidation potential had a near linear relationship with E_{HOMO}. This means that it is possible to evaluate the oxidation potential during Fe^{3+}-catecholate complex decomposition using E_{HOMO}. Fig. 4-3 illustrates the HOMOs of the three Fe^{3+}-catecholate complexes with their corresponding energies (i.e., E_{HOMO}). The HOMO is localized on the π orbitals of C_6H_4 part for tris- and bis-catecholate complexes while for the mono-catecholate complex, it is localized on the lone pair orbital of oxygen atoms. The HOMO energy level goes up with increase in the number of coordinated catechol molecule, so tris-catecholate complexes, $[Fe(cat)_3]^{3-}$, had the highest value for E_{HOMO} (-7.249 eV) among the three Fe^{3+} -catecholate complexes. At higher E_{HOMO}, removal of electrons from HOMO is easier, so the DFT calculations predict that the oxidative decomposition of $[Fe(cat)_3]^{3-}$ would occur at lower electrode potentials than the other two complexes. The predications of DFT calculations were consistent with the LSV measurement results on both Pt and pyrite electrodes; that is, $[Fe(cat)_3]^{3-}$ decomposition occurred at around + 0.2 V, which was lower than those of $[Fe(cat)_2]^-$ (about + 0.3 V) and $[Fe(cat)]^+$ (about + 0.48 V). In addition, E_{HOMO} of $[Fe(cat)_2]^-$ decreases to - 7.891 eV while that of $[Fe(cat)]^+$ was even lower at - 8.109 eV, suggesting that once $[Fe(cat)_3]^{3-}$ is oxidatively decomposed to $[Fe(cat)_2]^-$, higher electrode potentials are required for the next sequential oxidation steps ($[Fe(cat)_2]^- \rightarrow [Fe(cat)]^+ \rightarrow Fe^{3+}$). These deductions are also consistent with the results of LSV on Pt and pyrite electrodes showing that the oxidation peaks of $[Fe(cat)_2]^-$ and $[Fe(cat)]^+$ occurred at higher applied potentials (Fig. 4-2).

4.3.2 Coating formation on the rotating disk-type Pt electrode

When the sequential decomposition of Fe^{3+}-catecholate complexes on the pyrite surface is completed, Fe^{3+} is released, precipitated rapidly as Fe-oxyhydroxide at pH > 4, and under certain condition may act as a protective coating of pyrite (Eq. 4-5) (Li et al., 2019).

$$Fe^{3+} + 3\ OH^- \rightarrow Fe(OH)_3 \tag{4-5}$$

Electrochemical measurements using a rotating disk-type electrode require the use of electrodes with a surface that is perfectly circular in shape, a requirement that is very difficult to achieve using a natural mineral sample. Fortunately, the oxidative decomposition of Fe^{3+}-catecholate complexes on pyrite was identical to that on Pt as discussed in the previous section, so instead of pyrite, chronoamperometry-EIS measurements were done on Pt to elucidate the mechanisms of coating formation and growth. The use of Pt rather than pyrite as the working electrode for the rotating disk-type electrochemical studies also has the following advantages: (1) the complex effects of pyrite oxidation as a side-reaction is eliminated simplifying the analysis of EIS, and (2) the absence of oxidation products from pyrite like Fe-oxyhydroxide/oxide makes it easier to characterize the coating formed by Fe^{3+}-catecholate complexes by surface analytical techniques like SEM-EDX.

A constant potential of + 0.8 V was applied on the Pt electrode and 10 cycles of 1-min chronoamperometry and EIS were conducted. This applied potential (i.e., + 0.8 V) was much higher than the observed potential whereby Fe^{3+}-catecholate complexes are completely decomposed to release Fe^{3+} (+ 0.48 V). Fig. 4-4 shows the current measured during the 10 sets of 1-min chronoamperometry as a function of time. The current dramatically decreased with time in the 1st set of 1-min chronoamperometry results but from the 2nd until the 10th sets, the current decrease was more gradual. These results suggest that the rate of Fe^{3+}-catecholate complex decomposition was rapid on the fresh Pt electrode surface but becomes less extensive with time. In a rotating electrode system, the supply of reactants (Fe^{3+}-catecholate complexes) to the surface of electrode is almost constant, so the decrease in the extent of complex decomposition could not be attributed to the depletion of reactants near the surface of the electrode. In addition, the amounts of Fe^{3+}-catecholate complex consumed through electrochemical decomposition can be calculated from the measured current. Based on our estimates, less than 1.60×10^{-4} mM of Fe^{3+}-catecholate complex were decomposed in each cycle of the chronoamperometry, which were negligible in relation to the initial concentration of Fe^{3+}-catecholate complexes. This means that the most probable explanation for the current decrease is the formation of a passivating coating that limited Fe^{3+}-catecholate complexes decomposition.

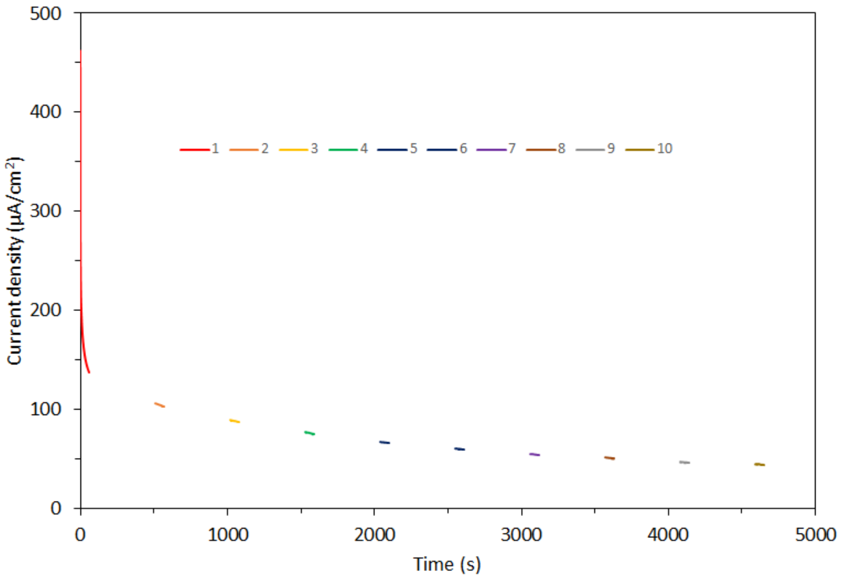

Fig. 4-4 Amounts of current generated with time from the oxidative decomposition of Fe^{3+}-catecholate complexes on a rotating disk-type Pt electrode. Note that the numbers denote sequence of 1-minute chronoamperometry-EIS cycles.

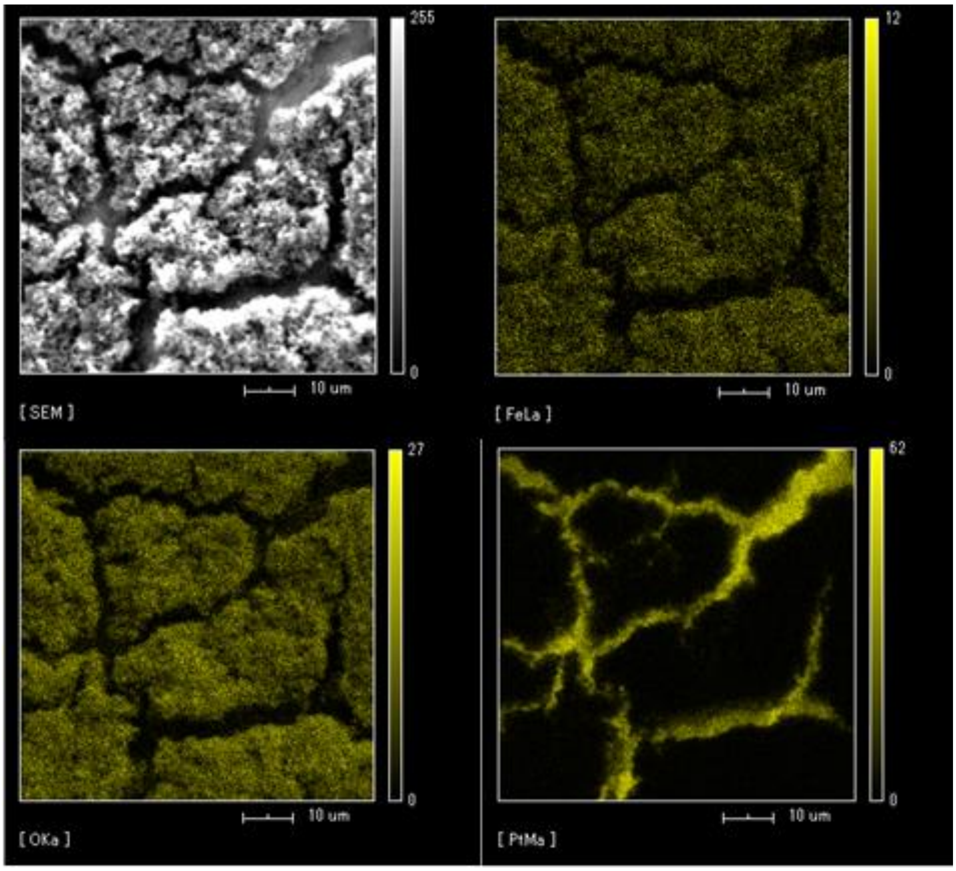

Fig. 4-5 Surface observation and chemical analysis of rotating Pt disk electrode after chronoamperometry-EIS using SEM-EDX

The results of SEM-EDX analysis of the Pt electrode after chronoamperometry-EIS measurements (Fig. 4-5) confirmed the formation of a coating primarily composed of Fe and O, which is most probably Fe-oxyhydroxide/oxide (Eq. 4-5).

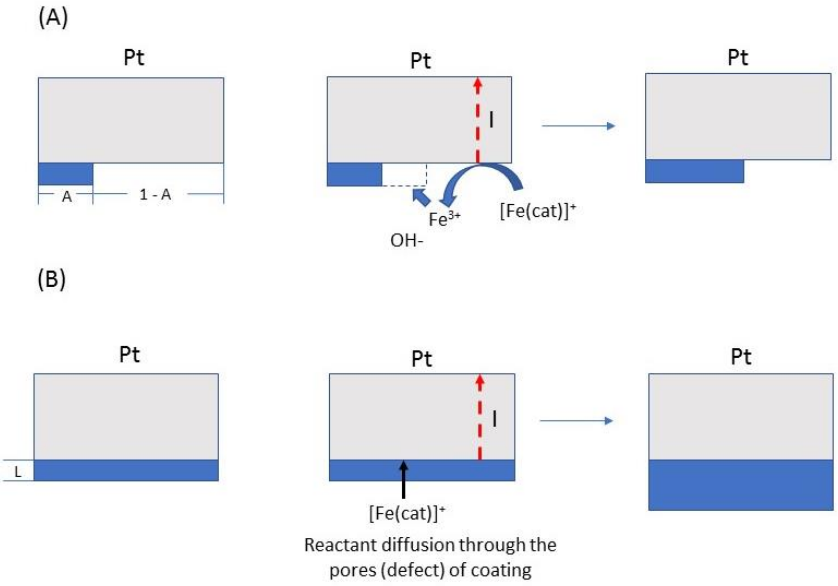

Fig. 4-6 Schematic diagrams of kinetic models for coating growth on Pt electrode

As discussed previously, the decrease in current observed during the rotating disk-type electrode experiment was likely because of coating growth on the Pt electrode. Figs. 4-6(A) and (B) show two kinetic models explaining two possible coating growth mechanisms of coating and are used to analyze the current data shown in Fig. 4-4. Kinetic model (A) assumes that the coating area increases but the coating thickness is kept constant. Because the coating is caused by the oxidative decomposition of Fe^{3+}-catecholate complexes (Eq. 4-4) and precipitation of Fe^{3+} (Eq. 4-5), the rate of coating area expansion (dA/dt) should be proportional to the current (I) as shown in Eq. 4-6.

$$dA/dt \propto I \qquad (4\text{-}6)$$

Kinetic model (A) also assumes that the contact between Fe^{3+}-catecholate complexes and the Pt electrode is prevented by the coating, so current due to Fe^{3+}-catecholate complex decomposition is generated only on the uncoated area of the Pt electrode. If this is the case, current (I) should be proportional to the uncoated area. If the total area is assumed to be 1, the uncoated area can be represented as 1-A, and the following relation is obtained:

$$I \propto 1 - A \qquad (4\text{-}7)$$

By combining Eqs. 4-6 and 4-7, a differential equation is obtained and solving this equation results in this relationship between current and time:

$\ln I \propto -t$ (4-8)

In kinetic model (B), it is assumed that the Pt electrode surface is completely covered by a thin porous coating during the initial periods of the experiment and the reactant (Fe^{3+}-catechol complex) diffuses from the solution phase to the Pt electrode surface through pores or defects within the coating layer. Oxidative decomposition of Fe^{3+}-catecholate complex and the subsequent precipitation of Fe-oxyhydroxides would increase the coating thickness (L) with time. In other words, the rate of coating thickness increase, dL/dt, is proportional to the current, I, as explained by Eq. 4-9.

$dL/dt \propto I$ (4-9)

The current, I, is proportional to the diffusion rate of Fe^{3+}-catecholate complex through the coating, so the diffusion rate can be considered proportional to 1/L when (1) the concentration of Fe^{3+}-catecholate complex in bulk solution is constant, (2) Fe^{3+}-catecholate complex is consumed on Pt surface and its concentration is assumed to be 0 at the surface, and (3) the concentration of Fe^{3+}-catecholate complex is linearly changed through the coating layer. Considering the above, the following relationships are obtained:

$I \propto 1/L$ or $1/I \propto L$ (4-10)

With these, a differential equation, $d(1/I)/dt \propto I$, is derived, and the following relation is obtained by solving the equation.

$I \propto t^{-1/2}$ (4-11)

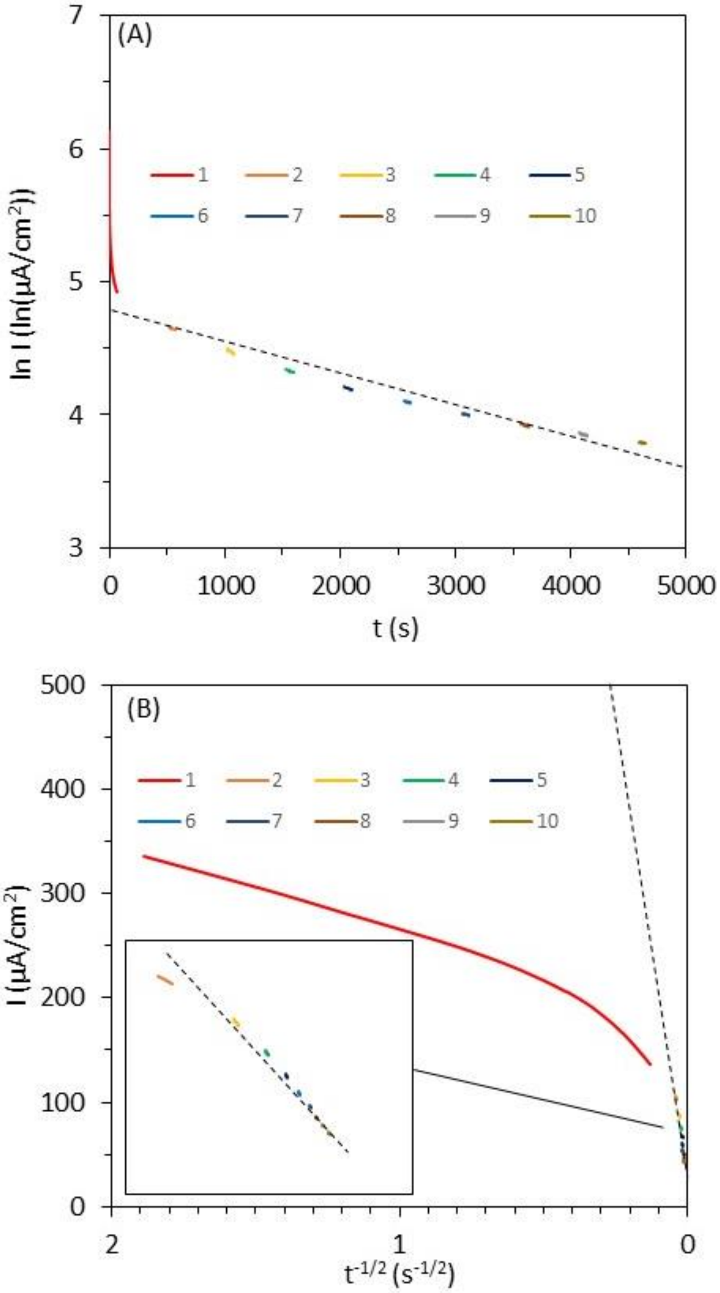

Fig. 4-7 (A) Relationship between ln I and t and (B) relationship between I and t $^{-1/2}$

Figs. 4-7(A) and (B) show the ln I vs. t and I vs. t$^{-1/2}$ plots, respectively. Except for the first set (red line), the experimental data are found close to the straight dashed line shown in each figure. In both figures, the current in the first data set was larger than that expressed by the straight line in Fig. 4-7(A) but was smaller in Fig. 4-7(B).

Smaller initial current in Fig. 4-7(B) is difficult for kinetic model (B) to interpret because higher current is expected on the fresh Pt surface. Larger initial currents in Fig. 4-7(A) is also difficult for kinetic model (A) to interpret. However, the larger initial currents can be interpreted by a modified model; that is, Fe^{3+}-catecholate complex is oxidized initially period on the fresh Pt surface at a very rapid rate, which is immediately followed by formation of a thin coating that covered the surface. This thin coating, however, has many defect and pores, which were gradually filled with precipitates formed via complex decomposition and Fe-oxyhydroxide precipitation, resulting in the reduction of pore/defect area with time. If we consider the area of pore (or defect) corresponded to “1-A” in the kinetic model (A), it is possible to apply Eq. 4-8 for expressing the current-time relation. The validity of the modified model (A) mentioned above is further discussed based on the results of EIS measurements discussed below.

Fig. 4-8 shows the cole-cole plots (impedance spectra) of EIS obtained from each set of 1-min chronoamperometry-EIS. As an example, Fig. 4-8(B) highlights the impedance spectrum after the 1st set of 1-min chronoamperometry. The observed spectrum could be fitted with two semi-circles, indicating that the equivalent circuit involves two parallel circuits composed of a resistor and a capacitor (RC parallel circuits). One of the RC circuits (semi-circle 1) may correspond to the coating on the Pt surface while the other (semi-circle 2) could be related to the double layer capacitance and polarization resistance of the Pt electrode surface exposed to solution in areas without coating or defect sites (e.g. cracks), the presence of which is clearly observed from the SEM-EDX results.

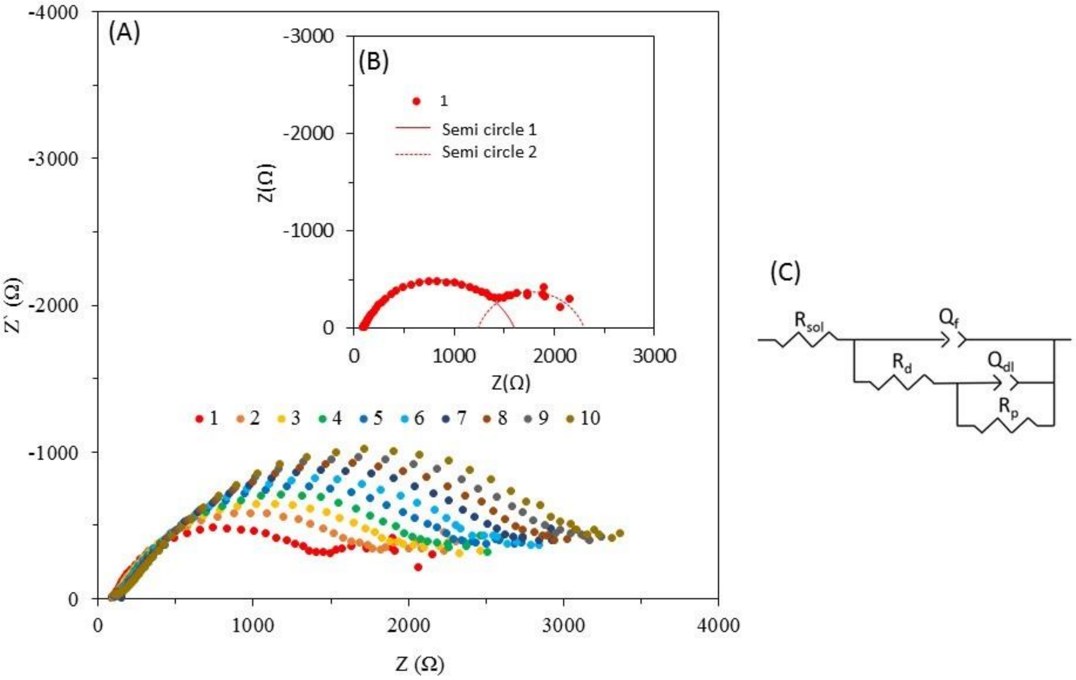

Fig. 4-8 Impedance spectra ((A) and (B)) of rotating Pt electrode after repetitive decomposition of Fe^{3+}-catecholate complexes and (C) the model applied for fitting EIS results.

Model (C) in Fig. 4-8 is an equivalent circuit used to fit the results of EIS wherein R_{sol} represents the solution resistance, R_p is the polarization resistance, Q_{dl} stands for a constant phase element related to the double layer capacitance, Q_f refers to a constant phase element related to the capacitance of coating while R_d stands for the resistance of coating defect. Coating capacitance, C_f, was calculated by fitting results of Q_f (Eq. 4-12) and the time constant, f_{max}, was calculated according to Eq. 4-13 (Itagaki, 2011).

$$C_f = T^{1/P} R_d^{(1-P)/P} \tag{4-12}$$

$$f_{max} = \frac{1}{2\pi R_d C_f} \tag{4-13}$$

Where, T and P are the amplitude and exponential parameters for the constant phase element, Q_f, respectively. The fitting results showed that R_d and C_f increased while f_{max} decreased with repetitive 1-min chronoamperometry measurements (Figs. 4-9(A)-(C)). When the defect area (A_d) is smaller than the electrode surface area (A), the time constant (f_{max}) is proportional to the area ratio of defect in the coating according to the Eq. 4-14 (Itagaki, 2011).

$$\frac{Ad}{A} = 2\pi\rho_{sol}\varepsilon_f f_{max} \tag{4-14}$$

where ρ_{sol} and ε_f stand for the resistivity of solution and permittivity of coating, respectively, and are both considered as constants.

With increasing polarization times, f_{max} decreased, indicating that the coating area increased while the defect area decreased. This means that the decrease in polarization current was due to the increase of coating area coverage on the Pt electrode surface.

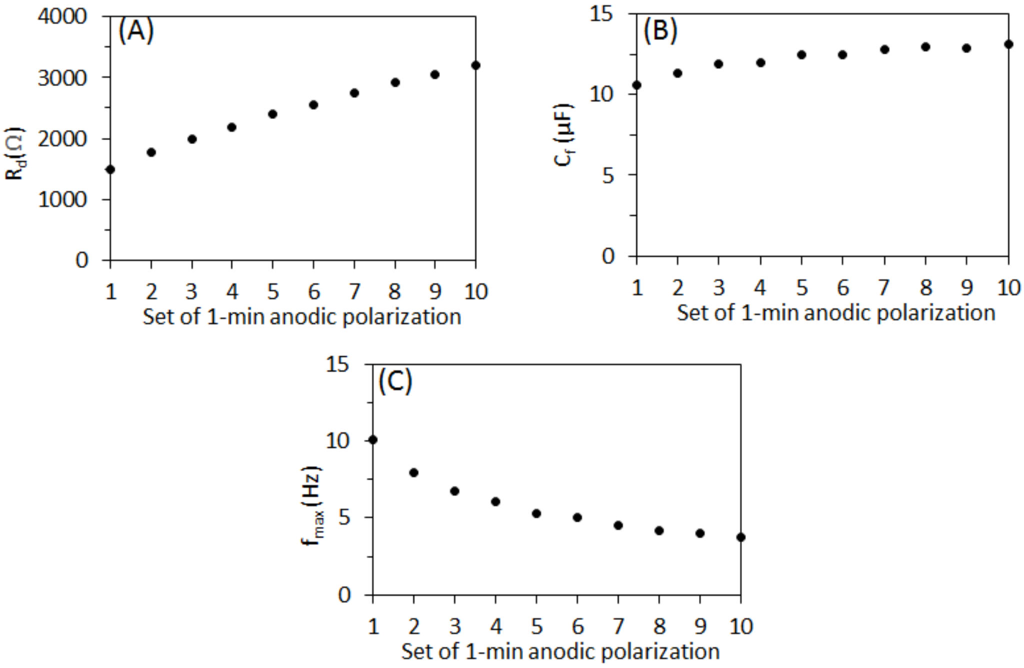

Fig. 4-9 Fitting results of (A) R_d, (B) C_f and (C) f_{max} of coating on Pt rotating disk electrode

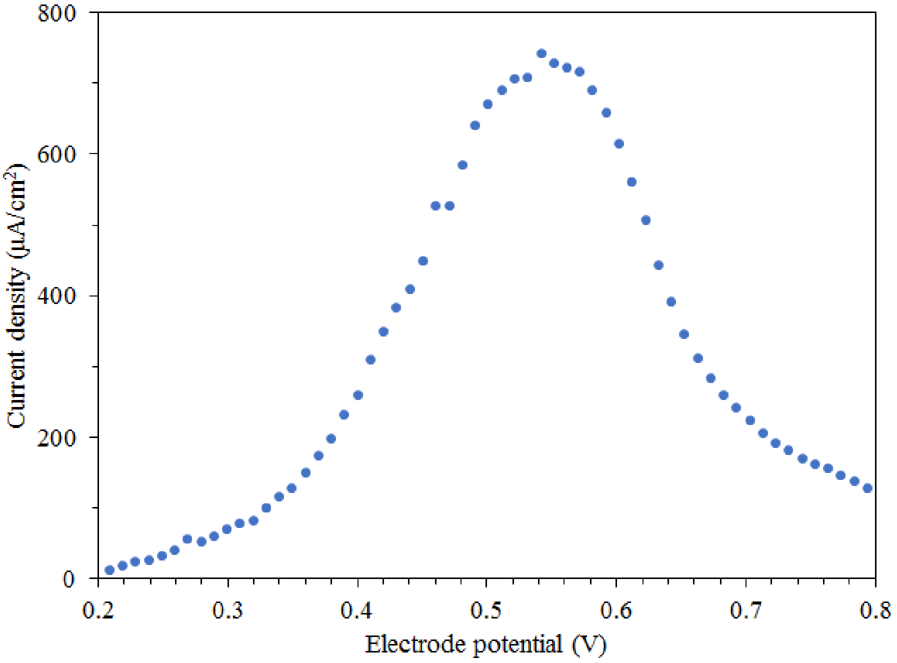

Fig. 4-10 Equilibrium current generated from the oxidative decomposition of Fe^{3+}-catecholate complex under different electrode potentials

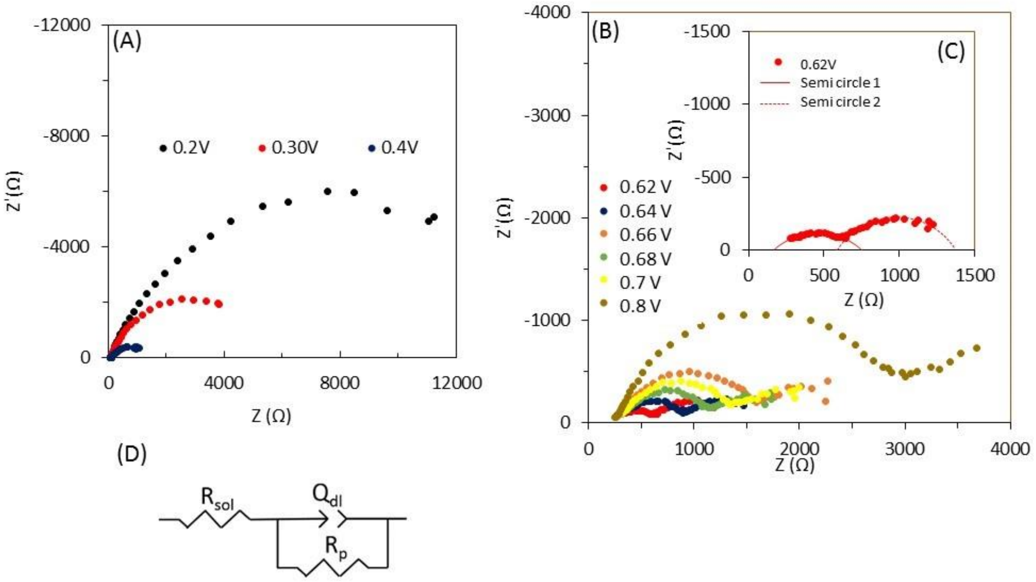

Fig. 4-11 Typical impedance spectra measured on Pt rotating disk electrode after oxidative decomposition of Fe^{3+}-catecholate complexes under various potential and the model applied for fitting EIS results (Model D)

The effects of electrode potential on coating formation are illustrated in Fig. 4-10. The current increased with increasing electrode potential, reached a maximum at around + 0.55 V, and then decreased at higher potentials until + 0.8 V. The increase of the current between + 0.21 V and + 0.55 V could be attributed to the increase of the rate of oxidative decomposition of Fe-catecholate complexes while the decrease of current may be explained by the formation of an inert coating on the Pt electrode, which inhibited the oxidative decomposition of Fe^{3+}-catecholate complexes even at high applied potentials. Figs. 4-11(A) and (B) show the typical impedance spectra under different electrode potentials. At lower potentials (from + 0.2 to + 0.55 V), the data can be fitted with a part of a compressed semi-circle, corresponding to an R-CPE parallel circuit. Based on Fig. 4-11, it could be assumed the coating formed between + 0.2 and + 0.55 V was still negligible, so the resistance, R, and parameter, T, in the R-C parallel circuit (Model (D)) would correspond to the polarization resistance (R_p), and a double layer capacitance on Pt surface, respectively. With increasing electrode potential, the diameter of the semi-circle decreased, which suggest that the polarization resistance, R_p, decreased with increasing potential.

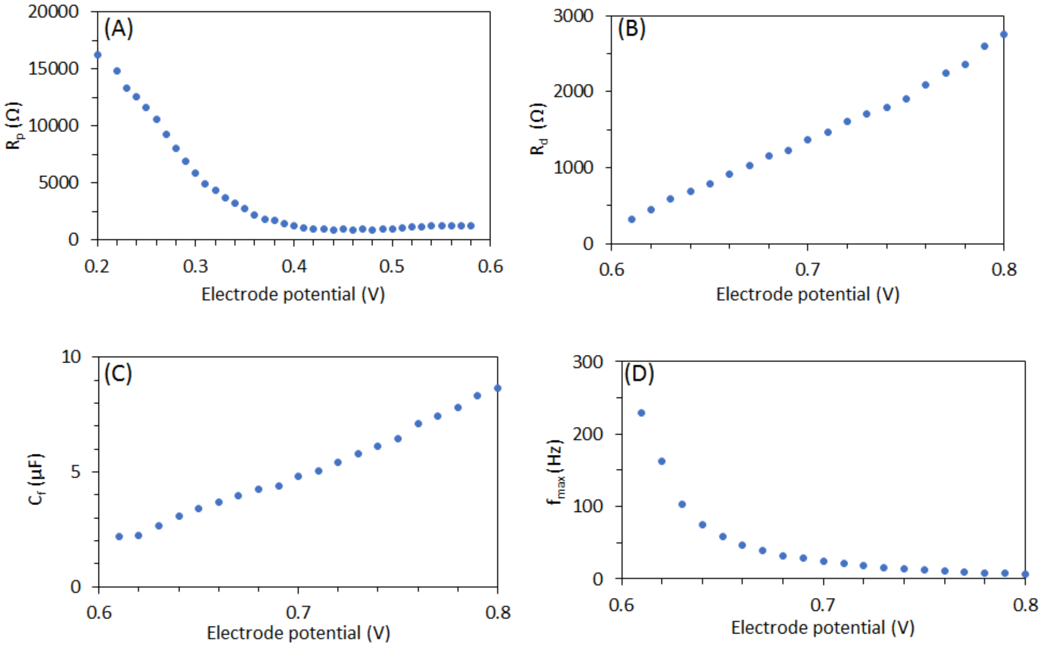

Fig. 4-12 Fitting results of impedance spectra measured after oxidative decomposition of Fe^{3+}-catecholate complexes

At higher electrode potentials (over + 0.6V), the data could be fitted with two semi-circles 1 and 2. With increasing potential, the diameter of semi-circle 1 decreased but that of semi-circle 2 increased. Semi-circle 1 corresponds to the coating while semi-circle 2 could be attributed to the combination of polarization resistance R_p and double layer capacitance on the Pt surface. These results indicate that coating formation occurred when the electrode potential was higher than a critical value (around 0.6 V in the case of experiments shown in Fig. 4-10).

EIS results obtained at + 0.2-0.58V were analyzed with Model (D) as an equivalent circuit. Fig. 4-12(A) shows R_p as a function of the electrode potential. The value of R_p decreased with increasing potential until + 0.45 V, after which, its value stabilized. Similarly, EIS results obtained above + 0.6 V were analyzed with Model (C) as an equivalent circuit. The values of R_d, C_f and f_{max} are shown in Figs. 4-10 (B)-(D) as a function of the electrode potential. With increasing potential, the values of R_d and C_f values increased while that of f_{max} decreased. The different values of R_d, C_f , and f_{max} estimated for the coating formed at different electrode potentials could be explained by the faster rate of complex decomposition and coating formation on the Pt electrode at higher applied potentials.

4.3.3 Effects of coating on the half-cell reactions of pyrite oxidation.

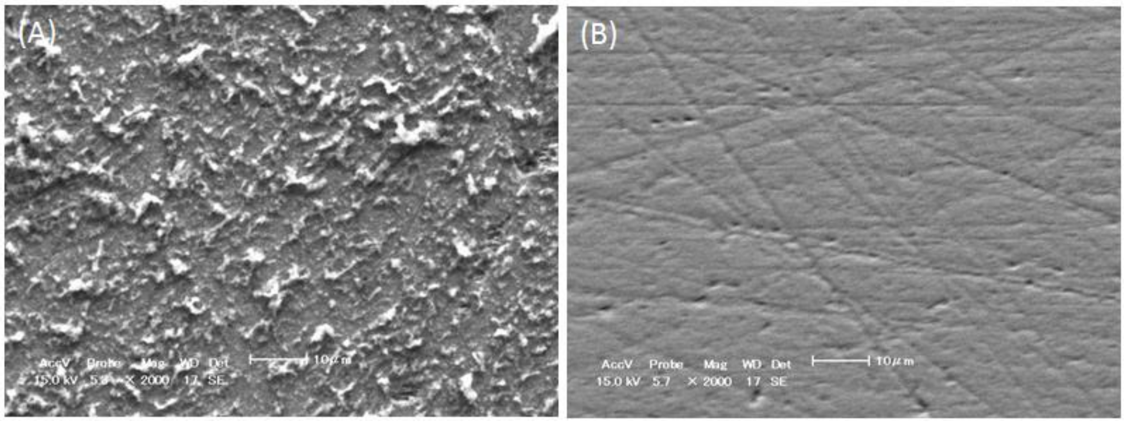

Fig.4-13 SEM photomicrographs of the pyrite electrode surface after pretreatment for 1 day in solutions with (A) and without (B) Fe^{3+}-catecholate complexes

In this section, anodic and cathodic chronoamperometry of coated and uncoated pyrite electrodes were carried out, and the effects of coating formed by Fe^{3+}-catecholate complex decomposition on the anodic and cathodic half-cell reactions of pyrite oxidation are discussed. The coated electrode was prepared by immersing the pyrite electrode in Fe^{3+}-catecholate solution for 24 h under aerobic conditions and coating formation was confirmed by SEM observations (Fig. 4-13).

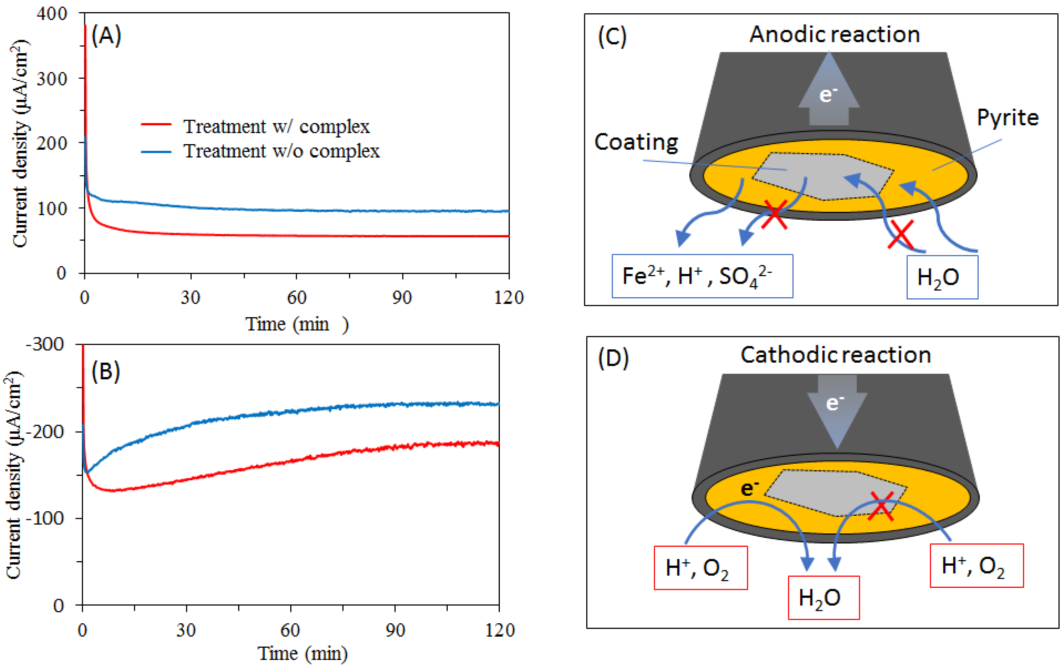

Fig. 4-14 Current density generated during the (A) anodic reaction at + 0.6 V and (B) cathodic reaction at - 0.2V. Schematic illustrations of (C) anodic and (D) cathodic reactions

Fig. 4-14(A) shows the results of anodic chronoamperometry of pyrite electrode without or with coating formed by Fe^{3+}-catecholate complex. The anodic current was lower in pyrite with coating than that without coating, indicating that the anodic dissolution of pyrite was suppressed by the coating formed by Fe^{3+}-catecholate complexes. This suppressive effect could be attributed to more limited diffusion of reactant (H_2O) and products (Fe^{2+} and SO_4^{2-}) in Eq. 4-15 between bulk solution phase and pyrite surface.

$$FeS_2 + 8\,H_2O \rightarrow Fe^{2+} + 2\,SO_4^{2-} + 16\,H^+ + 14\,e^- \qquad (4\text{-}15)$$

Fig. 4-14(B) shows the results of cathodic chronoamperometry of pyrite electrode without or with coating formed by Fe^{3+}-catecholate complexes. The cathodic current was smaller in the presence of the coating most probably due to the suppression of O_2 reduction on the surface of the pyrite electrode (Eq. 4-16).

$$O_2 + 4\ H^+ + 4e^- \rightarrow 2\ H_2O \qquad (4\text{-}16)$$

According to Rimstidt and Vaughan (2003), adsorption of O_2 to Fe atoms in pyrite is necessary for electron transfer between pyrite and O_2, so the coating formed on pyrite suppressed the cathodic half-cell reaction shown in Eq. 4-16 by physically protecting cathodic sites against O_2 adsorption.

The quantity of electric charge after 2 h of anodic chronoamperometry calculated from the observed current with and without coating were 0.44 and 0.72 C/cm^2, respectively. Using these values, the efficiency of suppression (E) of the half-cell reactions by the coating was calculated according to the Eq. 4-17

$$E = (Q_0 - Q) / Q_0 \qquad (4\text{-}17)$$

where Q and Q_0 are the amounts of electric charge measured with and without coating, respectively. The results showed that the suppression efficiency of the coating was 39% for the anodic half-cell reaction. A similar calculation method was applied for the cathodic half-cell reaction and the results showed that suppression efficiency of the coating was 34%. Based on these results, the effectiveness of the coating to suppress the anodic and cathodic half-cell reactions of pyrite oxidation was almost similar.

4.4 Conclusions

In this study, the mechanisms of CME using Fe^{3+}-catecholate complexes were evaluated using electrochemical techniques and DFT calculations. The results of LSV showed that Fe^{3+}-catecholate complex decomposition on pyrite was a sequential process; that is, tris-catecholate complex → bis-catecholate complex → mono-catecholate complex → Fe^{3+}. These sequential decomposition reactions occur at different electrode potentials corresponding to the HOMO energy levels of the Fe^{3+}-catecholate complexes. Chronoamperometry-EIS measurements using a rotating disk-type Pt electrode suggest that a passivating coating was formed via the oxidative decomposition of Fe^{3+}-catecholate complexes. With longer decomposition time and higher anodic potentials, defects in the coating decreased that made it more effective. Comparison of chronoamperometry of coated and uncoated pyrite electrodes suggests that the coating limited not only the movement and adsorption of reactants but also the diffusion of products from pyrite to the bulk solution phase, which resulted in the suppression of both anodic and cathodic half-cell reactions of pyrite oxidation.

This chapter is modified from “Li et al., 2019. Suppression of pyrite oxidation by ferric-catecholate complexes: An electrochemical study. Miner. Eng. 138, 226–237”.

References

Cancès, E., Mennucci, B., Tomasi, J., 1997. A new integral equation formalism for the polarizable continuum model: Theoretical background and applications to isotropic and anisotropic dielectrics. J. Chem. Phys. 107, 3032–3041.

Cossi, M., Barone, V., Mennucci, B., Tomasi, J., 1998. Ab initio study of ionic solutions by a polarizable continuum dielectric model. Chem. Phys. Lett. 286, 253–260.

Dance, I., 2006. The Correlation of Redox Potential, HOMO Energy, and Oxidation State in Metal Sulfide Clusters and Its Application to Determine the Redox Level of the FeMo-co Active-Site Cluster of Nitrogenase. Inorg. Chem. 45, 5084–5091.

Gaussian 09, Revision D.01, M. J. Frisch, G. W. Trucks, H. B. Schlegel, G. E. Scuseria, M. A. Robb, J. R. Cheeseman, G. Scalmani, V. Barone, B. Mennucci, G. A. Petersson, H. Nakatsuji, M. Caricato, X. Li, H. P. Hratchian, A. F. Izmaylov, J. Bloino, G. Zheng, J. L. Sonnenberg, M. Hada, M. Ehara, K. Toyota, R. Fukuda, J. Hasegawa, M. Ishida, T. Nakajima, Y. Honda, O. Kitao, H. Nakai, T. Vreven, J. A. Montgomery, Jr., J. E. Peralta, F. Ogliaro, M. Bearpark, J. J. Heyd, E. Brothers, K. N. Kudin, V. N. Staroverov, R. Kobayashi, J. Normand, K. Raghavachari, A. Rendell, J. C. Burant, S. S. Iyengar, J. Tomasi, M. Cossi, N. Rega, J. M. Millam, M. Klene, J. E. Knox, J. B. Cross, V. Bakken, C. Adamo, J. Jaramillo, R. Gomperts, R. E. Stratmann, O. Yazyev, A. J. Austin, R. Cammi, C. Pomelli, J. W. Ochterski, R. L. Martin, K. Morokuma, V. G. Zakrzewski, G. A. Voth, P. Salvador, J. J. Dannenberg, S. Dapprich, A. D. Daniels, Ö. Farkas, J. B. Foresman, J. V. Ortiz, J. Cioslowski, and D. J. Fox, Gaussian, Inc., Wallingford CT, 2009.

Itagaki, M., Electrochemical impedance spectrometry: principle, measurement and analysis (in japanese), 2011, 84-97

Li, X., Hiroyoshi, N., Tabelin, C.B., Naruwa, K., Harada, C., Ito, M., 2019a. Suppressive effects of ferric-catecholate complexes on pyrite oxidation. Chemosphere 214, 70–78.

Mennucci, B., Tomasi, J., 1997. Continuum solvation models: A new approach to the problem of solute’s charge distribution and cavity boundaries. J. Chem. Phys. 106, 5151–5158.

Nematollahi, D., Jameh-Bozorghi, S., Mansouri, A., Dadpou, B., 2010. Experimental and Computational Study on Electrochemical Oxidation of Catechols. Int J Electrochem Sci 5, 13.

Rimstidt, J.D., Vaughan, D.J., 2003. Pyrite oxidation: a state-of-the-art assessment of the reaction mechanism. Geochim. Cosmochim. Acta, Advances in Oxide and Sulfide Mineral Surface Chemistry 67, 873–880.

Tsuneda, T., Hirao, K., 2014. Long-range correction for density functional theory. Wiley Interdiscip. Rev. Comput. Mol. Sci. 4, 375–390.

Yanai, T., Tew, D.P., Handy, N.C., 2004. A new hybrid exchange–correlation functional using the Coulomb-attenuating method (CAM-B3LYP). Chem. Phys. Lett. 393, 51–57.

Chapter 5 Effects of Ferric-catechol derivative complexes on pyrite oxidation

5.1 Introduction

In CME, metal(loid)-organic ligand complexes are oxidatively decomposed on pyrite surface to form oxy-hydroxy metal(loid) coating on pyrite surface, acting as protective barrier against further oxidation towards mineral (Li et al., 2019a, 2019b). Catechol has been widely studied as carrier (ligand) for CME, because it forms water-soluble complexes with various metal(loid) ions like Ti^{4+}, Si^{4+}, Al^{3+} and Fe^{3+}, which is oxidatively decomposed to form coating on semiconductor sulfide minerals like pyrite and arsenopyrite (Jha et al., 2008, 2011, 2012; Park et al, 2018a, 2018b., 2019; Satur et al., 2007; Yuniati et al., 2015a, 2015b). Industrial by-products containing catechol was also studied for CME instead of regent grade catechol: Yuniati et al. (2015a, 2015b) reported that liquid by-product of hydrothermal treatment of biomass and low-rank coal (HTL-LRC) contained high concentration of catechol (≈ 800 mg/L) as complexing agents to form Si^{4+}-catecholate complexes (Si-HTL). Pyrite oxidation was suppressed after treatment by Si-HTL even with presence of iron-oxidizing bacteria (Yuniati et al., 2015a).

From the view point of cost, use of industrial by-products containing catechol or catechol like materials would be attractive. As an example, it was reported that by-product in pulp and oil mills contain catechol derivatives, which have similar structure as catechol but substituted with functional group (Schweigert et al., 2001). If industrial by-products are applied as sources of organic carriers for CME, properties of catechol derivatives should be well understood.

Considering the above, in this chapter, electrochemical properties of Fe^{3+} - catechol derivative complexes were investigated. Due to the induction and resonance effect between functional group and benzene circle, electron donating functional group (EDG), such as $-CH_3$ and $-C_2H_5$ and electron withdrawing functional group (EWG) such as -COOH and $-NO_2$ may affect the protonation of catechol (Nurchi et al., 2009), which is an important process for complex formation; it may also influence the redox properties of metal-catecholate complexes, which is essential for coating formation on pyrite surface in CME. In this chapter, catechol derivatives which are 4-substitued by EDGs ($-CH_3$ or $-C_2H_5$) or EWGs (-COOH or $-NO_2$) were used to investigate the effects of substituted functional group on electrochemical properties of the complexes of Fe^{3+} and catechol derivatives. Ultraviolet-visible light (UV-Vis) spectrophotometry was conducted to investigate the formation of complexes between Fe^{3+} and catechol derivatives. Effects of EDGs and EWGs on the redox properties of Fe^{3+} - complexes was predicted by frontier orbital theory using energy level of highest occupied molecular orbital (E_{HOMO}) and the predictions were verified by linear sweep voltammetry. Coating formation by Fe^{3+}-catechol derivative complexes was studied by electrochemical impedance spectroscopy (EIS). The effects of coating formed from Fe^{3+}-catechol derivative complexes on suppressing reduction of dissolved oxygen (DO) on pyrite surface was investigated by conducting cathodic polarization on pyrite electrode pretreated with various Fe^{3+} - catechol derivative complexes. The effects of Fe^{3+}-catechol derivative complexes on pyrite oxidation were studied by leaching experiments.

5.2 Methodology

5.2.1 Regents

Five kinds of ligands (catechol and catechol derivatives) were used in this study and their structures and abbreviations are listed in Fig.5-1. Catechol ($C_6H_6O_2$, purity of 99 %), 4-ethylcatechol ($C_8H_{10}O_2$, purity > 95.0 %), ferric nitrate nonahydrate ($Fe(NO_3)_3 \cdot 9H_2O$, purity of 99 %), sodium hydroxide (NaOH, purity of 93 %), and sodium nitrate ($NaNO_3$, purity of 99 %) were obtained from Wako Pure Chemical Industries, Ltd., Japan. 4-methylcatechol ($C_7H_8O_2$, purity > 98.0 %), 3,4-dihydroxybenzoic acid (purity > 98.0 %) and 4-nitrocatechol (purity > 98.0 %) were purchased from Tokyo Chemical Industry Co. Ltd., Japan. All the reagents were used without further purification.

5.2.2. Solution preparation

Solutions containing Fe^{3+} - complexes were prepared by mixing $Fe(NO_3)_3 \cdot 9H_2O$ and organic ligands in deionized water (DI water, 18 MΩ·cm, Milli-Q® Water Purification System, Merck Millipore, USA). The pH of solutions was adjusted with NaOH solution to predetermined value (pH 8 or 10). For electrochemical experiments, 0.1 M $NaNO_3$ was added to solutions as supporting electrolyte. All solutions were filtered through syringe-driven membrane filters with 0.2 μm pore size (Sartorius AG, Germany) to remove precipitates and polymerized organic compounds which possibly formed during solution preparation.

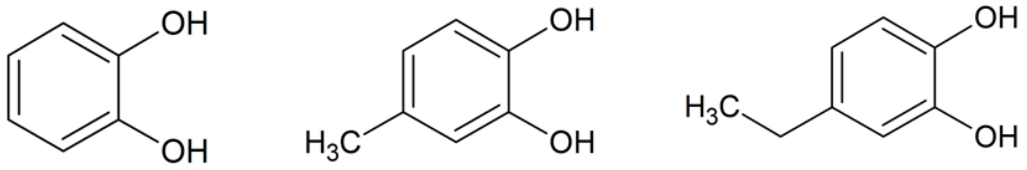

Catechol (H_2cat) 4-methylcatechol (H_2mcat) 4-ethylcatechol (H_2ecat)

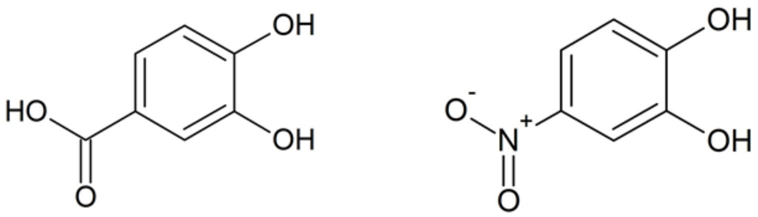

3,4-dihydroxybenzoic acid (H_2xcat) 4-nitrocatechol (H_2ncat)

Fig. 5-1 Structures and abbreviations of catechol and catechol derivatives used in this study

5.2.3 Pyrite sample

Pyrite sample obtained from Cerro de Pasco Mine, Peru was used for preparing a pyrite electrode and leaching experiments. For preparing pyrite working electrode, a single-crystal pyrite specimen was cut into a cuboid by a diamond cutter, connected to copper wires with silver conducting paste, and then embedded inside a plastic holder with Technovit® non-conductive resin (Heraeus Kulzer GmbH, Germany). To expose a surface of pyrite crystal in the working electrode, it was polished with silicon carbide papers of increasing grit numbers (#200, #600, #1000, and #1500). Before each electrochemical experiment, the exposed surface of pyrite electrode was polished with silicon carbide paper (#1200, #1500, #2000, and #3000) and ultrasonically cleaned.

Pyrite sample for leaching experiments was prepared as follows: (1) the pyrite specimen was crushed by a hammer to ca. 2 cm in diameter to remove visible impurities manually. (2) the crushed sample was further crushed by a jaw crusher (BB51, Retsch Inc., Germany) until the size became less than 2 mm, (3) the crushed pyrite was ground by a disk mill (RS 100, Retsch Inc., Germany), and (4) the ground sample was sieved to obtain a predetermined size fraction. To remove attached fine particles and any oxidized layer formed during preparation and storage, the sample was sonicated in ethanol for 30 s, washed with 1 M HNO_3 for 1 min, rinsed with deionized water (DI water, 18 MΩ·cm, Milli-Q® Water Purification System, Merck Millipore, USA) and dewatered with acetone (McKibben and Barnes, 1986).

In the X-ray powder diffraction (XRD) pattern of the sample, the strong signals corresponding to pyrite were detected. Chemical analysis of the sample by a wet method (i.e., microwave digestion and inductively coupled plasma atomic emission spectrometry, ICP-AES, ICPE 9820, Shimadzu Corporation, Japan) showed that total amount of impurities like Si, Ca, Cu, and Zn was about 3 %.

5.2.4 UV-Vis spectrophotometry

Solutions (pH 10) containing 0.1 mM Fe^{3+} and 0.3 mM catechol derivatives were examined by UV-Vis spectrophotometry using V-630 spectrophotometer (Jasco Analytical Instruments, USA). A temperature controller (EHC-716, Jasco Analytical Instruments, USA) was used to maintain constant temperature at 25℃. Spectra were taken from 750 nm to 350 nm at a scan rate of 100 nm/min.

5.2.5 Theoretical calculation

Density Functional Theory (DFT) calculations with hybrid functionals were performed to determine geometries, energies, and highest occupied molecular orbital (HOMO) energy levels (E_{HOMO}) of tris-complex molecules formed between Fe^{3+} and catechol or catechol derivatives using Gaussian 09 program (rev. D01). The functional CAM-B3LYP with 6-311+G** basis set was employed in all calculations. It has been reported that the long-range corrected functional could reproduce the orbital energy accurately and with high degrees of certainty. The water solvation effect was included in the calculations using a polarizable continuum model (Li et al., 2019b).

5.2.6 Electrochemical studies

5.2.6.1 Linear sweep voltammetry

Complex solutions used for LSV were prepared by dissolving 1 mM Fe^{3+} and 3 mM organic ligand (catechol or catechol derivatives) in 0.1 M $NaNO_3$ solution. With pH adjustment by NaOH solution to pH 10 and filtration by syringe-driven membrane filters with 0.2 μm pore size, 12 ml of the complex solutions were poured into a water-jacketed cell connected with constant temperature water recirculating bath maintaining the temperature to 25℃. N_2 (purity, 99.999 %) was induced into the solution for 30 min to remove dissolved O_2 before the measurement.

A conventional three-electrode system connected to a Solartron electrochemical measurement unit (SI 1280B, Solartron Instruments, UK) was used. A Pt electrode with a surface area of 7.06 mm^2 was used as working electrode. An Ag/AgCl electrode filled with 3 M NaCl and a Pt wire were used as reference electrode and counter electrode, respectively. All electrode potentials mentioned in this chapter are based on the Ag/AgCl electrode. Linear sweep voltammetry measurement was started from the open circuit potential (OCP) where net current on the working electrode surface was zero and terminated at + 0.8 V. The change in current density with increasing electrode potential was recorded.

5.2.6.2 EIS measurements and chronoamperometry

To investigate the formation of protective coatings by the anodic decomposition of Fe^{3+}-catechol derivative complexes, EIS measurement were carried out using pyrite working electrode. A Pt electrode and an Ag/AgCl/statured KCl electrode were used as counter and reference electrode, respectively. Coating was formed by applying + 0.3 V on pyrite electrode immersed in 120 ml of 0.1 M $NaNO_3$ solution containing 5 mM Fe^{3+} and 10 mM catechol derivatives (pH 8) under N_2 atmosphere for 1 h (10 mins × 6 times). After coating was formed on pyrite electrode surface, pyrite electrode was washed and moved to another solution containing only 0.1 M $NaNO_3$ for EIS measurement (DC bias, 0 V vs open circuit potential (OCP); AC amplitude, 5 mV; AC frequency, 20,000 Hz to 0.1 Hz) under air atmosphere. The results of EIS were fitted by equivalent circuit using the ZView® software (Solartron Analytical, UK).

After finishing the measurement of EIS, cathodic polarization at - 0.2 V was applied to pyrite electrode. The change of current density with time was plotted.

5.2.7 Leaching experiment

Complex solutions used for leaching experiments were prepared by dissolving 5 mM Fe^{3+} and 10 mM ligand in 0.5 M tris(hydroxymethyl)aminomethane buffer solution (pH 8). Leaching experiments were carried out by mixing 1 g of washed ground pyrite and 10 ml complex solution in

50 ml Erlenmeyer flask shaken at 120 strokes/min in a constant temperature water bath maintained at 25 °C. At predetermined time intervals, suspensions were collected and filtered using a syringe-driven membrane filter (pore size, 0.2 µm). The filtrates were analyzed for dissolved Fe and S concentrations using ICP-AES (margin of error = ± 2%).

5.3 Results and discussion

5.3.1 Characterization of Fe^{3+}-complexes with catechol and catechol derivatives

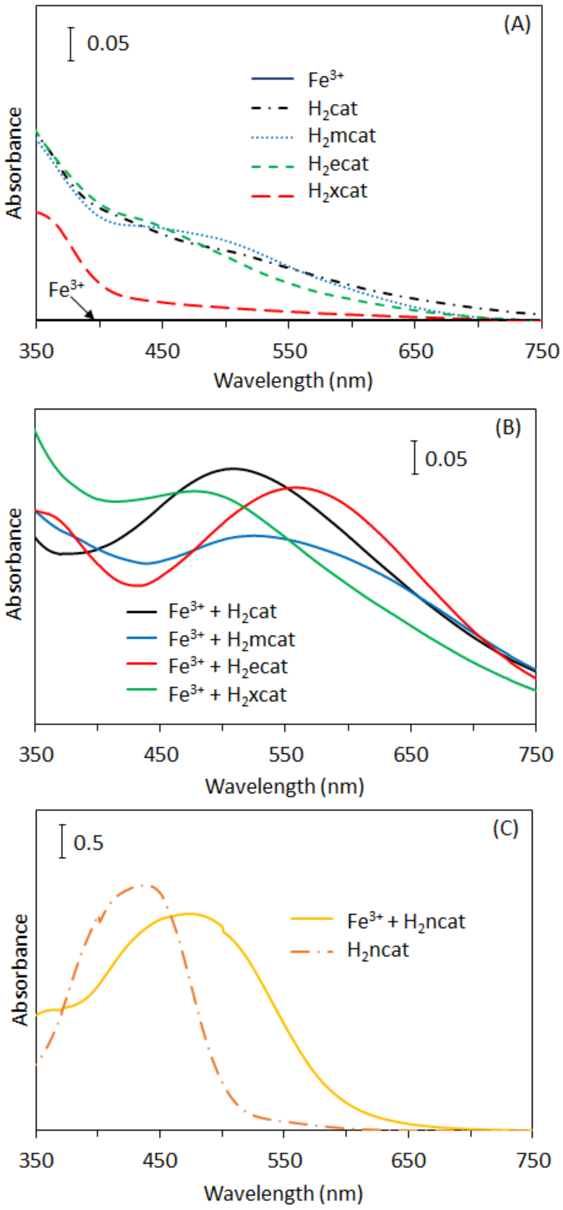

Fig. 5-2 UV-Vis spectra of solution containing (A) Fe^{3+} or ligand (except H_2ncat) (B) Fe^{3+} and ligand (except H_2ncat) and (C) H_2ncat with or without Fe^{3+}

As reported in the previous chapters, catechol could coordinate with Fe^{3+} to form mono-, bis- and tris-catecholate complexes under different pH. At pH 10, as shown in Fig. 5-2, an absorbance peak around 508 nm was observed in the solution containing Fe^{3+} and catechol (Fig. 5-2 (B)), while it was not observed when solution contained only catechol (Fig. 5-2 (A)). This absorbance peak could be attributed to the presence of $[Fe(cat)_3]^{3-}$ as discussed in chapter 3. In the solution containing only ligand like H_2mcat, H_2ecat and H_2xcat, no absorbance peak was observed while the absorbance peaks were observed at 524, 478, and 557 nm in the solution containing Fe^{3+}-H_2mcat, Fe^{3+}-H_2ecat and Fe^{3+}-H_2xcat, respectively. The results indicated complexes were formed between Fe^{3+} and catechol derivatives. Although coordination number of the derivatives in the complexes are not certain, by considering similarity of the structure of the ligands like H_2ecat, H_2mcat, H_2xcat and H_2cat, it can be assumed that the complexes is most likely tris-coordinated, which could be represented as $[Fe(mcat)_3]^{3-}$, $[Fe(ecat)_3]^{3-}$ and $[Fe(xcat)]^{3-}$, respectively. For solution containing H_2ncat, since the nitro-group is a chromophore, absorbance at 437nm was observed in the solution containing only H_2ncat (Fig. 5-2(C)). When Fe^{3+} present with H_2ncat, new absorbance peaks at 364 and 476 nm appeared. According to the thermodynamic constants reported by Nurchi et al. (2009), the speciation diagram of Fe -H_2ncat complexes was calculated using Hyss and the result shown in Fig. 5-3 indicated that at pH 10, the dominant species is tris-species, so, the peaks at 364 and 476 nm are considered to be corresponding to the presence of $[Fe(ncat)_3]^{3-}$.

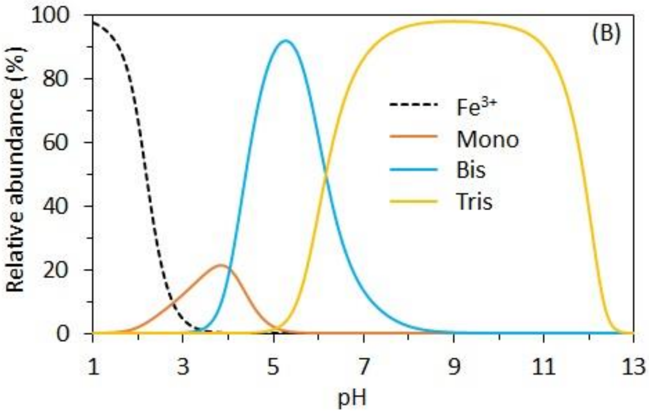

Fig. 5-3 Speciation diagram of Fe-H_2ncat complexes (condition set for calculation: 0.1 mM Fe^{3+} and 0.3 mM H_2ncat)

5.3.2 Redox properties of Fe^{3+}-catechol derivative complexes

As an essential step of CME, the complexes oxidatively decomposed on pyrite surface and released metal ion on the surface, resulting in the formation of protective coating. The previous chapters showed that decomposition of Fe^{3+}-catecholate complexes is a sequential process as shown in Eqs. 5-1 to 5-3:

$$[Fe(cat)_3]^{3-} \rightarrow [Fe(cat)_2]^{-} + Q + 2\ e^- \quad (5\text{-}1)$$

$$[Fe(cat)_2]^{-} \rightarrow [Fe(cat)]^{+} + Q + 2\ e^- \quad (5\text{-}2)$$

$$[Fe(cat)]^{+} \rightarrow Fe^{3+} + Q + 2\ e^- \quad (5\text{-}3)$$

The oxidative decomposition of Fe^{3+}-complexes could be considered as a process that electrons remove from the complex. The effects of EDGs and EWGs substituted in catechol on redox properties of Fe^{3+}-catechol derivative complexes may be predicted based on E_{HOMO} (Li et al., 2019b). Calculated value of E_{HOMO} for $[Fe(cat)_3]^{3-}$ is - 7.25 eV. For $[Fe(mcat)_3]^{3-}$ and $[Fe(ecat)_3]^{3-}$, the values of E_{HOMO} were increased to - 7.21 eV and - 7.19 eV, respectively, suggesting that the oxidation of complexes may be achieved at lower electrode potentials. On the other hand, for $[Fe(xcat)_3]^{3-}$ and $[Fe(ncat)_3]^{3-}$, the values of E_{HOMO} decreased to - 7.37 eV and - 7.57 eV, respectively, indicating the oxidative decomposition may occur at higher electrode potentials than $[Fe(cat)_3]^{3-}$.

For verifying the prediction based on the values of E_{HOMO}, LSV of various Fe-catechol derivative complexes was conducted. As shown in Fig. 5-4, polarization curves with multi current peaks were observed in the case of $[Fe(cat)_3]^{3-}$. In the previous studies, the current peak at around + 0.12, + 0.3 and + 0.42 V corresponded to Eqs. 5-1, 5-2 and 5-3, respectively and the peak at around + 0.6 V was attributed to the oxidation of free catechol as shown in Eq. 5-4.

$$H_2cat \rightarrow Q + 2\ e^- \quad (5\text{-}4)$$

For $[Fe(mcat)_3]^{3-}$ and $[Fe(ecat)_3]^{3-}$, multi current peaks (or shoulders) were detected. The presence of multi current peaks indicates that the oxidation of these complexes is sequential process. It may be considered that at around + 0.12 V, $[Fe(mcat)_3]^{3-}$ and $[Fe(ecat)_3]^{3-}$ were oxidatively decomposed to form $[Fe(mcat)_2]^-$ and $[Fe(ecat)_2]^-$ (Eq. 5-5); $[Fe(mcat)_2]^-$ and $[Fe(ecat)_2]^-$ were further oxidized around + 0.24 V to form $[Fe(mcat)]^+$ and $[Fe(ecat)]^+$ (Eq.5-6); $[Fe(mcat)]^+$ and $[Fe(ecat)]^+$ was oxidized to release Fe^{3+} around + 0.35 V (Eq. 5-7). Besides, the current peaks observed at around + 0.5 V could be attributed to the oxidation of free H_2mat and H_2ecat (Eq.5-8).

$[Fe(Rcat)_3]^{3-} \rightarrow [Fe(Rcat)_2]^{-} + RQ + 2\ e^-$ (5-5)

$[Fe(Rcat)_2]^{-} \rightarrow [Fe(Rcat)]^{+} + RQ + 2\ e^-$ (5-6)

$[Fe(Rcat)]^{+} \rightarrow Fe^{3+} + RQ + 2\ e^-$ (5-7)

$H_2Rcat \rightarrow RQ + 2\ e^-$ (5-8)

Where Rcat and RQ represents for the catecholate and quinone 4-substituted by additional functional group (R).

For the case of $[Fe(xcat)_3]^{3-}$, three current peaks (shoulder) were detected at around + 0.35, + 0.4 and + 0.53 V, which could be attributed to Eq. 5-5, 5-6, and 5-7, respectively. For $[Fe(ncat)_3]^{3-}$, in the measuring range, only two current peaks (shoulders) that may correspond to Eqs. 5-5 and 5-6 appeared at around + 0.44 and + 0.68 V were observed. The electrode potential of current peaks in different Fe-catechol/catechol derivative complexes were plotted in Fig. 5-4(B). The results indicated that when EDGs like $-CH_3$ or $-CH_2CH_3$ presents in the ligand of the complexes, the electrode potential for oxidative decomposition of Fe^{3+}-complexes were lower than that without EDGs while EWGs like -COOH and $-NO_2$ caused higher electrode potentials for the complex decomposition.

Fig. 5-5 shows the relation between the calculated values of E_{HOMO} and the observed peak potential of the decomposition of tris-complexes (corresponding to Eq. 5-1 or 5-5). Approximately, a linear relationship was obtained between E_{HOMO} and the initial peak potentials, indicating that the results of theoretical calculation were in line with the experimental results.

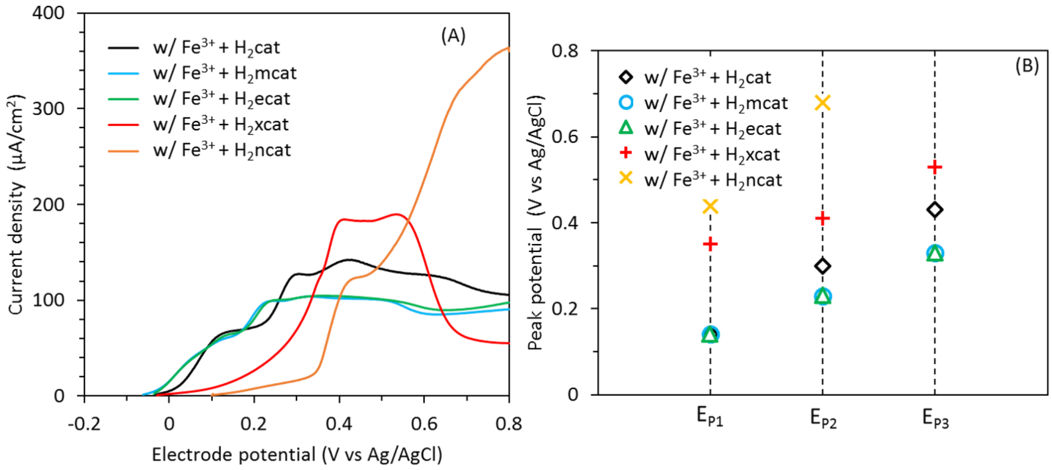

Fig. 5-4 (A) Linear sweep voltammograms of Fe^{3+}-catechol/catechol derivative complexes and (B) electrode potential of anodic current peak observed in (A).

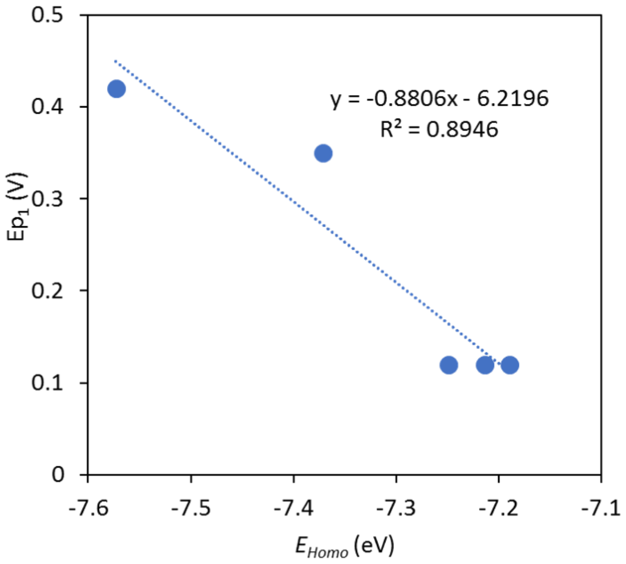

Fig. 5-5 Relationship between E_{p1} and E_{HOMO} of Fe^{3+}-catechol/catechol derivative complexes

5.3.3 Coating formation

In the last section, the redox properties of Fe^{3+}-catechol/catechol derivative complexes were studied. When complexes were completely decomposed, Fe^{3+} was released and precipitated as protective coatings on pyrite surface, so the coating formation could be strongly affected by the redox properties of Fe^{3+}-catechol/catechol derivative complexes. For understanding the effects of EDGs and EWGs substituted in catecholate of complexes on coating formation, EIS measurement was conducted on pyrite electrode pretreated in solutions containing Fe^{3+}-catechol/catechol derivative complexes. As shown in Fig. 5-6(A), when pyrite electrode was treated without Fe^{3+} and ligands as control condition, the result of EIS seemed as an inclined line in Cole-Cole plot. It indicated that no RC parallel circuit corresponding to the presence of coating on the pyrite electrode surface was found. The results of EIS of pyrite pretreated in solution containing Fe^{3+}-H_2xcat or Fe^{3+}-H_2ncat also gave the similar results as the one obtained in control condition, suggesting that coatings may not be formed with pretreatment in the complexes solution mentioned above. Equivalent circuit (A) including solution resistance (R_s) and impedance of a finite-length diffusion with transmissive boundary (Warburg impedance, W_s) was applied for fitting the EIS result in Fig. 5-6(A) and the fitting results were shown in this figure as solid straight lines.

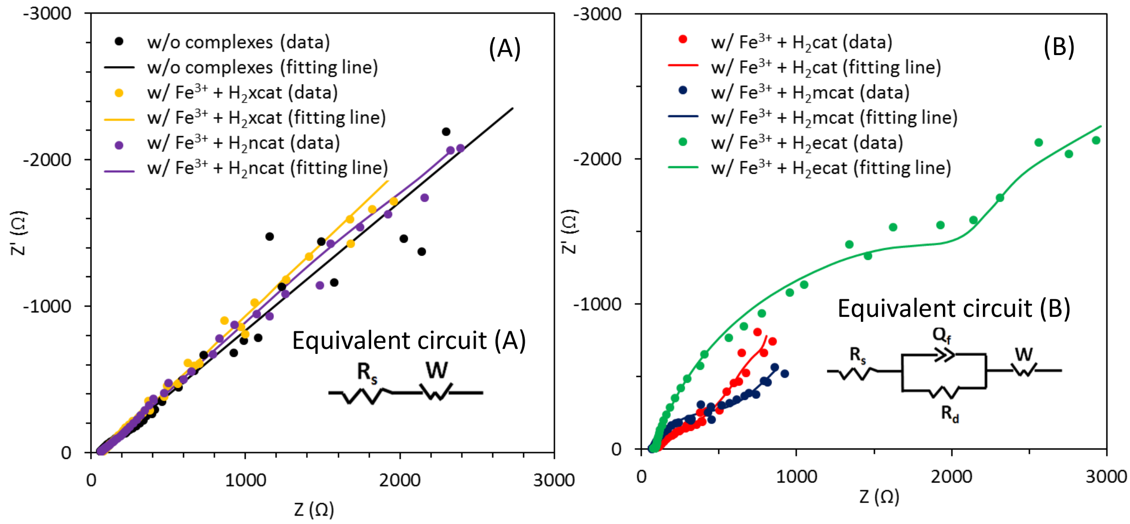

Fig. 5-6 EIS spectra and fitting results of pyrite electrode pretreated in Fe^{3+}-catechol/catechol derivative complex solutions

Fig 5-6(B) showed the results of EIS of the electrodes pretreated in the solution containing Fe^{3+}-H_2cat, Fe^{3+}-H_2mcat or Fe^{3+}-H_2ecat. The results can be approximately plotted on the combination of a part of semi-circle and inclined straight lines. The semi-circles may correspond to the presence of coating and the inclined straight lines may be due to the diffusion of reactant or product. To analyze EIS results in Fig. 5-6(B), equivalent circuit (B) composed of a solution resistance (Rs), a Warburg impedance (Ws), a resistance (R_d) corresponding to the resistance of coating defect, and a constant phase element (Q_f), was used. The Q_f here is used as a "modified" capacitance which corresponds to the capacitance of ununiform coating. The fitting results were shown in the Fig. 5-6(B) as solid lines and the fitted values of parameter of electrical elements in equivalent circuit (B) were listed in Table 5-1. Comparing to R_d in the coating formed with Fe^{3+}-H_2cat and Fe-H_2mcat, the value of the resistance of R_d for Fe^{3+}-H_2ecat was much higher.

When we assume that R_d is the resistant of defect in the coating, R_d is expressed as Eq. 5-9,

$$R_d = \rho L/A \tag{5-9}$$

Where ρ, L, A represent for resistivity of the solution in defect area, thickness of coating and area of defect in the coating, respectively.

Table 5-1 Fitting results of EIS spectra of pyrite electrode in solution containing Fe^{3+}-H_2cat, Fe^{3+}-H_2mcat and Fe^{3+}-H_2ecat

	Fe^{3+}-H_2cat	Fe^{3+}-H_2mcat	Fe^{3+}-H_2ecat
Rs (Ω)	98.12	69.74	84.61
R_d (Ω)	307.6	409.6	2318
Qc-T	0.0004808	0.000303	0.00018
Qc-P	0.61623	0.81095	0.86586
Ws-R (Ω)	3368	2867	2400
Ws-T	10.57	19	3.815
Ws-P	0.68507	0.58817	0.69035

If the differences of solution resistivity for Fe^{3+}-H_2cat, Fe^{3+}-H_2mcat and Fe^{3+}-H_2ecat can be disregarded, the higher R_d value could be attributed to smaller defect area and/or thicker coating. It suggested that Fe-H_2ecat may form coating with large thickness or smaller defect area than those with Fe^{3+}-H_2cat, and Fe^{3+}-H_2mcat. As shown in Fig. 5-4, $[Fe(ecat)_3]^{3-}$ and $[Fe(mcat)_3]^{3-}$ could be decomposed more easily than $[Fe(cat)_3]^{3-}$, therefore, during the pretreatment under same potential, more complexes may be decomposed at lower electrode potential, resulting in formation of more coating on pyrite surface.

The effects of pretreatment with Fe-catechol/catechol derivative complexes were further evaluated by chronoamperometry at - 0.2 V on pretreated pyrite electrode. At - 0.2 V, dissolve O_2 was reduced on pyrite surface according to

$$O_2 + 2\ H_2O + 4\ e^- \rightarrow\ 4\ OH^- \qquad (5\text{-}10)$$

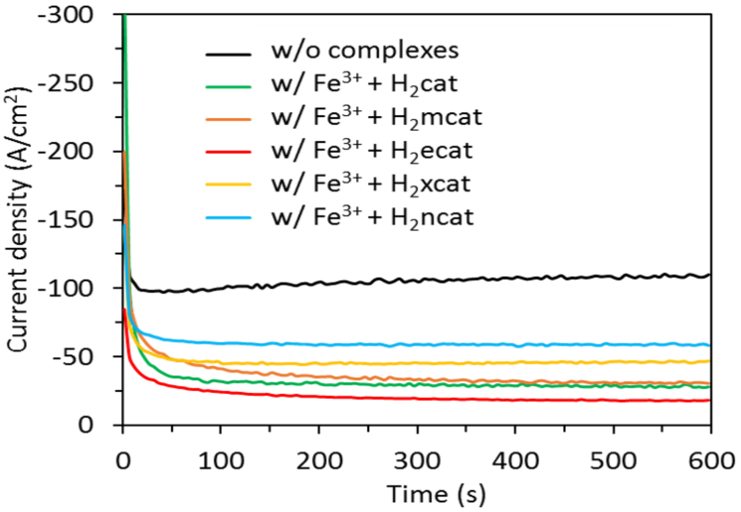

Fig. 5-7 Chronoamperometry at - 0.2 V on pyrite electrode pretreated with or without Fe-catechol/catechol derivative complexes

As shown in Fig. 5-7, for the case pretreated without Fe^{3+} and organic ligand (control condition), a high current was observed, indicating that the reduction of dissolved O_2 on pyrite surface occurred actively. Comparing to the control condition (w/o complexes), when treatment was done with Fe^{3+}-H_2xcat and Fe^{3+}-H_2ncat, currents became smaller, suggesting that the suppressive effects of DO reduction were achieved. The suppressive effects may be attributed to the formation of protective coating during oxidative decomposition of Fe^{3+}-H_2xcat and Fe^{3+}-H_2ncat complexes. As shown in Fig. 5-6 (A), with Fe^{3+}-H_2xcat and Fe^{3+}-H_2ncat, RC-parallel circuit corresponding to the presence of coating was not observed in EIS results, so the coatings formed by Fe-H_2xcat and Fe-H_2ncat complexes may be very thin that could not be detected by EIS measurement. Currents observed for the electrodes pretreated with Fe-H_2cat and Fe-H_2mcat complex were almost same after 300 seconds and were apparently smaller than those achieved in the case of Fe^{3+}-H_2xcat and Fe^{3+}-H_2ncat, indicating that stronger suppressive effects on O_2 reduction were achieved. The smallest current was observed for the electrode pretreated with the Fe^{3+}-H_2ecat complex. This may be because thickest or widest protective coatings were formed as suggested in EIS results shown in Fig. 5-5(B).

5.3.4 Leaching experiment

To understand the effects of Fe^{3+}-catechol derivative complexes on pyrite oxidation, leaching experiment was conducted by mixing 1 g pyrite and 10 ml solutions containing 5 mM Fe^{3+}, 15 mM organic ligand (H_2cat, H_2mcat and H_2xcat) and 0.5 M TRIS buffer (pH 8). For comparison, the experiment with solution containing only buffer was also conducted. Fig. 5-8(A) showed the changes in the concentration of dissolved Fe with time. For the solution containing Fe-catechol/catechol derivative complexes, the initial Fe concentration is high while without the complexes, the initial Fe concentration is almost 0. After leaching for 1 day, the concentration of Fe in Fe^{3+}-H_2cat and Fe^{3+}-H_2mcat solution decreased, indicating these complexes were oxidatively decomposed to release Fe^{3+} (Eqs. 5-11 and 5-12) and the released Fe^{3+} were precipitated as Fe-oxyhydroxide (Eq. 5-13).

$$[Fe(cat)_2]^- + O_2 + 4\ H^+ \rightarrow Fe^{3+} + 2\ Q + 2\ H_2O \qquad (5\text{-}11)$$

$$[Fe(mcat)_2]^- + O_2 + 4\ H^+ \rightarrow Fe^{3+} + 2\ Q + 2\ H_2O \qquad (5\text{-}12)$$

$$Fe^{3+} + 3\ OH^- \rightarrow Fe(OH)_3 \qquad (5\text{-}13)$$

The results also showed that the decrease of dissolved Fe concentration in Fe^{3+}-H_2mcat solution was apparently faster than that in Fe^{3+}-H_2cat solution, indicating that the kinetic rate of Eq. 5-12 is faster than Eq. 5-11. This could be attributed to the electron donating effect of -CH_3 in the complexes, which causes an increase in E_{HOMO} (Fig. 5-5) and a decrease of oxidation potential for complex decomposition (Fig. 5-4). For the case of Fe-H_2xcat, the concentration of dissolved Fe did not decrease but slightly increased, suggesting that Fe-H_2xcat complex was not decomposed completely to form precipitates. The reason could be attributed to the electron withdrawing effect of -COOH, which caused a decrease in E_{HOMO} and an increase in oxidation potential of complexes.

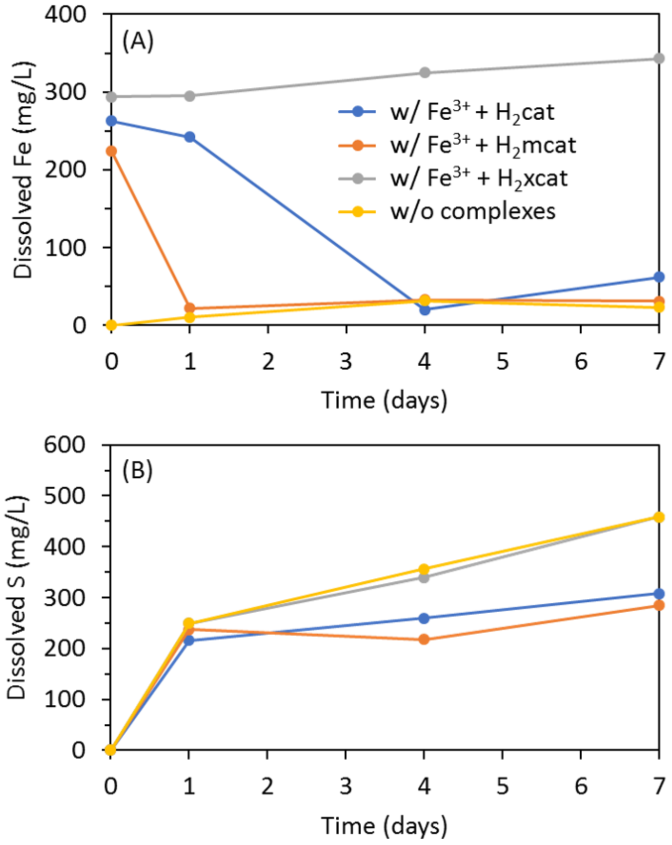

Fig. 5-8 Concentrations of (A) dissolved Fe and (B) S as a function of leaching time

Fig. 5-8(B) showed the concentration of dissolved S as a function of leaching time. For the solution without complex (control experiment), the concentration of dissolved S increased with time. This was caused by pyrite oxidation releasing dissolved S according to:

$$2\,FeS_2 + 7/2\,O_2 + H_2O \rightarrow 2\,Fe^{2+} + 2\,SO_4^{2-} + 2\,H^+ \quad (5\text{-}14)$$

The concentration of dissolved S released in the first day were similar as that of control experiment when Fe^{3+}-H_2mcat and Fe^{3+}-H_2mcat complexes were present in the solutions. After one day, SO_4^{2-} release was significantly suppressed with the complexes, indicating that the oxidation of pyrite was passivated with the complexes. The suppressive effects of Fe^{3+}-H_2mcat and Fe^{3+}-H_2cat complexes could be attributed to the formation of Fe-oxyhydroxide coating on pyrite surface (Eq.

5-13). As for Fe-H_2xcat, the concentration of dissolved S is closed to that obtained in control experiment. As shown in Fig. 5-7(A), Fe-H_2xcat complexes could not be decomposed to form coating on pyrite surface. This may be the reason why Fe^{3+}-H_2xcat complexes could not suppress pyrite oxidation.

5.4 Conclusions

In this chapter, the effects of Fe^{3+}-catechol derivative complexes with EDGs or EWGs on pyrite oxidation was studied. UV-Vis spectrophotometry showed tris-coordinated complexes could be formed between Fe^{3+} and catechol derivatives. Similar as Fe^{3+}-catecholate complexes, the oxidative decomposition of Fe-catechol derivative complexes was a sequential process. Based on the results of LSV, the presence of EDG such as -CH_3 or -CH_2CH_3 in the complexes decreased the oxidation potential of the complexes while the presence of EWG such as -COOH or -NO_2 increased the oxidation potential of complexes, which could be attributed to the effects of EDGs and EWGs on E_{HOMO} of Fe^{3+}-complexes. EIS results showed that thicker or wider coating was formed by the complexes with EDGs than with EWGs during oxidative decomposition, resulting in more effective suppression on O_2 reduction. Leaching experiments indicated that complexes with EDG suppressed pyrite oxidation by forming protective coating on pyrite surface. The complexes with EWGs could not be decomposed completely. As a result, coating did not form on pyrite surface, and pyrite oxidation was not suppressed.

References

Jha, R.K.T., Satur, J., Hiroyoshi, N., Ito, M., Tsunekawa, M., 2008. Carrier-microencapsulation using Si–catechol complex for suppressing pyrite floatability. Miner. Eng.,21, 889–893.

Jha, R.K.T., Satur, J., Hiroyoshi, N., Ito, M., Tsunekawa, M., 2011. Suppression of floatability of pyrite in coal processing by carrier microencapsulation. Fuel Process. Technol. 92(5), 1032-1036.

Jha, R.K.T., Satur, J., Hiroyoshi, N., Ito, M., Tsunekawa, M., 2012. Suppression of Pyrite Oxidation by Carrier Microencapsulation Using Silicon and Catechol. Miner. Process. Extr. Metall. Rev. 33, 89–98.

Li, X., Hiroyoshi, N., Tabelin, C.B., Naruwa, K., Harada, C., Ito, M., 2019a. Suppressive effects of ferric-catecholate complexes on pyrite oxidation. Chemosphere 214, 70–78.

Li, X., Gao, M., Hiroyoshi, N., Tabelin, C.B., Taketsugu, T., Ito, M., 2019b. Suppression of pyrite oxidation by ferric-catecholate complexes: An electrochemical study. Miner. Eng. 138, 226–237.

Nurchi, V.M., Pivetta, T., Lachowicz, J.I., Crisponi, G., 2009. Effect of substituents on complex stability aimed at designing new iron(III) and aluminum(III) chelators. J. Inorg. Biochem. 103, 227–236.

Park, I., Tabelin, C.B., Magaribuchi, K., Seno, K., Ito, M., Hiroyoshi, N., 2018a. Suppression of the release of arsenic from arsenopyrite by carrier-microencapsulation using Ti-catechol complex. J. Hazard. Mater. 344, 322–332.

Park, I., Tabelin, C.B., Seno, K., Jeon, S., Ito, M., Hiroyoshi, N., 2018b. Simultaneous suppression of acid mine drainage formation and arsenic release by Carrier-microencapsulation using aluminum-catecholate complexes. Chemosphere 205, 414–425.

Park, I., Tabelin, C.B., Jeon, S., Li, X., Seno, K., Ito, M., Hiroyoshi, N., 2019. A review of recent strategies for acid mine drainage prevention and mine tailings recycling. Chemosphere 219, 588–606.

Satur, J., Hiroyoshi, N., Tsunekawa, M., Ito, M., Okamoto, H., 2007. Carrier-microencapsulation for preventing pyrite oxidation. Int. J. Miner. Process. 83, 116–124.

Schweigert, N., Zehnder, A.J.B., Eggen, R.I.L., 2001. Chemical properties of catechols and their molecular modes of toxic action in cells, from microorganisms to mammals. Environ. Microbiol. 3, 81–91.

Yuniati, M.D., Kitagawa, K., Hirajima, T., Miki, H., Okibe, N., Sasaki, K., 2015a. Suppression of pyrite oxidation in acid mine drainage by carrier microencapsulation using liquid product of hydrothermal treatment of low-rank coal, and electrochemical behavior of resultant encapsulating coatings. Hydrometallurgy 158, 83–93.

Yuniati, M.D., Hirajima, T., Miki, H., Sasaki, K., 2015b. Silicate Covering Layer on Pyrite Surface in the Presence of Silicon–Catechol Complex for Acid Mine Drainage Prevention. Mater. Trans. 56, 1733–1741.

Chapter 6 Effects of ferric-catecholate complexes on Ti-based carrier-microencapsulation

6.1 Introduction

In the previous studies, CME using Ti^{4+}-catecholate complexes was studied. The results showed that Ti-based CME was effective in suppressing both pyrite oxidation and mobilization of arsenic (As) from arsenopyrite (FeAsS) by forming Ti-oxyhydroxide coating on pyrite or arsenopyrite surface. Comparing to the coating like Fe- or Al-oxyhydroxide formed by Fe- or Al-based CME, Ti-oxyhydroxide formed by Ti-CME is stable in a wider pH range, suggesting Ti-based CME may be more favorable for application in the real operation (Park et al., 2019). When the application of Ti-based CME is considered, it is important to understand the effects of co-existing ion. Ferric ion, Fe^{3+}, is a common co-existing ion that could be generated by dissolution of iron-containing minerals and was confirmed to form ferric-catecholate complexes with free catechol in the previous chapters. Although the effects of ferric-catecholate complexes on pyrite oxidation was investigated in the chapter 3 and 4, the effects of ferric-catecholate complexes on Ti-based CME remains unclear. In this chapter, the CME system containing both Ti^{4+}- and Fe^{3+}-catecholate complexes (bimetallic system) was studied. Formation of complexes in bimetallic systems were studied by ultraviolet-visible light (UV-Vis) spectrophotometry. Redox properties of complexes formed in bimetallic system were investigated by linear sweep voltammetry (LSV). Electrochemical impedance spectroscopy (EIS) measurement was conducted for investigating the coating formation in bimetallic system. Coating formation in bimetallic system was evaluated by shaking flask experiments and the coating formed on pyrite surface was analyzed by X-ray photoelectron spectroscopy (XPS). A model for coating formation in bimetallic system was made by thermodynamic calculation.

6.2 Methodology

6.2.1 UV-Vis spectrophotometry

Solutions were prepared by dissolving 0.1mM Fe^{3+}, 0.1mM Ti^{4+} and various concentration of catechol (0.1 mM - 0.6 mM) in deionized (DI) water. The solutions were adjusted to pH 8 and filtered by membrane filter (pore size: 0.2 μm). The solutions were poured into the single-crystal cell and measured by UV–Vis spectrophotometer (V-630, Jasco Analytical Instruments, Japan). During measurement, solutions were maintained at 25 °C. The UV–Vis absorption spectrum was measured between 800 and 300 nm.

6.2.2 Linear sweep voltammetry (LSV)

Redox properties of bimetallic catecholate complexes were investigated by anodic LSV using a computer-controlled electrochemical measurement unit (SI 1280B, Solartron Instruments, UK). A conventional three-electrode system was used consisting of a platinum (Pt) rod working electrode (surface area: 7.06 mm^2), a Pt wire counter electrode, Ag/AgCl/3.3 M NaCl reference electrode, and a glass cell with water-jacket connected to a recirculating thermostat water bath (BB400, Yamato Scientific Co. Ltd., Japan).

Solutions for LSV was prepared by dissolving (i) 1mM Fe^{3+} and 3mM catechol, (ii) 1mM Ti^{4+} and 3mM catechol and (iii) 1mM Fe^{3+}, 1mM Ti^{4+} and 3mM catechol in 0.1M $NaNO_3$ solutions. The solutions were adjusted to pH 10 and filtered by membrane filter (pore size: 0.2 μm). 12ml solution was poured in the cell maintained at 25 °C and purged with N_2 (99.999% purity) for 30 min through a Teflon® tube to remove dissolved oxygen (DO). Before each measurement, the tube tip was repositioned slightly above the surface of the solution, and N_2 was continuously introduced to avoid redissolution of oxygen during the measurement. The LSV measurement was started after equilibration at the open circuit potential (OCP) towards positive (+ 0.8 V) at a sweep rate of 5 mV/s.

6.2.3 Electrochemical impedance spectroscopy (EIS)

Solutions in experiment was prepared by adding (i) 5mM Fe^{3+} and 30mM catechol, (ii) 5mM Ti^{4+} and 30mM catechol and (iii) 5mM Ti^{4+}, 5mM Fe^{3+} and 30mM catechol in 0.1M $NaNO_3$. All the solutions were adjusted to pH 8 and filtered with 0.2 μm syringe-driven membrane filter. Chronoamperometry at + 0.8 V was applied to Pt electrode for 1 hours to induce the coating formation in the solutions. After chronoamperometry, electrode with coating was taken out from complex solutions, washed with DI water and reset in diluted H_2SO_4 solution (pH 2.5) for conducting EIS (DC bias, 0 Vs OCP; AC amplitude, 5 mV; AC frequency, 20000 Hz to 0.1 Hz).

6.2.4 Shaking flask experiment

Solutions for shaking flask experiment was prepared by adding (i) 5mM Fe^{3+} and 30mM catechol, (ii) 5mM Ti^{4+} and 30mM catechol and (iii) 5mM Fe^{3+}, 5mM Ti^{4+} and 30mM catechol in deionized water. All solutions were adjusted to pH 8 and filtered by were membrane filter (pore size: 0.2 μm). Shaking flask experiments were carried out by mixing 1 g of washed pyrite (106–150 μm) and 10 ml solution in 50-ml Erlenmeyer flask shaken at 120 strokes/min in a constant temperature water bath maintained at 25 °C. At predetermined time intervals, suspensions were collected and filtered using a 0.2 μm membrane filter. The filtrates were analyzed for dissolved Fe and Ti concentrations using ICP-AES (margin of error = ± 2%) while the residues were thoroughly washed with DI water, dried in a vacuum drying oven at 40 °C for 24 h, and analyzed by X-ray photoelectron spectroscopy (XPS, JPS-9200, JEOL Ltd., Japan).

6.3 Results and discussions

6.3.1 Characterization of the complexes in bimetallic catecholate complex system

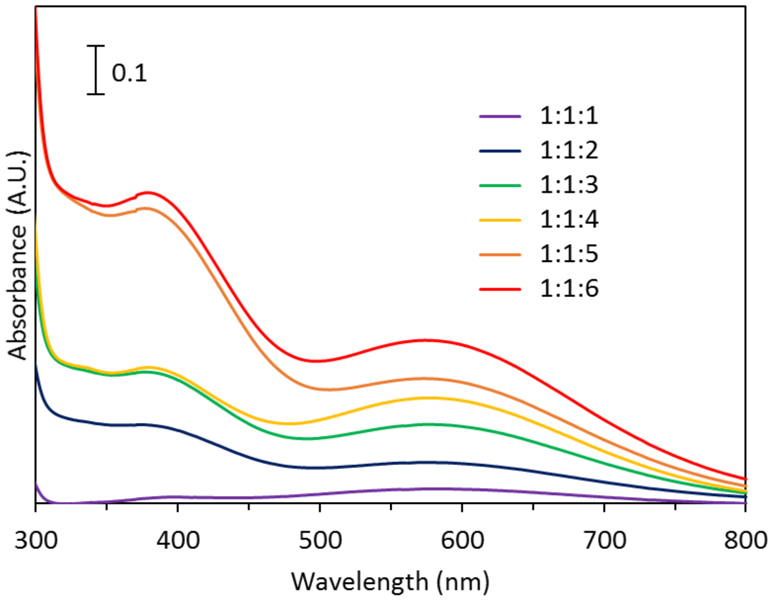

Fig. 6-1 UV-Vis spectra of solution containing Fe-Ti-catechol with different molar ratios of [Fe]: [Ti]: [catechol]

In chapters 2 and 3, the speciation of Fe^{3+}- and Ti^{4+}-catecholate complexes under different pH was studied and the results showed that at pH 8, the predominant species were $[Fe(cat)_2]^-$ and $[Ti(cat)_3]^{2-}$, respectively. UV-Vis spectra of solutions containing 0.1 mM Fe^{3+}, 0.1 mM Ti^{4+} and various concentration catechol (0.1 mM - 0.6 mM catechol) were shown in Fig. 6-1. The results showed that even in the case that 0.1 mM catechol was present in the solution, absorbance peaks appeared around 380-400 nm and 570-590 nm, corresponding to the presence of $[Ti(cat)_3]^{2-}$ and $[Fe(cat)_2]^-$, respectively. It indicated that when the concentration of catechol was low, Fe^{3+} and Ti^{4+} competed for coordination with catechol and both of $[Ti(cat)_3]^{2-}$ and $[Fe(cat)_2]^-$ present in the solution simultaneously. With increase of concentration of catechol, absorbance peak around 380-400 nm and 570-590 nm increased, indicating that the concentration of $[Ti(cat)_3]^{2-}$ and $[Fe(cat)_2]^-$ increased.

6.3.2 Redox properties of bimetallic catecholate complexes

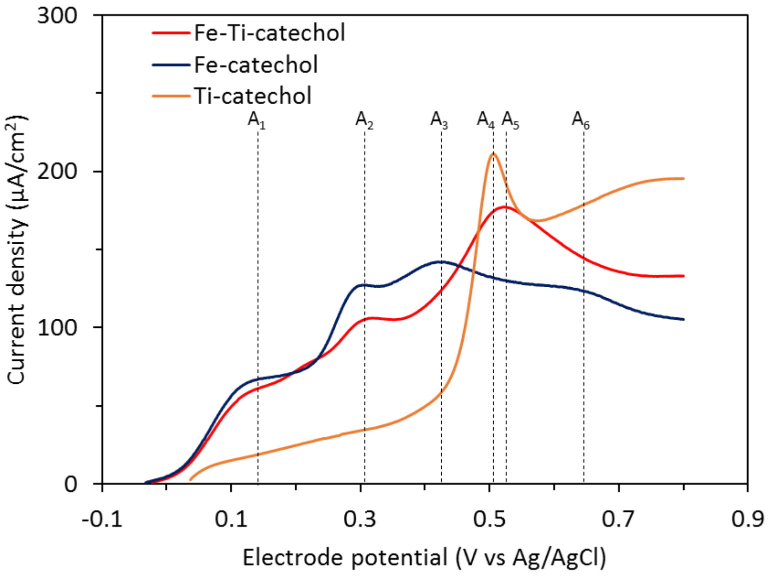

Fig. 6-2 Linear sweep voltammograms of solutions containing Fe-catechol, Ti-catechol or Fe-Ti-catechol

In chapters 2, 3, and 4, the redox properties of Fe^{3+}- and Ti^{4+}-catecholate complexes were investigated. As shown in Fig. 6-2, for $[Fe(cat)_3]^{2-}$, three anodic current peaks (A_1, A_2 and A_3) corresponding to sequential oxidative decomposition of Fe^{3+}-catecholate complexes (Eq. 6-1, Eq. 6-2, and Eq. 6-3) and a peak corresponding to oxidation of free catechol (A_6) (Eq. 6-4) were observed.

$[Fe(cat)_3]^{3-} \rightarrow [Fe(cat)_2]^{-} + Q + 2\ e^{-}$ (6-1)

$[Fe(cat)_2]^{-} \rightarrow [Fe(cat)]^{+} + Q + 2\ e^{-}$ (6-2)

$[Fe(cat)]^{+} \rightarrow Fe^{3+} + Q + 2\ e^{-}$ (6-3)

$H_2cat \rightarrow Q + 2\ H^{+} + 2\ e^{-}$ (6-4)

For $[Ti(cat)_3]^{2-}$, a peak (A_4) corresponding to one-step oxidative decomposition of this complex (Eq. 6-5) was detected.

$[Ti(cat)_3]^{2-} \rightarrow Ti^{4+} + 3\ Q + 6\ e^{-}$ (6-5)

When $[Fe(cat)_3]^{3-}$ and $[Ti(cat)_3]^{2-}$ coexisted in the solution, current peaks A_1 and A_2 were observed, indicating that oxidation of Fe^{3+}-catecholate complexes described in Eq. 6-1 and 6-2 occurred without being affected by the presence of $[Ti(cat)_3]^{2-}$. A peak A_3 corresponding to Eq. 6-3 (oxidation of $[Fe(cat)]^{+}$) and a sharp peak A_4 corresponding to Eq. 6-5 (oxidation of $[Ti(cat)_3]^{2-}$) were absent while a wider peak A_5 were detected in this bimetallic catecholate system. This result suggested that the oxidative decompositions of $[Fe(cat)]^{+}$ and $[Ti(cat)_3]^{2-}$ were suppressed and a new reaction corresponding to peak A_5 occurred. This new reaction may be attributed to a simultaneous decomposition of $[Fe(cat)]^{+}$ and $[Ti(cat)_3]^{2-}$. Detail of the new reaction will be discussed later.

6.3.3 Evaluation of coating formed by bimetallic catecholate complexes

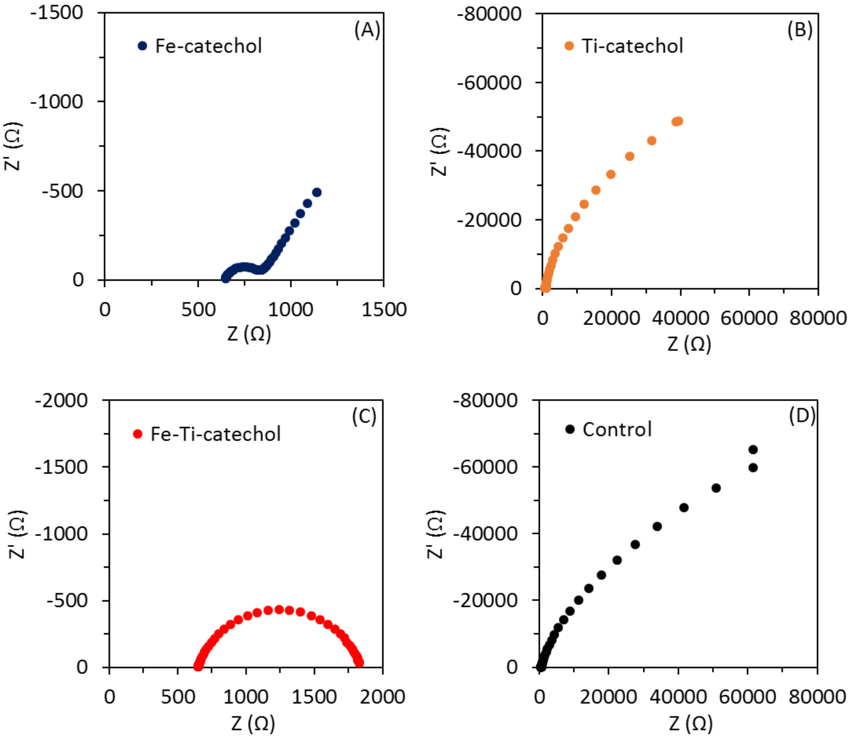

Fig. 6-3 EIS results of Pt electrode pretreated by anodic polarization at + 0.8 V for 1 h with (A) Fe-catechol, (B) Ti-catechol, (C) Fe-Ti-catechol and (D) no complex

EIS measurements were conducted for comparing the coating properties formed in Fe-catechol, Ti-catechol and Fe-Ti-catechol systems. For comparison, EIS measurement was also applied to a Pt electrode pretreated (anodically polarized at + 0.8 V for 1 h) in the solution without addition of Fe^{3+}, Ti^{4+} and catechol (control experiment). The results of EIS were shown in Fig. 6-3. For the case pretreated in Fe-catechol system, a semi-circle with an inclined straight line was observed. The semi-circle may correspond to the presence of parallel resistor-capacitor (RC) circuit in the coating and the inclined straight line may correspond to a Warburg impedance relating to a diffusion process. The results indicated that the coating could be formed in Fe-catechol system. For the case pretreated in Ti-catechol system, semi-circle corresponding to the presence of coating was not observed, which was similar as the result obtained in the control experiment. These results indicate that metal oxyhydroxide coating formed in Fe-catechol system but did not form in Ti-catechol system. In the experiments here, metal ion concentration was about 1 mM while catechol concentration was 6 mM. Because maximum coordination number of catechol to metal ions (ferric and titanium ions) is three, in this condition, an excessive concentration (about 3 mM) of free catechol presented in the solution. Oxidation of free catechol may compete with that of metal catecholate complexes and inhibit the coating formation due to the oxidation of the complexes. Compared to Fe-catechol system, oxidation peak positions of free catechol (A_6) and $[Ti(cat)_3]^{2-}$ (A_4) were closer, which may cause an intensive competition between free catechol and $[Ti(cat)_3]^{2-}$ in the oxidation process. This may be a reason why the coating was not formed in Ti-catechol system but formed in Fe-catechol system.

For the case pretreated in Fe-Ti-catechol system, a clear semi-circle was observed, indicating the formation of coating. To compare the electrochemical properties of the coating formed in Fe-catechol and Fe-Ti-catechol system, equivalent circuit (A) and (B) shown in Fig. 6-4 were applied for analyzing the EIS results shown in Fig. 6-3(A) and (C), respectively and the fitting results were shown in Table 6-1. In equivalent circuit (A) and (B), R_s represents for solution resistance; R_d and Q_f represent for the resistance in the defect area of coating and the constant phase element corresponding to the capacitance of the coating, respectively; W_s represents for Warburg short corresponding to the diffusion with transmissive boundary. As shown in Table 6-1, R_d in the coating formed in Fe-Ti-catechol system was about 5 times bigger than the one formed by Fe-catechol system, indicating that a coating with a higher resistance may be formed in the bimetallic catecholate complex solution.

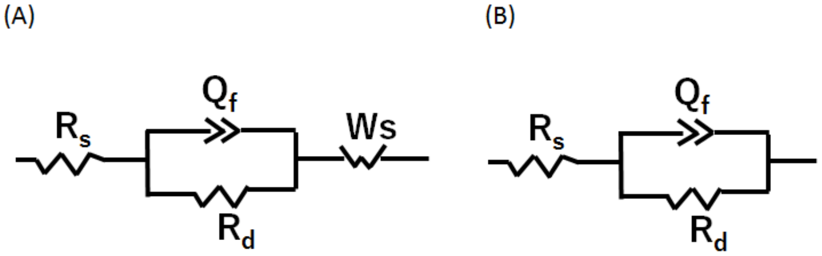

Fig. 6-4 Two equilibrant circuit (A) and (B)

Table 6-1 Fitting results of EIS results of coatings formed in Fe-catechol and Fe-Ti-catechol system

	Fe-catechol	Fe-Ti-catechol
R_s (Ω)	652	647.3
R_d (Ω)	237.1	1199
Q_f-T	5.33E-5	3.71E-5
Q_f-P	0.80	0.74
W_s-R (Ω)	1497	--
W_s-T	6.52	--
W_s-P	0.70	--

6.3.4 Formation of coating on pyrite

Shaking flask experiments were conducted to investigate the formation of coating on pyrite surface in the presence of metal ions and catechol. Fig. 6-5(A) and (B) showed the change of the concentrations of dissolve Fe and Ti in the solutions with time. For the solutions containing (i) Fe^{3+} and catechol and (ii) Fe^{3+}, Ti^{4+} and catechol, the initial concentrations of dissolved Fe were high due to the presence of Fe^{3+}-catecholate complexes while Fe was not present in the solution containing (iii) Ti^{4+} and catechol. For the solution containing (ii) Fe^{3+}, Ti^{4+} and catechol, and (iii) Ti^{4+} and catechol, the initial dissolved Ti concentrations were high due to the presence of $[Ti(cat)_3]^{2-}$.

The concentrations of dissolved Fe for Fe-catechol system (Fig. 6-5(A)) and dissolved Ti for Ti-catechol system (Fig. 6-5(B)) were kept almost constant during the experiments. This was probably attributed to the following reasons: (1) The competition between catechol and metal-catecholate complexes inhibited the decomposition of metal-catecholate complexes, and/or (2) products of the decomposition of metal-catecholate complexes (intermediate metal catechol complex like $[Fe(cat)]^+$, metal ions, metal-oxyhydroxide) react with free catechol to reproduce metal-catecholate complexes.

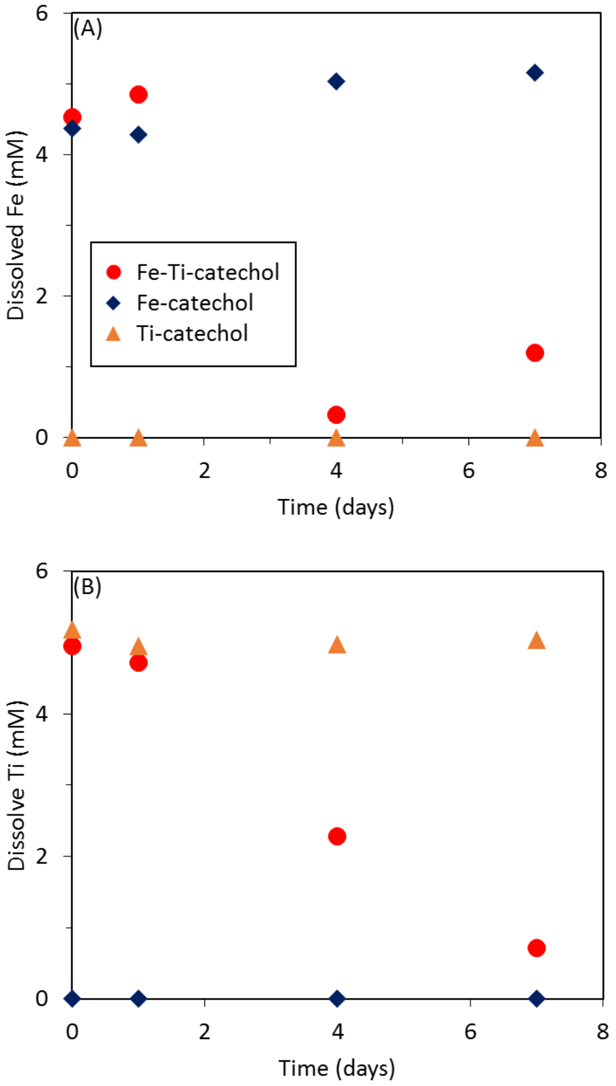

Fig. 6-5 Concentration of (A) dissolved Fe and (B) dissolved Ti as function of time

For Fe-Ti-catechol system, significant decrease of Fe and Ti concentrations were observed. This indicates that the decomposition of $[Fe(cat)_2]^-$ and $[Ti(cat)_3]^{2-}$ occurred and a coating containing Fe and Ti was formed. A possible reason of the decrease of Ti and Fe concentrations may be the lower concentration of free catechol in Fe-Ti-catechol system: in this bimetallic system, both 5mM of Fe^{3+} and 5 mM of Ti^{4+} was mixed with 30 mM catechol, and both metal ions coordinated with catechol, causing a lower concentration of uncoordinated free catechol than those of Fe-catechol system (5 mM Fe^{3+} and 30 mM catechol) and Ti-catechol system (5 mM Ti^{4+} and 30 mM catechol). In this case, it is possible to consider that the inhibition of metal-catecholate complex oxidation and metal oxyhydroxide coating formation due to free catechol become weaker and coating formation may occur with a faster reaction rate.

There may be another possibility to interpret the faster coating formation in Fe-Ti-catechol system: The oxidation of metal-catecholate complexes in the bimetallic system was not as same as that occurred in Fe-catechol or Ti-catechol solution as shown in the results of LSV (Fig. 6-2). The results of EIS also showed that a coating with a higher resistance formed in the bimetallic system. These results suggest that the oxidation of metal-catecholate complexes and the subsequent coating formation process are changed in the presence of both Fe^{3+} and Ti^{4+}-catecholate complexes, and this cause a faster coating formation in the presence of both metal complexes. In the bimetallic catecholate system, formation of oxyhydroxide containing both metal ions is possible. To identify the coating formed on pyrite surface in Fe-Ti-catechol system, surface analysis (XPS) of pyrite residue was conducted in next subsection 6.3.5.

6.3.5 Surface analysis (XPS)

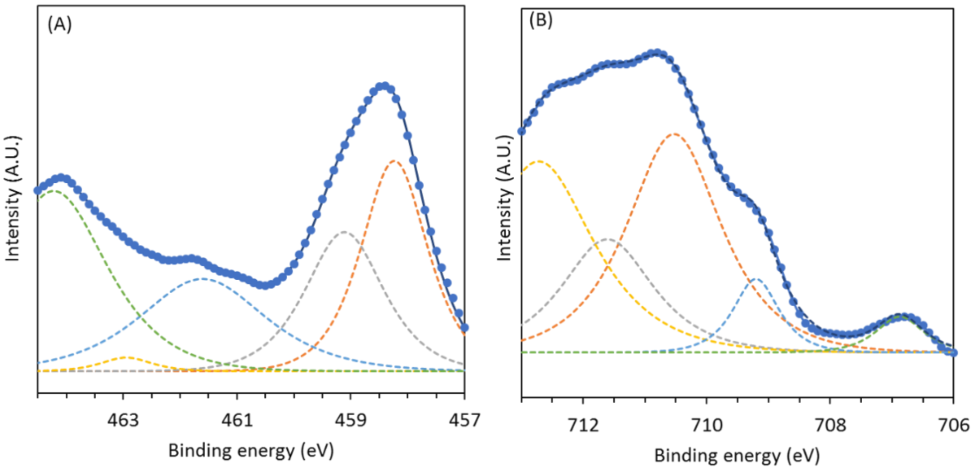

Fig. 6-6 XPS spectra of (A) Ti 2p and (B) Fe 2p of component on pyrite surface after treated in Fe-Ti-catechol system for 7 day

In order to have a better understanding of the coating composition on pyrite surface, XPS was applied on the pyrite treated in Fe-Ti-catechol solutions for 7 days. Fig. 6-6(A) and (B) showed the XPS spectra of Ti 2p and Fe 2p, respectively. In Fig. 6-6(A), doublet peaks at 458.2 eV and 464.2 eV may be ascribed to Ti $2p_{3/2}$ and Ti $2p_{1/2}$ in $FeTiO_3$ (Guo et al., 2016). A peak centering at 459.1 eV could be assigned to the tetravalent valence state of Ti(IV) in Ti_3O_5 (Shen et al., 2017) and a peak centering at 461.6 eV may correspond to the presence of TiC (Hao et al., 2017). In Fig. 6-6(B), a peak at 706.9 eV is attributed to presence of pyrite (Qiu et al., 2013). A peak at 710.5 eV is closed to the value reported for Fe $2p_{3/2}$ in $FeTiO_3$ (Guo et al., 2016), which was in line with the results for Ti in Fig. 6-6 (A). Peaks at 709.2 eV, 711.6 eV and 712.7 eV may be attributed to the presence of FeO, α-FeOOH and Fe_2O_3, respectively (Godec et al., 2008, Ohtsuka, 2015, Rahman et al., 2013), which may be produced by oxidation of pyrite or precipitation of Fe^{3+} released from Fe^{3+}-catecholate complexes.

6.3.6 A model of coating formation in the presence of Fe^{3+}- and Ti^{4+}-catecholate complexes

As discussed in the last subsection, both XPS spectra of Ti 2p and Fe 2p suggested the presence of $FeTiO_3$ on pyrite surface. If this is the case, there may be a reasonable explanation for the simultaneous precipitation of dissolved Ti and Fe, which was observed in Fig 6-5 (A) and (B): $[Fe(cat)_2]^-$ and $[Ti(cat)_3]^{2-}$ are oxidized simultaneously on pyrite surface to form $FeTiO_3$ coating on pyrite surface according to

$$[Fe(cat)_2]^- + [Ti(cat)_3]^{2-} + 3\ H^+ + 9/4\ O_2 \rightarrow FeTiO_3 + 5\ Q + 3/2\ H_2O \qquad (6\text{-}6)$$

The standard Gibbs energy change (ΔG°) for Eq. 6-6 was calculated based on the thermodynamic data listed in the Table 6-2.

Table 6-2 Standard Gibbs free energy of formation (ΔG°_f) used in this chapter

Component	$\Delta G^\circ_{f\ (kJ/mol)}$	Reference
H^+	0	Dean and Lange (1999)

O_2	0	Dean and Lange (1999)
H_2O	-237.1	Dean and Lange (1999)
H_2cat	-210.0	Dean and Lange (1999)
Q	-56.6	Horner and Geyer (1965)[*1]
$[Fe(cat)_2]^-$	-198.1	Avdeef et al. (1978)[*2]
$[Ti(cat)_3]^{2-}$	-342.5	Creutz and Chou (2008)[*2]
Fe_2O_3	-742.2	Dean and Lange (1999)
$FeTiO_3$	-1155.3	Berman (1988)
Fe_2TiO_5	+4.9	Kumagai et al. (2017)
TiO_2	-889.5	Berman (1988)

[*1] ΔG°_f of Q was calculated from standard electrode potential of Q/H_2cat reported in Horner and Geyer (1965) and ΔG°_f of catechol.

[*2] ΔG°_f of $[Fe(cat)_2]^-$ was calculated from the stability constants determined by experiments by Avdeef et al. (1978). ΔG°_f of $[Ti(cat)_3]^{2-}$ was calculated by the constant reported by Creutz and Chou (2008) .

The calculation result showed that ΔG° for Eq. 6-15 is - 1253.6 kJ/mol, indicating that the Eq. 6-13 is thermodynamically possible. For comparison, the ΔG°_f for formation of Fe_2O_3, TiO_2 and $FeTi_2O_5$ were calculated and shown in Eqs. 6-15, 6-16 and 6-17.

$$2\,[Fe(cat)_2]^- + 2\,H^+ + 2\,O_2 \rightarrow Fe_2O_3 + 4\,Q + H_2O \quad \Delta G^\circ = -\,809.5\ \text{kJ/mol} \tag{6-7}$$

$$[Ti(cat)_3]^{2-} + 2\,H^+ + 3/2\,O_2 \rightarrow TiO_2 + 3\,Q + H_2O \quad \Delta G^\circ = -\,953.9\ \text{kJ/mol} \tag{6-8}$$

$$2\,[Fe(cat)_2]^{2-} + [Ti(cat)_3]^{2-} + 7/2\,H_2O + 4\,H^+ \rightarrow Fe_2TiO_5 + 2\,H_2O + 7\,Q \quad \Delta G^\circ = -\,126.8\ \text{kJ/mol}$$

(6-9)

The values of ΔG° for Fe_2O_3, TiO_2 and Fe_2TiO_5 formation, as shown in Eq. 6-7, 6-8, and 6-9 are -809.5, -953.9, and -126.8 kJ/mol, respectively, which are higher than $\Delta G°_f$ for $FeTiO_3$ formation. This indicates that the formation of $FeTiO_3$ are more thermodynamically favorable than formation of Fe_2O_3, TiO_2, and Fe_2TiO_5. Considering this, it is possible to assume that in the presence of both $[Fe(cat)_2]^-$ and $[Ti(cat)_3]^{2-}$, $FeTiO_3$ is formed rather than TiO_2 and Fe_2O_3, and this may cause a faster coating formation in the bimetallic system. The model assuming the formation of $FeTiO_3$ make it possible to interpret the andic current peak at A_5 observed in the presence of both $[Fe(cat)_2]^-$ and $[Ti(cat)_3]^{2-}$ (Fig. 6-2). In the results of LSV, by the sequential oxidation of ferric-catecholate complexes, $[Fe(cat)]^+$ was formed, and oxidized together with $[Ti(cat)_3]^{2-}$ to from $FeTiO_3$ according to

$$[Fe(cat)]^+ + [Ti(cat)]^{2-} + 3\ H_2O \rightarrow FeTiO_3 + 6\ H^+ + 7\ e^- \qquad (6\text{-}10)$$

6.4 Conclusions

In this chapter, the bimetallic system containing Fe-Ti-catechol was discussed. UV-Vis spectrophotometry showed that Fe^{3+} and Ti^{4+} competed to form complexes with catechol, and $[Fe(cat)_2]^-$ and $[Ti(cat)_3]^{2-}$ could coexist in the solution. Results of LSV indicated that oxidation of $[Fe(cat)_3]^{2-}$ and $[Fe(cat)_2]^-$ was not affected in the presence of $[Ti(cat)_3]^{2-}$ while the oxidation of $[Fe(cat)]^+$ may shift and be oxidized simultaneously with $[Ti(cat)_3]^{2-}$. EIS results showed that coating formed in the solution containing both Ti^{4+}- and Fe^{3+}-catecholate complexes was more resistant than the case formed in Fe-catechol system, while no coating was formed in solution containing Ti-catchol. Shaking flask experiments with pyrite showed that in bimetallic system, both of dissolved Fe and Ti precipitated on pyrite surface. The results of XPS suggested the formation of $FeTiO_3$ on pyrite surface and thermodynamic calculation indicated that the formation of $FeTiO_3$ are more thermodynamically favorable than formation of Fe_2O_3 and TiO_2.

References

Avdeef, A., Sofen, S.R., Bregante, T.L., Raymond, K.N., 1978. Coordination chemistry of microbial iron transport compounds. 9. Stability constants for catechol models of enterobactin. J. Am. Chem.

Soc. 100, 5362–5370.

Berman, R.G., 1988. Internally-consistent thermodynamic data for minerals in the system Na_2O-K_2O-CaO-MgO-FeO-Fe_2O_3-Al_2O_3-SiO_2-TiO_2-H_2O-CO_2. J. Petrol. 29, 445–522.

Creutz, C., Chou, M.H., 2008. Binding of catechols to mononuclear titanium (IV) and to 1- and 5-nm TiO_2 nanoparticles. Inorg. Chem. 47, 3509–3514.

Dean, J.A., Lange, N.A. (Eds.), 1999. Lange's handbook of chemistry, 15. ed. ed, McGraw-Hill handbooks. McGraw-Hill, New York, NY.

Godec, M., Mandrino, D., Šuštaršič, B., Nolan, D., Jenko, M., 2008. Characterisation of rapidly solidified nanocrystalline soft magnetic ribbons based on Fe-Si-B with P and Ga additions. Surf. Interface Anal. 40, 498–502.

Guo, S., Liu, J., Qiu, S., Wang, Y., Yan, X., Wu, N., Wang, S., Guo, Z., 2016. Enhancing electrochemical performances of TiO2 porous microspheres through hybridizing with FeTiO3 and nanocarbon. Electrochimica Acta 190, 556–565.

Hao, L., Wang, Z., Zheng, Y., Li, Q., Guan, S., Zhao, Q., Cheng, L., Lu, Y., Liu, J., 2017. C, N co-doped TiO_2/$TiC_{0.7}N_{0.3}$ composite coatings prepared from TiC0.7N0.3 powder using ball milling followed by oxidation. Appl. Surf. Sci., 2nd International Symposium on Energy and Environmental Photocatalytic Materials 391, 275–281.

Horner, L., Geyer, E., 1965. Zur Kenntnis der o-Chinone, XXVII: Redoxpotentiale von Brenzcatechin-Derivaten. Chem. Ber. 98, 2016–2045.

Kumagai, N., 2017. New concept of rutile processing from ilmenite ore; Free energy of formation of pseudobrookite.

Ohtsuka T., 2015. The present and future on surface analysis for corrosion study. Zair. Kankyo 64, 268–272.

Park, I., Tabelin, C.B., Jeon, S., Li, X., Seno, K., Ito, M., Hiroyoshi, N., 2019. A review of recent strategies for acid mine drainage prevention and mine tailings recycling. Chemosphere 219, 588–606.

Qiu, X., Liu, M., Hayashi, T., Miyauchi, M., Hashimoto, K., 2013. Solution-based synthesis of pyrite films with enhanced photocurrent generation. Chem. Commun. 49, 1232–1234.

Rahman, M., Khan, S., Jamal, A., Faisal, M., Asiri, A.M., A. Alamry, K., Khan, A., Khan, A.A., Abdul Rub, M., Azum, N., Al-youbi, A., 2013. Large-scale synthesis of low-dimension un-doped iron oxide nanoparticles by a wet-chemical method: efficient photo-catalyst & sensitive chemi-sensor applications. Micro Nanosyst. 5, 3–13.

Shen, Z., Shi, Q., Huang, W., Huang, B., Wang, M., Gao, J., Shi, Y., Lu, T., 2017. Stabilization of microcrystal λ-Ti_3O_5 at room temperature by aluminum-ion doping. Appl. Phys. Lett. 111, 191902.

Chapter 7 General conclusions

Pyrite is a common sulfide mineral in nature, and it is separated from valuable minerals and disposed to tailing dams in coal and metal mines. When pyrite is exposed to air and water, it is oxidized to form sulfuric acid, which causes acid mine drainage (AMD), a serious environmental problem in mining industry. Neutralization techniques have been commonly used to treat AMD, but they are unsustainable because AMD formation could be continued even after closure of mine. It is important to develop a sustainable method to suppress pyrite oxidation in tailing dam and prevent AMD formation. Carrier-microencapsulation (CME) has been proposed as a promising method to prevent the formation of AMD by forming a protective coating on pyrite surface. Using model experiments, the previous studies demonstrated that CME using titanium-, silicon- or aluminum-catecholate complexes effectively suppressed pyrite oxidation by forming metal-oxyhydroxide coating on pyrite surface. Considering the actual operation of CME, it is needed to understand the effects of co-existing metal ions. A common co-existing metal ion associated with pyrite is ferric ion, because it is a product of pyrite oxidation process. In this study, the effects of coexisting ferric ions on CME for suppressing pyrite oxidation were investigated.

Chapter 1 included the statement of the problem, objectives of this study and a literature review of pyrite, pyrite oxidation and prevention techniques of AMD formation.

In chapter 2, the thermodynamic and redox properties of ferric-catecholate complex were compared to aluminum- and titanium-catecholate complexes. Mono-, bis- and tris-catecholate complexes were formed in the solution containing ferric ions and catechol as same as aluminum-catechol system, while only tris-catecholate complexes was formed in solution containing titanium ions and catechol. The results of linear sweep voltammetry (LSV) indicated that ferric-catecholate complexes was decomposed sequentially: tris-catecholate complex were decomposed to bis-catecholate complex, and bis-catecholate complex was decomposed to mono-catecholate complex, then finally mono-catecholate complex was decomposed to release ferric ions. The sequential decomposition also occurred for aluminum-catecholate complexes while decomposition of titanium-catecholate complex was a one-step reaction: tris-catecholate complex was directly decomposed to release titanium ions. Among three complexes, ferric-catecholate was decomposed at the lowest redox potential and the decomposition rate was fastest. The coating formed with ferric-catecholate by polarization strongly suppressed the reduction of dissolved oxygen on platinum electrode.

In chapter 3, the effects of ferric-catecholate complexes on pyrite oxidation were investigated. Microscopic observation confirmed that coating was formed on pyrite treated with mono- and bis-catecholate complexes. Results of SEM-EDX and ATR-FTIR indicated that the coating was mainly composed of iron-oxyhydroxide phases. The results of leaching experiments showed that pyrite oxidation was suppressed by ferric-catecholate complexes via two mechanisms: (1) electron donating effects of the complexes, and (2) formation of a protective coating on pyrite.

In chapter 4, the details of coating formation with ferric-catecholate complexes and the effects of the coating on pyrite oxidation were investigated by conducting a series of electrochemical studies. The results of theoretical calculation showed that the sequential decomposition of ferric-catecholate complexes on pyrite occurred at different electrode potentials corresponded to the different HOMO energy levels of the tris-, bis-, and mono-catecholate complexes of ferric ions. Chronoamperometry and EIS using a rotating disk platinum (Pt) electrode indicated that a passive coating was formed when oxidative decomposition of Fe^{3+}-catecholate complexes occurred. When longer decomposition time and higher anodic potentials were applied, defects in the coat decreased, resulting in the formation of a more resistant coating. A comparison of the chronoamperometry results of coated and uncoated pyrite electrodes suggests that the coating formed with ferric-catecholate complex suppressed both anodic and cathodic half-cell reactions of pyrite oxidation by limiting the diffusion of reactants and products between pyrite and bulk solution phase.

In chapter 5, electrochemical properties of ferric-complexes with catechol derivatives, which are catechol substituted with electron donating groups (EDGs) and electron withdrawing group (EWGs) as potential carrier for CME was evaluated. Results of LSV indicated that the oxidation potential of ferric-complexes decreased with EDGs but increased with EWGs. Chronoamperometry and EIS showed the coating formation was enhanced with presence of EDGs while suppressed with

EWGs. Results of leaching experiments suggested that ferric-complexes with EDGs suppressed pyrite oxidation by forming protective coating on pyrite surface while no suppressive effect was achieved by the complexes with EWGs.

Chapter 6 evaluated the effects of ferric-catecholate complexes on Ti-based CME. UV-Vis spectra indicated that both ferric- and titanium-catecholate complexes were formed in solution. The results of LSV and chronoamperometry suggested that ferric- and titanium-catecholate may be oxidatively decomposed at similar potential to form a Fe-Ti-oxyhydroxide due to the co-precipitation of titanium and ferric ion. Shaking flask experiments showed that with presence of ferric-catecholate complexes, decomposition of titanium-catecholate complex to release titanium ions was enhanced. The results of XPS and thermodynamic calculation suggested that $FeTiO_3$ may be formed on pyrite surface.

Acknowledgement

Firstly, I would like to express my sincere appreciation to my supervisor Prof. Hiroyoshi Naoki for his continuous support since I was a master student. During my doctoral course, he gave me so many constructive advices on the research, presentation and journal paper writing. He was always willing to hear my opinions and encourage me to overcome the difficulties in the research. I am really appreciated that I could work under his guidance.

I would like to thank Assoc. Prof. Mayumi Ito and Assis. Prof. Carlito Baltazar Tabelin for their valuable suggestions and critical comments on my study.

My sincere thanks also go to the committee members for examining doctoral dissertation, Prof. Toshifumi Igarashi and Assoc. Prof. Yasumasa Tojo for their valuable advices on the revision of this dissertation.

I would like to thank Mr. Kosuke Naruwa and Ms. Chie Harada, who worked with me in CME research group, for their valuable inputs into the research of CME. I also thank the other lab mates for their assistance to my study.

Special appreciation goes to Ministry of education culture sports science and technology (MEXT) for providing finical support during my master and doctoral courses.

Finally, I would like to thank my beloved grandparents and all my family for their moral support throughout my study and life.